Electron–Photon Interaction in Quantum Dots: Spin and Entanglement

Inauguraldissertation

zur

Erlangung der Würde eines Doktors der Philosophie

vorgelegt der

Philosophisch-Naturwissenschaftlichen Fakultät

der Universität Basel

von

Oliver Gywat

aus Riehen (BS)

Basel, 2005

Genehmigt von der Philosophisch-Naturwissenschaftlichen Fakultät auf Antrag von

Prof. Dr. Daniel Loss
Prof. Dr. David D. Awschalom

Basel, den 8. Februar 2005

Prof. Dr. Hans-Jakob Wirz
Dekan

Acknowledgements

First of all, I would like to thank Prof. Daniel Loss for accepting me as a Ph. D. student. I am very much obliged to his guidance and to many important ideas he has contributed to this thesis. Moreover, I have benefitted a lot from a unique research environment during my Ph. D. studies, for which I am deeply grateful to him. The Condensed Matter Theory Group at the University of Basel has provided a friendly and stimulating scientific environment for which I thank all of its members. In addition to the discussions with my supervisor I had the pleasure to collaborate in Basel with Dr. Guido Burkard, Veronica Cerletti, Bill Coish, and Dr. Hans-Andreas Engel. I am very grateful to them for many fruitful discussions. I also appreciated very much that I was given the opportunity to participate in various schools and conferences. The close collaboration with the group of Prof. David D. Awschalom at the University of California at Santa Barbara has been an exciting and also a very inspiring experience. Many thanks are here to Prof. David D. Awschalom, Ryan J. Epstein, Felix Mendoza, and, especially, to Dr. Florian Meier for their contributions to this thesis. I would also like to acknowledge very useful discussions with Martin H. Baier, Dr. Denis V. Bulaev, Prof. J. Carlos Egues, Dr. Simon Gardiner, Vitaly N. Golovach, Prof. Bert Hecht, Alexander Högele, Dr. Alexander Holleitner, Prof. Atac Imamoğlu, Senta Karotke, Prof. Alexander V. Khaetskii, Prof. Jörg P. Kotthaus, Dr. Wayne Lau, Dr. Michael N. Leuenberger, Prof. Min Ouyang, Prof. Pierre M. Petroff, Prof. Dieter Pohl, Prof. Patrik Recher, Dr. Daniel S. Saraga, Holger Schaefers, and Dr. Wilfred G. van der Wiel. Many helpful suggestions to the text have been made by Dr. Olivier Merlo, Dr. Hanno Gassmann, Bill Coish, and Dr. Florian Meier. I would also like to thank my present and former office mates Massoud Borhani, Dr. Olivier Merlo, and Prof. Patrik Recher for the pleasant atmosphere we have always had in our office and for many entertaining discussions on scientific and non-scientific topics. On the non-scientific side I would especially like to thank Dr. Hanno Gassmann for organizing various activities and Massoud Borhani and Dr. Oleg Chalaev for providing enormous amounts of delicious Iranian and Italo-Russian pastry for our coffee breaks.

I would like to thank Prof. David D. Awschalom for co-refereeing this thesis and Prof. Dirk Trautmann for agreeing to chair the defense.

Finally, I cordially thank my family for their continuous support.

Summary

The interaction of electrons and photons lies at the heart of quantum physics. The most notable phenomena which are described by quantum physics but which obviously invalidate a classical description of the electromagnetic field—the photoelectric effect, the Compton effect, or the antibunching of photons emitted from a single atom, to mention a few—are intimately related to the interaction of electrons and photons.

Electrons possess an internal degree of freedom, the spin. The spin $\mathbf{S}$ of an electron can be described as an internal angular momentum, leading to a magnetic moment $\mathbf{m}$ due to the electric charge of the electron. Stern and Gerlach have shown that the projection of $\mathbf{m}$ onto a quantization axis (defined by an external magnetic field in their experiment), e.g., along the z axis, is either $m_z = g\mu_\mathrm{B}/2$ ("spin up") or $m_z = -g\mu_\mathrm{B}/2$ ("spin down"), where $\mu_\mathrm{B} \approx 9.2741 \cdot 10^{-24}\,\mathrm{J/T}$ is the Bohr magneton and g is the g-factor of the electron ($g = 2$ for free electrons). An electron spin is therefore usually referred to as a two-level system. Due to this property, the spin of electrons which are localized in semiconductor quantum dots has recently attracted significant attention regarding the implementation of quantum information processing: Electron spins can be used as carriers of quantum information. One can define that the spin pointing "up" corresponds to the logical value "0" and the spin pointing "down" corresponds to "1". Moreover, because the electron spin is a quantum mechanical property one can form arbitrary coherent superpositions of "up" and "down" with a single spin. A system with this property is called a quantum bit (qubit). The additional possibilities due to quantum superpositions of qubits are exploited, e.g., in the algorithms introduced by Shor and Grover to solve certain tasks much more efficiently than with a classical computer (i.e., the prime factorization of large numbers for Shor's algorithm and the search within an unstructured database for Grover's algorithm). While quantum computation has presently only been achieved in prototypical experiments with few qubits, the implementation of efficient large-scale quantum computation with many qubits still remains an extremely demanding task. Yet, other quantum mechanical properties of qubits, such as entanglement, have already been exploited experimentally with photons in quantum communication schemes, for example, quantum teleportation and quantum data compression.

In this thesis, we investigate the interaction of electrons and photons in semiconductor quantum dots. Optical transitions in quantum dots enable a direct link between electron spins and photon polarizations due to conservation laws. We show that

entanglement can be transferred from electron spin qubits to qubits defined by the photon polarization, enabling the measurement of entangled spin states via photons. The mechanism under study can also be used for the production of entangled photons, for instance for the implementation of quantum communication protocols. In contrast to the presently used sources of entangled photons, the photon source we propose here is deterministic, providing entangled photons on demand. It has been demonstrated in several recent experiments that the most obvious way to achieve such a transfer of entanglement—using the recombination of biexcitons in a single quantum dot—fails in the presently available quantum dot structures. We have analyzed the problems of this approach. As a solution, we propose schemes based on charged excitons in single or coupled quantum dots. We discuss the generation of entangled two- and four-photon states.

In addition to the transfer of quantum states, photons can also be used to probe electron spin states. We investigate in detail different methods to optically measure the decoherence time of a single electron spin in a quantum dot. The decoherence time of a spin establishes the time scale during which coherent manipulation is possible. Measurements of the electron spin decoherence time are therefore highly desirable in view of the implementation of spin-based quantum information processing. We show that the schemes we propose can be implemented with current experimental techniques.

We then study the magneto-optical effect called Faraday rotation. Using the technique of time-resolved Faraday rotation, a recent experiment has demonstrated the coherent transfer of spin between quantum dots coupled by molecules. We calculate the Faraday rotation signal for a coupled dot system and show that a two-site Hamiltonian with a transfer term captures the essential features observed in this experiment. We also present results for a system of two coupled dots doped with a single electron.

We finally show that the coupled states of two qubits can be detected via the optical interaction with a cavity in the dispersive regime. We present a Schrieffer-Wolff transformation which removes the coupling of the two qubits to the cavity in leading order. The different two-qubit states lead to a different spectral shift of the cavity line. For a sufficiently low cavity linewidth, this enables the direct readout of a two-qubit system.

Zusammenfassung

Die Wechselwirkung von Elektronen und Photonen ist von zentraler Bedeutung für die Quantenphysik. Die wahrscheinlich berühmtesten Phänomene, welche von der Quantenphysik korrekt beschrieben werden, sich aber einer Beschreibung mit einem klassischen elektromagnetischen Felde vollständig entziehen—beispielsweise der photoelektrische Effekt, der Compton-Effekt, oder das "Antibunching" von Photonen, welche von einem einzelnen Atom emittiert werden, um nur ein paar zu nennen—sind direkt mit der Wechselwirkung von Elektronen und Photonen verbunden.

Elektronen besitzen einen inneren Freiheitsgrad, den Spin. Der Spin $\mathbf{S}$ eines Elektrons kann als innerer Drehimpuls beschrieben werden, welcher aufgrund der elektrischen Ladung des Elektrons zu einem magnetischen Moment $\mathbf{m}$ führt. Das Experiment von Stern und Gerlach bewies, dass die Projektion von $\mathbf{m}$ auf eine Quantisierungsachse (welche im Experiment durch ein äusseres Magnetfeld gegeben war), zum Beispiel z, entweder den Wert $m_z = g\mu_\mathrm{B}/2$ ("spin up") oder den Wert $m_z = -g\mu_\mathrm{B}/2$ ("spin down") annimmt, wobei $\mu_\mathrm{B} \approx 9.2741 \cdot 10^{-24}\,\mathrm{J/T}$ das Bohrsche Magneton ist und g der gyromagnetische Faktor des Elektrons ($g = 2$ für das freie Elektron). Ein Elektronenspin wird daher auch als ein Zwei-Niveau-System bezeichnet. Aufgrund dieser Eigenschaft hat der Spin von Elektronen, welche in Halbleiter-Quantenpunkten lokalisiert sind, grosse Aufmerksamkeit erregt hinsichtlich der Verarbeitung von Quanteninformation: Elektronenspins können als Träger von Quanteninformation benutzt werden. Dem "spin up"-Zustand kann der logische Wert "0" zugeordnet werden, sowie dem "spin down"-Zustand der logische Wert "1". Darüberhinaus können beliebige kohärente Superpositionen dieser beiden Zustände mit einem einzelnen Spin gebildet werden, da es sich beim Spin um eine quantenmechanische Grösse handelt. Ein System mit dieser Eigenschaft wird auch Quantenbit oder Qubit genannt. Das zusätzliche Potential von Qubits, das sich durch die Möglichkeit der quantenmechanischen Superposition eröffnet, wird beispielsweise im Algorithmus von Shor oder im Algorithmus von Grover ausgenutzt, um bestimmte Aufgaben schneller zu lösen als es ein herkömmlicher klassischer Computer vermag. Im Falle des Shor-Algorithmus ist dies die Primfaktorzerlegung grosser Zahlen, während der Grover-Algorithmus eine Suche in einer nicht geordneten Datenbasis durchführt. Während solches "Quantencomputing" zur Zeit erst in prototypenhaften Experimenten und erst mit wenigen Qubits durchgeführt wurde, bleibt die Verwirklichung von effizientem und umfangreichem "Quantencomputing" mit vielen Qubits eine äusserst schwierige Aufgabe. Aller-

dings wurden auch schon weitere quantenmechanische Eigenschaften von Qubits, zum Beispiel Verschränkung, in Experimenten mit Photonen verwendet zur Implementierung von Schemen der Quantenkommunikation, beispielsweise Quantenteleportation und Quanten-Datenkompression.

In dieser Dissertation ist die Wechselwirkung von Elektronen und Photonen in Halbleiter-Quantenpunkten der Gegenstand der Untersuchung. Optische Übergänge in Quantenpunkten ermöglichen eine direkte Verknüpfung des Elektronenspins mit der Polarisation des Photons aufgrund der Erhaltungssätze. Wir zeigen, dass Verschränkung von Elektronenspins auf die Polarisation von Photonen transferiert werden kann, was die Messung von verschränkten Spinzuständen ermöglicht. Der hier untersuchte Mechanismus kann ebenfalls zur Herstellung von verschränkten Photonen benutzt werden, beispielsweise zur Implementierung von Protokollen der Quantenkommunikation. Im Gegensatz zu den momentan weit verbreiteten Quellen von verschränkten Photonen ist die Photonenquelle welche wir hier vorschlagen deterministisch, d.h. es können quasi "auf Knopfdruck" verschränkte Photonen emittiert werden. In zahlreichen Experimenten wurde es kürzlich gezeigt, dass die naheliegendste Art dies zu erreichen—durch die Rekombination eines Biexzitons in einem einzelnen Quantenpunkt—in den momentan verfügbaren Quantenpunktstrukturen versagt. Wir haben die diesem Befund zugrunde liegenden Ursachen analysiert. Als Lösung schlagen wir die Verwendung von geladenen Exzitonen in einzelnen oder gekoppelten Quantenpunkten vor. Wir diskutieren die Produktion von verschränkten Zwei- und Vier-Photonenzuständen.

Zusätzlich zu dem Transfer von Quantenzuständen können Photonen auch zur Messung von Elektronenspinzuständen benutzt werden. Wir untersuchen hier im Detail verschiedene Methoden zur optischen Messung der Spin-Dekohärenzzeit eines einzelnen Elektrons in einem Quantenpunkt. Die Spin-Dekohärenzzeit legt die Zeitskala fest, auf welcher kohärente Manipulation des Spins möglich ist. Die Messung der Spin-Dekohärenzzeit eines einzelnen Elektrons ist daher von grossem Interesse hinsichtlich der Implementierung von spin-basierter Verarbeitung von Quanteninformation. Wir zeigen, dass die von uns vorgeschlagenen Methoden mit bereits heute verfügbaren experimentellen Techniken durchgeführt werden können.

Wir untersuchen anschliessend den magneto-optischen Effekt der Faraday-Rotation. Anhand der Technik von zeitaufgelöster Faraday-Rotation hat ein Experiment neulich kohärenten Spintransfer zwischen molekular gekoppelten Quantenpunkten aufgezeigt. Wir berechnen das Faraday-Rotationssignal für ein System von gekoppelten Quantenpunkten und zeigen, dass ein Hamilton-Operator mit einem Transferterm zwischen zwei Punkten die wesentlichen Befunde des Experimentes reproduziert. Wir präsentieren auch Resultate für ein System von zwei gekoppelten Quantenpunkten, welches mit einem zusätzlichen Elektron geladen ist.

Schlussendlich zeigen wir, dass die gekoppelten Zustände zweier Qubits über die optische Wechselwirkung mit einer Kavität im dispersiven Regime detektiert werden können. Wir beschreiben eine Schrieffer-Wolff-Transformation, welche die Kopplung

der zwei Qubits mit der Kavität in führender Ordnung entfernt. Die verschiedenen Zwei-Qubit-Zustände führen zu einer unterschiedlichen spektralen Verschiebung der Kavitätslinie. Für eine hinreichend scharfe Kavitätslinie ermöglicht dies das direkte Auslesen eines Zwei-Qubit-Zustandes.

Contents

Chapter 1

Introduction

During the last years, a new branch of electronic technology that benefits from the usage of the spin degree of freedom of the electron (or other charge carriers) has attracted a lot of attention in solid-state physics [1, 2]. This branch of electronics is called spintronics. The giant magnetoresistance (GMR) effect [3, 4] has led to a major breakthrough for spintronics: Only a few years after the detection of GMR, industry has started the commercial production of hard-disk read and write heads based on GMR, which has sparked large interest in the research on spintronics. In addition to metals and magnetic materials, significant research efforts are currently dedicated to semiconductor spintronic devices. Spin-related phenomena in semiconductors are interesting from a fundamental point of view. For example, spin can be transported in spin currents, analogous to electrical currents for the charge. Many interesting effects arise due to the coupling of spin and charge, which is mediated by the spin-orbit interaction in semiconductors. An example of such an effect is the recently observed spin Hall effect in semiconductor films, where a spin current flows transverse to an electric field even if no external magnetic field is applied [5]. This effect has been named in analogy to the conventional Hall effect (which is not related to spin), where an electric current in the presence of a magnetic field acquires a non-zero transverse component due to the Lorentz force, giving rise to a transverse Hall voltage. Spin-dependent effects in semiconductors also promise new commercially interesting applications that can be integrated into standard electronic circuits. To mention one important proposal, Datta and Das [6] proposed a transistor which enables the electrical switching of electron spin states using the spin-orbit interaction in semiconductors.

Many important branches of technology are related to photons, the quanta of the electromagnetic field. Photons are only weakly interacting with their environment and propagate very quickly, namely with velocity $v = c/n$ in a material with refractive index n, where $c \approx 2.998 \cdot 10^8\,\mathrm{m/s}$ is the vacuum speed of light and typically $n \sim 1$ for transparent materials. Using fiber optics, photons can also be directed along arbitrary paths. Due to such properties, photons are well suited for applications in

high-speed and long-distance communication, as well as in information technology. Furthermore, entire photonic circuits can in principle be constructed, where photons are the carriers of information, similar to the electrons in electronics. A high level of control on photon states has been reached with the development of many innovative laser techniques, e.g., the generation of ultrafast laser pulses with pulse lengths as short as femtoseconds. Such laser techniques have enabled an enormous number of experiments exploring the interaction of light and matter, bringing the field of quantum optics, and especially also semiconductor optics, to bloom.

Spins in semiconductors can be detected and manipulated with photons. On a microscopic level, spin polarization can be converted into photon polarization and vice versa because of the selection rules for optical transitions, establishing a link between spintronics and photonics. Moreover, magneto-optical effects such as the Faraday rotation, for instance, provide novel mechanisms for spin detection, including–in principle– quantum non-demolition measurements of single spins.

1.1 Spins and photons as quantum bits

A spin 1/2 is a generic two-level system which can be used to define a logical bit. One can define that the spin pointing "up", $|\uparrow\rangle$, corresponds to the logical value "0", whereas the spin pointing "down", $|\downarrow\rangle$, is attributed to the logical value "1". Thus, one (classical) bit of information can be encoded into a spin 1/2. But this is not yet the full potential of spin-based information storage. The dynamics of a spin 1/2 is governed by the laws of quantum mechanics. It is therefore possible to create an arbitrary *coherent superposition* $\alpha|\uparrow\rangle + \beta|\downarrow\rangle$ of the spin states $|\uparrow\rangle$ and $|\downarrow\rangle$, where the complex numbers α and β satisfy $|\alpha|^2+|\beta|^2 = 1$. A two-level system with this property is called a quantum bit (qubit). For qubits, algorithms have been discovered which solve certain problems much more efficiently than classical algorithms, exploiting the *coherent* dynamics of qubits for computation [7, 8]. This type of computation is referred to as quantum computation. From the discussion above we conclude that a spin 1/2 represents a natural candidate for a qubit [9]. Based on this intrinsic property of spin-1/2 systems, Loss and DiVincenzo proposed to use electron spins localized in quantum dots for the implementation of quantum computation [11, 9]. Quantum dots are structures which provide electron confinement in three spatial dimensions, see Section 1.3 for a more detailed discussion. Since the proposal by Loss and DiVincenzo, an impressive number of proposals for spin-based quantum computation has been published in the literature. For a recent review article, see Ref. [10].

An electron spin in the solid state is interacting with its environment. This interaction leads to dissipative effects for the spin which can be described in the frame of a system–reservoir approach. In this approach, an effective dynamics is derived for the spin system by tracing over the degrees of freedom of the reservoir, and one can define

lifetimes for the spin. For spins which are used as qubits, the spin lifetime limits the time during which quantum information can be processed. For single spins, one distinguishes between the two characteristic decay times T_1 and T_2. The relaxation of an excited spin state in a static magnetic field into the thermal equilibrium occurs with the spin relaxation time T_1, whereas the spin decoherence time T_2 is associated with the loss of phase coherence of a single spin that is prepared in a coherent superposition of its eigenstates. See Section 2.2 for a more detailed discussion of spin relaxation and decoherence. It is remarkable that the electron spin is only weakly interacting with its environment in many semiconductor systems, due to a rather weak coupling of the spin and orbital degrees of freedom. A series of ground-breaking experiments has given clear evidence for amazingly long spin lifetimes in semiconductors [12, 9]. Spin decoherence times in n-doped semiconductors have been shown to be on the order of nanoseconds up to room temperature [13], and even on the order of one hundred nanoseconds in n-doped GaAs at cryogenic temperatures [14]. Further, coherent transport of electron spins in semiconductors has been demonstrated over distances exceeding one hundred micrometers [15], nourishing hopes that the electron spin may be used as carrier of information, similar to the electron charge. Recently, expectations for the stability of spin qubits in quantum dots have also grown considerably as progressively longer spin lifetimes have been reported. A series of works on electron spin relaxation in quantum dots started with a reported triplet-to-singlet relaxation time of $\tau_{\mathrm{S-T}} = 200\,\mu$s [16]. Several groups have since measured T_1 for single electron spins. For electrostatically-defined GaAs dots, a lower bound $T_1 \gtrsim 50\,\mu$s has been measured at a magnetic field of $B = 7.5$ T [17] which was subsequently topped with $T_1 \approx (0.85 \pm 0.11)$ ms at $B = 8$ T [18]. For In(Ga)As self-assembled dots, a lower bound $T_1 \gtrsim 20$ ms at $T = 1$ K and $B = 4$ T has been established [19]. The larger level spacing of self-assembled dots (compared to gated GaAs dots) is responsible for the longer T_1-time seen in this experiment (which is limited by spin-orbit coupling). Recently, a lower bound $\tau_{\mathrm{S-T}} \geq 70\,\mu$s has been reported for the triplet-singlet relaxation time in electrostatically defined dots [20], and $\tau_{\mathrm{S-T}} = (2.58 \pm 0.09)$ ms has been measured independently, using a novel spin readout technique [21]. Spin coherence in quantum dots has also been studied already and has been shown to persist during at least on the order of hundreds of picoseconds [22, 23, 24]. Recently, a decoherence time $T_2 \approx 16$ ns of a single electron spin has been measured in GaAs quantum dots [25]. These and also other experiments suggest that the processing of quantum information encoded in spins in semiconductors is nowadays within experimental reach. For a further discussion of electron spin coherence in quantum dots see Section 4.1.

Another generic two-level system is the polarization of a photon. In the basis of circular polarization, the two basis states are the left- and the right-hand circular polarization, whereas in the basis of linear polarization the two basis states can be chosen along two orthogonal directions, e.g., in horizontal and vertical direction. Photons are capable of carrying quantum information encoded in their polarization. In stark contrast to their solid-state counterparts, photonic qubits exhibit an exemplary phase coherence because they can efficiently be protected from interactions with their

environment. Similarly to electrons, one can also define other types of qubits based on photons, for example using two photon number states or two distinct modes. In the following, we focus on photon qubits defined in terms of the photon polarization.

A qubit that is encoded in the photon polarization is closely related to an electron spin qubit via optical transitions in semiconductor quantum dots. For many applications it is desirable to combine the complementary qualities of electron spins and photons we have described above. In view of quantum information schemes, converting spin into photon quantum states corresponds to a conversion of localized into flying qubits, which can be transmitted over long distances and could overcome limitations caused by the short-range nature of the electron exchange interaction [9]. On a more fundamental level, the photon polarization can be readily measured experimentally such that an interface between spins and photons will allow one to measure quantum properties of the spin system via the photons generated on recombination. Among such quantum properties, entanglement is of particular importance.

1.2 Entanglement

The entanglement of qubits is a crucial resource for both quantum computation and quantum communication. Quantum communication comprises schemes, for instance, for the faithful transmission of a quantum state ("quantum teleportation"), to produce a secure cryptographic key ("quantum key distribution"), or to enhance classical communication (e.g., with "quantum superdense coding") using entangled qubits [7, 8]. Entanglement is a purely quantum mechanical phenomenon without a classical analogue. Two particles are entangled if their wave function can not be written as a tensor product of two single-particle wave functions. This property is a direct consequence of the superposition principle of quantum mechanics. For example, it follows directly from the Pauli principle that two electrons in the same orbital state (which we assume to be only degenerate for the spin quantum number) form a spin-entangled state, namely, a spin singlet $|\Psi^-\rangle = (|\uparrow\rangle_1|\downarrow\rangle_2 - |\downarrow\rangle_1|\uparrow\rangle_2)/\sqrt{2}$, where $|S_z\rangle_i$ is the spin state $S_z = \uparrow, \downarrow$ of particle i. Further, interaction between two systems leads often to a ground state where the two systems are entangled. Entanglement is therefore almost a ubiquitous phenomenon in atomic physics and especially also in solid-state physics.

If entangled particles are spatially separated, nonlocal correlations of the particles exist according to quantum theory. In order to test quantum mechanics versus the principle of local causes in such experimental setups, John Bell has formulated a set of inequalities [26, 27]. However, the direct detection of entanglement in solid-state systems is in general enormously difficult because there are many possible types of interaction which may perturb a measurement. It is also usually difficult to measure individual particles in a solid-state environment.

For photons the situation is fundamentally different than for electrons. In vacuum or in air, photons are practically non-interacting for the low radiation intensities that

are usually produced in the laboratory (except for the case of high-energy physics). Nevertheless, entanglement can be transferred from an emitter system to photons upon optical recombination, as we discuss in Chapters 2 and 3. For example, photon entanglement can be generated in emission cascades where decay paths with different polarizations interfere quantum mechanically [28]. Such photon entanglement due to atomic cascades has been demonstrated by several experimental violations of Bell's inequalities [29, 30, 31]. In these experiments, an atomic *s*-*p*-*s* emission cascade has been studied, giving rise to the emission of two photons that are entangled in polarization. Subsequently, parametric down-conversion has been exploited for the production of entangled photons [32]. In particular, type-II parametric down-conversion has evolved as a widely used method to produce polarization-entangled photons [33]. In type-II parametric down-conversion, a photon from an intense light source decays spontaneously in an optically nonlinear medium (typically a beta-barium-borate (BBO) crystal) into two daughter photons of lower frequency that are emitted along the directions of two cones of ordinary and of extraordinary polarization, respectively. The conservation laws for energy and momentum induce strong correlations among the daughter photons. One can adjust the experimental setup such that the two emission cones intersect. Two photons that are emitted at the two intersection points, respectively, are entangled in polarization [33]. In addition to the production of pairs of entangled photons, parametric down-conversion has also been used for the production of entangled three- [34] and four-photon [35] states of the Greenberger-Horne-Zeilinger (GHZ) type. Such entangled multiphoton states are an essential ingredient of multiparty quantum communication schemes [36].

In spite of the many successful demonstrations of the production of entangled photons, e.g., in experimental quantum teleportation [37, 38], there are two major shortcomings of parametric down-conversion: the efficiency is low and the process is intrinsically stochastic. For efficient processing and transmission of quantum information, a deterministic source of entangled photons is highly desirable, producing entangled photon pairs on demand. In Section 1.3, we show that the goal of an efficient and deterministic source of entangled photons could be realized using solid-state systems, especially, semiconductor quantum dots.

1.3 Semiconductor quantum dots

In this thesis, we discuss the interaction of semiconductor quantum dots and the electromagnetic field with a special focus on spin-related effects and entanglement. We show that spin-entangled electrons can be used for the production of polarization-entangled photons. Further, we investigate the optical detection of electron spin decoherence in quantum dots and the magneto-optical properties of coupled quantum dots. Quantum dots provide confinement in three spatial dimensions and have a size that can range from a few nanometers up to one hundred nanometers, which is comparable to the de Broglie wavelength of electrons in semiconductors. Quantum

dots therefore provide well-separated discrete levels for electronic states with a typical level spacing of several meV. Due to this property, quantum dots are sometimes referred to as artificial atoms [39] (even though they usually contain hundreds of thousands of real atoms). In the following, we consider quantum dots that confine conduction-band electrons as well as valence-band holes. These quantum dots are referred to as type I quantum dots. Such quantum dots are particularly interesting for optical investigations because of their good coupling to photons. See Sections 2.4, 2.5, and 3.4 for a microscopic discussion of the optical properties of quantum dots. In contrast, in type II quantum dots only one type of charge carrier is confined and the other type is repelled. In such systems (e.g., electrostatically defined quantum dots), the optical transition rates are significantly reduced because of the small overlap of electron and hole wave functions. Several techniques have been developed for the fabrication of quantum dots, e.g., etching of a quantum well [40]. Quantum dots also form "naturally" at monolayer steps at the interface of, e.g., thin GaAs/AlGaAs quantum wells [41, 42]. Usually, molecular beam epitaxy (MBE) is used for the growth of such systems. If the MBE growth process is performed without interruption, such steps occur at random positions as natural fluctuations of the quantum well width. Quantum dots of this type possess excellent optical properties, including very sharp optical linewidths. Coherent control of optically excited states has been achieved for such quantum dot structures [43, 44], culminating in the recent implementation of a CROT gate for qubits which were defined by the presence or absence of an optically excited electron-hole pair (exciton) in the dot [45]. Further, quantum dot structures can be grown by self-assembly, e.g., using the Stranski-Krastanov growth technique. In this technique, self-assembled dot islands form spontaneously during epitaxial growth due to a lattice mismatch between the dot and the substrate material [46]. Small self-assembled dots typically have a pyramidal shape with four facets, whereas larger dots (containing, e.g., 7 monolayers of InAs) form multi-faceted domes [47]. If pyramidal self-assembled dots are covered with a thin layer of the substrate material (called the capping layer), the capped dots take-on an elliptical (sometimes even a circular) shape. We do not restrict our analysis to a specific kind of type I quantum dot in the following. Rather, our goal is to provide theoretical studies based on simple models that cover the relevant low-energy physics of the class of typical type I quantum dot systems. For the quantum dots mentioned above, the quantum confinement along the growth direction (e.g., [001]) is typically much stronger than in the plane perpendicular to it. For low temperatures it is then usually a good approximation to only take the lowest subband of the quantization along [001] into account and make a quasi two-dimensional ansatz for the quantum dot confinement potential [48]. We continue this discussion in Section 2.4.4.

1.3.1 Quantum dot photon sources

In addition to the conversion of spin into photon polarization, semiconductor quantum dots have recently attracted a lot of attention as non-classical light sources. Sin-

gle quantum dots have been proposed as single-photon sources [49], and this purely quantum mechanical emission property has been demonstrated subsequently in several experiments [50, 51, 52, 53, 54, 55]. Recently, quantum cryptography [56] and quantum teleportation [57] have been demonstrated with quantum dot single-photon sources. Single photons can be produced by the recombination of single excitons in quantum dots. The production rate of such quantum dot single-photon sources has an upper limit given by the inverse exciton lifetime, which is typically $\sim 1/(1\,\mathrm{ns})$. Single photons can be created deterministically by pulsed carrier injection into the dots (via laser pulses or by switching external gate voltages). Electrons and holes can be stored for very long times (several milliseconds [19], or even seconds [58]) in different locations before they are brought into the same dot for recombination. As soon as more than one electron-hole pair are present in the dot, e.g., two (forming a so-called biexciton), the energy of the first emitted photon is shifted with respect to the second photon due to the different Coulomb interaction energies of the exciton and the biexciton. The collection of the emission of a single excitonic line of a single quantum dot is therefore sufficient to obtain single photons. Further, excitation of *single* excitons in the dot can be achieved by electrical injection of single electrons and single holes, via cw laser excitation with sufficiently low intensity, or via optical π-pulses, as the recent demonstrations of exciton Rabi oscillations have shown [59, 60, 61, 62].

As an extension of the scheme for single-photon generation, the decay cascade of ground-state biexcitons has been proposed as a mechanism for the deterministic production of pairs of polarization-entangled photons in single quantum dots [63]. The photon pair emitted during the biexciton decay cascade is entangled in polarization due to the spin entanglement of the biexciton ground state, which is transferred to the photons via optical selection rules. For optical injection of the biexciton, the conversion efficiency of entangled photon pair per pump photon has been estimated to be four orders of magnitude larger than for parametric down-conversion [64]. However, such entanglement has not been observed up to present in InAs [65, 66, 67, 68] and CdSe [69] quantum dots. It is believed that the electron-hole exchange interaction in asymmetric quantum dots is responsible for the observed lack of entanglement. We discuss this issue in Chapter 2.

1.4 Outline

This thesis is organized as follows. In Chapter 2 we discuss the transfer of entanglement from electron spins to photons using spin-LEDs which contain semiconductor quantum dots as the optically active medium. We show that nonlocal spin-entangled electron pairs that recombine in spatially separated spin-LEDs are converted into polarization-entangled photon pairs. Such a setup could be used to test the performance of devices which produce spin-entangled electrons. We start with a discussion of spin relaxation and decoherence. We then discuss optical properties of quantum dots and describe the production of entangled four- and two-photon states using spin-LEDs. The implications of the electron-hole exchange interaction in asymmetric quantum dots is reviewed. After discussing the fine structure of positively charged excitons we show that entangled two-photon states can be produced even with asymmetric quantum dots using positively charged excitons. We discuss the dependence of the polarization entanglement on the emission directions of the photons.

In Chapter 3 we specialize to a setup consisting of two tunnel-coupled quantum dots. We calculate the low-lying energies of a biexciton in the double dot and discuss the production of entangled photons with this setup. For two positively charged excitons instead of two (neutral) excitons, we show that the schemes for the generation of entangled photons discussed in Chapter 2 can also be realized using such a double quantum dot. With this respect, the two-electron ground state of the double dot provides the necessary spin entanglement which is transferred to the photons. We further study the optical properties of coupled quantum dots in terms of the oscillator strength.

In Chapter 4 we propose to apply optical detection of magnetic resonance to measure the decoherence time T_2 of a single electron spin in a quantum dot. Spin-dependent absorption due to Pauli blocking in the electron level enables the detection of electron spin resonance in such a setup. We show that relaxation of the total angular momentum of valence-band holes leads to a polarization of the electron spin, similarly as in an optical pumping scheme. For quick hole spin relaxation the efficiency of the discussed electron spin decoherence measurement is increased. We also discuss additional optical methods to measure T_2 or, alternatively, the spin relaxation time T_1.

In Chapter 5 we present a model that describes coherent spin transfer between molecularly coupled quantum dots, motivated by a recent experiment [70]. We calculate the Faraday rotation signal for such a system and obtain results that are in good agreement with the experiment. We also provide results for the Faraday rotation of two coupled dots that are initially charged with one excess electron.

Finally, in Chapter 6 we study a model for two coupled qubits which additionally interact with a single cavity mode. We show that the cavity mode dispersion allows one to measure the state of the coupled-qubit system in the dispersive regime.

Chapter 2

Entanglement transfer from electron spins to photons

We show that non-local spin-entangled electron pairs that recombine in spatially separated spin light-emitting diodes (spin-LEDs) are converted into polarization-entangled photons [71]. In Section 2.1 we introduce the building blocks of the setup under theoretical study. In Section 2.2 we describe the time evolution of an entangled two-electron state, where the two electrons are subject to different environments, leading to spin relaxation and decoherence. The dynamics of the entire conversion process is modelled in Section 2.3. We discuss the interaction of light and matter as well as optical properties of quantum dots in Section 2.4 and derive microscopic expressions for the optical transitions in quantum dots in Section 2.5. In Section 2.6 we show that entangled four-photon states can be produced deterministically with an electron entangler and symmetric quantum dots charged with two valence-band holes for optical recombination. In Section 2.7 the electron-hole exchange interaction is discussed. Subsequently, in Section 2.8 we discuss the effect of the electron-hole exchange interaction on positively charged excitons (which are relevant for the emission of the first two photons in our scheme). We show in Section 2.9 that it is possible to avoid the loss of photon entanglement encountered for the decay cascade of a biexciton in single quantum dots [65, 66, 67, 68, 69] by providing entangled electrons that recombine in two separate quantum dots with two holes per dot. Namely, a maximally entangled two-photon state can be extracted from the four-photon state by a measurement of the third and the fourth photon or an equivalent measurement of the hole spins. In Section 2.10 we study the dependence of the photon entanglement on the photon emission directions and we conclude in Section 2.11.

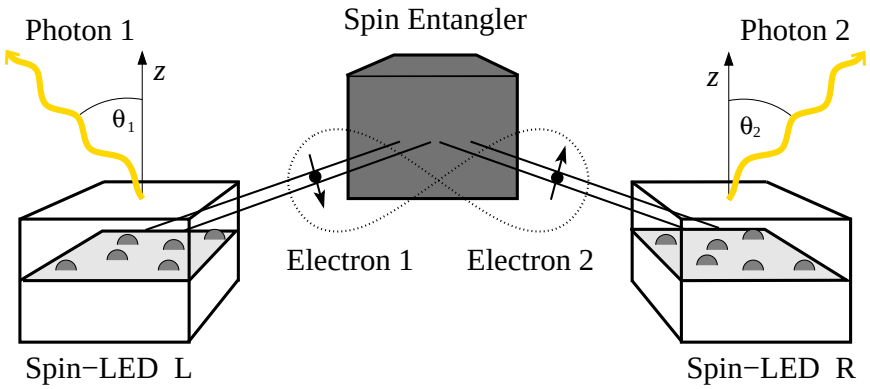

Figure 2.1: Schematic setup for the transfer of entanglement between electrons and photons. An electron entangler (gray box) injects a pair of spin-entangled electrons into two current leads. The electrons then recombine individually in one of the quantum dots located in the left (L) or the right (R) spin-LED and give rise to the emission of two photons.

2.1 Setup

The system under study, shown schematically in Figure 2.1, relies on an entangler as a source of spin-entangled electron pairs. Several schemes have been proposed that provide such pairs of spin-entangled electrons. For instance, two electrons in the orbital ground state of a double dot form a spin singlet at low magnetic fields [72, 73, 74]. Due to the Coulomb repulsion, there is only one electron per dot and the entangled pair of electrons can be injected into two adjacent current leads by applying a voltage across the dot structure. Alternatively, the two electrons of the ground-state singlet of a single quantum dot can be separated using tunneling into two adjacent quantum dots in the Coulomb blockade regime if sequential tunneling of single electrons is the dominant transport channel [75]. Another source of electron singlets are the Cooper pairs of an s-wave superconductor [76, 77, 78, 79, 80]. The two spin-entangled electrons of a Cooper pair can be separated by Andreev tunneling into two quantum dots in the Coulomb blockade regime [76], by tunneling into two Luttinger liquid leads [78, 79, 80], or by dynamical Coulomb blockade of the tunneling process into a normal lead [81]. Yet another proposal for an electron spin entangler is based on electron-electron scattering in a two-dimensional electron system [82]. For a scattering angle $\pi/2$, the two scattered electrons form a spin singlet. In the setup shown in Figure 2.1, the two spin-entangled electrons are injected from the output leads of the entangler into two spin-LEDs (denoted by L and R) where they recombine under photon emission.

Spin-LEDs [83, 84, 85, 86, 87, 88, 9, 19], in which electron recombination is accompanied by the emission of a photon with well-defined circular polarization, provide an efficient interface between electron spins and photons, as we already discussed in Section 1.3. Operation of such devices at the single-photon level would allow one

to convert the quantum state of an electron encoded in its spin state into that of a photon with a wide range of possible applications. More specifically, entanglement of electron spins could be demonstrated not only in current noise [73, 89] but also by measurements of photon polarizations which allows one to test Bell's inequalities [26] without the stringent limitations posed by decoherence in a solid-state environment.

The scheme discussed here is performed with two single quantum dots located within a spin-LED, respectively. Experimental access to single quantum dots can be achieved with the well-established techniques of single-dot spectroscopy [90, 91].

2.2 Spin relaxation and decoherence

After the production of the entangled spin state, the two electron spins interact with their environments. In the presence of a magnetic field, the effect of relaxation and decoherence of the two spins due to a dissipative environment is taken into account in the frame of the single-spin Bloch equation [92],

$$\dot{\mathbf{P}}(t) = \mathbf{P} \times \mathbf{h} - R(\mathbf{P} - \mathbf{P}_\infty). \tag{2.1}$$

Here, the first term describes the precession of the spin polarization $\mathbf{P} = (\langle\sigma_x\rangle, \langle\sigma_y\rangle, \langle\sigma_z\rangle)$ due to a magnetic field B contained in $\mathbf{h} = (0, 0, h)$, where $h = g_e\mu_\mathrm{B}B$ with the effective electron g factor g_e and the Bohr magneton μ_B, and σ_i are the Pauli matrices. The second term describes the effect of relaxation and decoherence of $\mathbf{P}$ towards the equilibrium polarization $\mathbf{P}_\infty = (0, 0, \tilde{P})$, which occurs due to

$$R = \begin{pmatrix} 1/T_2 & 0 & 0 \\ 0 & 1/T_2 & 0 \\ 0 & 0 & 1/T_1 \end{pmatrix}, \tag{2.2}$$

where T_2 is the decoherence time (or transverse spin lifetime) and T_1 the relaxation time (or longitudinal spin lifetime). The single-spin Bloch equation can be written in the compact form $\dot{\mathbf{P}}(t) = -\Omega(\mathbf{P} - \mathbf{P}_\infty)$ since $\mathbf{h} \times \mathbf{P}_\infty = 0$. The solution of Eq. (2.1) is given by

$$\mathbf{P}(t) = e^{-\Omega t}\mathbf{P}(0) + (1 - e^{-\Omega t})\mathbf{P}_\infty, \tag{2.3}$$

with the components

$$\begin{aligned} P_x(t) &= P_x(0)e^{-t/T_2}\cos(ht) + P_y(0)e^{-t/T_2}\sin(ht), && \text{(2.4a)} \\ P_y(t) &= -P_x(0)e^{-t/T_2}\sin(ht) + P_y(0)e^{-t/T_2}\cos(ht), && \text{(2.4b)} \\ P_z(t) &= P_z(0)e^{-t/T_1} + \tilde{P}\left(1 - e^{-t/T_1}\right). && \text{(2.4c)} \end{aligned}$$

Given that the electrons are in different leads, they interact with different environments (during times t and t', respectively). Therefore, we consider different magnetic fields $\mathbf{h} = (0, 0, h)$ and $\mathbf{h}' = (h'\sin\beta, 0, h'\cos\beta)$, enclosing an angle β, acting each on

an individual spin, and also different relaxation and decoherence times T_1', T_2' for the second spin. We obtain for the polarization of the second spin the solution

$$\begin{aligned}
P_x'(t') &= P_x'(0)\left[\cos^2\beta e^{-t'/T_2'}\cos(h't') + \sin^2\beta e^{-t'/T_1'}\right] \\
&\quad + \cos\beta P_y'(0) e^{-t'/T_2'}\sin(h't') + \sin\beta\tilde{P}'\left(1 - e^{-t'/T_1'}\right) \\
&\quad + P_z'(0)\sin\beta\cos\beta\left[e^{-t'/T_1'} - e^{-t'/T_2'}\cos(h't')\right], \qquad (2.5a) \\
P_y'(t) &= -P_x'(0)\cos\beta e^{-t'/T_2'}\sin(h't') + P_y'(0)e^{-t'/T_2'}\cos(h't') \\
&\quad + \sin\beta P_z'(0) e^{-t'/T_2'}\sin(h't'), \qquad (2.5b) \\
P_z'(t) &= P_x'(0)\sin\beta\cos\beta\left[e^{-t'/T_1'} - e^{-t'/T_2'}\cos(h't')\right] \\
&\quad - P_y'(0)\sin\beta e^{-t'/T_2'}\sin(h't') + \tilde{P}'\cos\beta\left(1 - e^{-t'/T_1'}\right) \\
&\quad + P_z'(0)\left[\cos^2\beta e^{-t'/T_1'} + \sin^2\beta e^{-t'/T_2'}\cos(h't')\right]. \qquad (2.5c)
\end{aligned}$$

From Eq. (2.4) we readily obtain the master equation for the single-spin density matrix $\rho^{(1)}$ of the first spin, using the relations $P_x = 2\mathrm{Re}\,\rho^{(1)}_{\uparrow,\downarrow}$, $P_y = -2\mathrm{Im}\,\rho^{(1)}_{\uparrow,\downarrow}$, $P_z = \rho_\uparrow{}^{(1)} - \rho_\downarrow{}^{(1)}$, and $\rho_\uparrow{}^{(1)} + \rho_\downarrow{}^{(1)} = 1$. We proceed similarly for the second spin with Eq. (2.5) and obtain for the density matrix

$$\begin{aligned}
\rho^{(2)}_\uparrow(t',\beta) &= \frac{1}{2}\left[\rho^{(2)}_\uparrow(0) + \rho^{(2)}_\downarrow(0)\right]\left[1 + \left(1 - e^{-t'/T_1'}\right)\tilde{P}'\cos\beta\right] \\
&\quad + \mathrm{Re}\,\rho^{(2)}_{\uparrow,\downarrow}(0)\sin\beta\cos\beta\left[e^{-t'/T_1'} - e^{-t'/T_2'}\cos(h't')\right] \\
&\quad + \mathrm{Im}\,\rho^{(2)}_{\uparrow,\downarrow}(0)\sin\beta e^{-t'/T_2'}\sin(h't') + \frac{1}{2}\left[\rho^{(2)}_\uparrow(0) - \rho^{(2)}_\downarrow(0)\right] \\
&\quad \times\left[\cos^2\beta e^{-t'/T_1'} + \sin^2\beta e^{-t'/T_2'}\cos(h't')\right], \qquad (2.6a) \\
\rho^{(2)}_\downarrow(t',\beta) &= \frac{1}{2}\left[\rho^{(2)}_\uparrow(0) + \rho^{(2)}_\downarrow(0)\right]\left[1 - \left(1 - e^{-t'/T_1'}\right)\tilde{P}'\cos\beta\right] \\
&\quad - \mathrm{Re}\,\rho^{(2)}_{\uparrow,\downarrow}(0)\sin\beta\cos\beta\left[e^{-t'/T_1'} - e^{-t'/T_2'}\cos(h't')\right] \\
&\quad - \mathrm{Im}\,\rho^{(2)}_{\uparrow,\downarrow}(0)\sin\beta e^{-t'/T_2'}\sin(h't') - \frac{1}{2}\left[\rho^{(2)}_\uparrow(0) - \rho^{(2)}_\downarrow(0)\right] \\
&\quad \times\left[\cos^2\beta e^{-t'/T_1'} + \sin^2\beta e^{-t'/T_2'}\cos(h't')\right], \qquad (2.6b) \\
\rho^{(2)}_{\uparrow,\downarrow}(t',\beta) &= \frac{1}{2}\left(1 - e^{-t'/T_1'}\right)\tilde{P}'\sin\beta + \mathrm{Re}\,\rho^{(2)}_{\uparrow,\downarrow}(0)\left\{\sin^2\beta e^{-t'/T_1'}\right. \\
&\qquad \left. + \cos\beta e^{-t'/T_2'}\left[\cos\beta\cos(h't') + i\sin(h't')\right]\right\} \\
&\quad + i\,\mathrm{Im}\,\rho^{(2)}_{\uparrow,\downarrow}(0)e^{-t'/T_2'}\left[\cos(h't') + i\cos\beta\sin(h't')\right] \\
&\quad - \frac{i}{2}\left[\rho^{(2)}_\uparrow(0) - \rho^{(2)}_\downarrow(0)\right]\left(\sin\beta\cos\beta e^{-t'/T_1'}\right. \\
&\qquad \left. - \sin\beta e^{-t'/T_2'}[\cos\beta\cos(h't') - i\sin(h't')]\right). \qquad (2.6c)
\end{aligned}$$

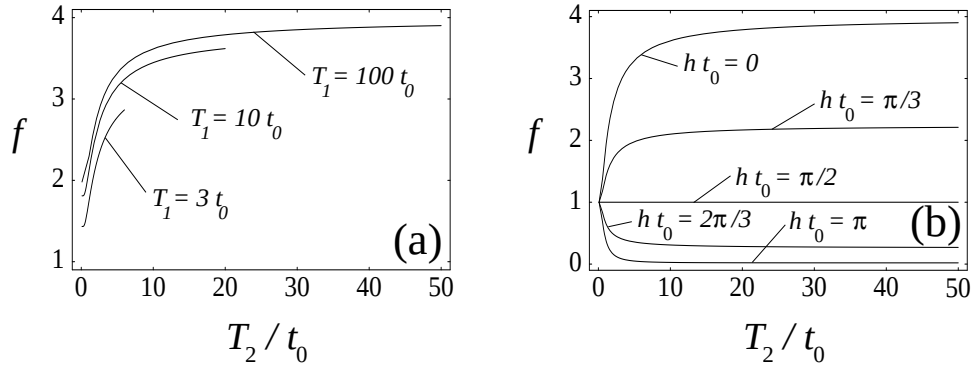

Figure 2.2: The singlet fidelity f [Eq. (2.7)] at time $t = t' = t_0$ as a function of the decoherence time T_2 in units of t_0. In (a), $\beta = 0$ and f is shown for the relaxation times $T_1 = 3t_0$, $10t_0$, $100t_0$ for $T_2 \leq 2T_1$. In (b), $\beta = \pi/2$, $T_1 = 100t_0$ and $h = h'$. f is plotted for different magnetic field strengths h (for a given t_0).

The density matrix for the first spin is obtained from above equations for $\beta = 0$ [92]. We calculate the two-spin density matrix $\chi(t,t') = \rho^{(1)}(t,0) \otimes \rho^{(2)}(t',\beta)$, and obtain for the fidelity $f = 4\langle \Psi^- | \chi(t,t') | \Psi^- \rangle$ of the singlet

$$\begin{aligned} f &= 1 - \cos\beta\, aa' \tilde{P}\tilde{P}' + e_1 \left[e_2' \sin^2\beta \cos(h't') + e_1' \cos^2\beta \right] \\ &\quad + e_2 e_1' \sin^2\beta \cos(ht) + e_2 e_2' \left[2\cos\beta \sin(ht)\sin(h't') \right. \\ &\quad \left. + \left(\cos^2\beta + 1\right) \cos(ht)\cos(h't') \right], \end{aligned} \tag{2.7}$$

where for the first (second) spin $e_i = e^{-t/T_i}$ ($e_i' = e^{-t'/T_i'}$) and $a = 1 - e_1$ ($a' = 1 - e_1'$). For $t \ll T_1, T_2$ and $t' \ll T_1', T_2'$ (in bulk GaAs $T_2 \sim 100\,\mathrm{ns}$ and typically $T_1 \gg T_2$), the electrons form a non-local spin-entangled state after their injection into the dots L and R and after their subsequent orbital relaxation to the single-electron orbital ground states $\phi_{c\alpha}(\mathbf{r}_{c\alpha}, \sigma)$. A local rotation of one of the two spins (for $\mathbf{h} \neq \mathbf{h}'$) enables a transformation of $|\Psi^-\rangle$ into another (maximally entangled) Bell state. For instance, for $\mathbf{h} \parallel \mathbf{h}'$ the singlet $|\Psi^-\rangle$ is rotated continuously into the triplet $|\Psi^+\rangle = (|\uparrow\downarrow\rangle + |\downarrow\uparrow\rangle)/\sqrt{2}$ and vice versa [92]. Further, for $\beta \neq 0$ [see Figure 2.2 (b)] the singlet can also evolve into one of the remaining Bell states $|\Phi^\pm\rangle = (|\uparrow\uparrow\rangle \pm |\downarrow\downarrow\rangle)/\sqrt{2}$. The situation with $\mathbf{h} \neq \mathbf{h}'$ can be achieved, e.g., by controlling the local Rashba spin-orbit interaction[1] in the current leads [89, 92].

In Figure 2.2, we show the fidelity f of the singlet as a function of the spin decoherence time T_2. For simplicity, we assume that the two electrons spend the same time in the current leads, $t = t' = t_0$, with $T_1' = T_1$ and $T_2' = T_2$. For a GaAs structure of length 1μm, $t_0 = v_\mathrm{F}/(1\,\mu\mathrm{m}) \approx 10 \ldots 100\,\mathrm{ps}$ for a Fermi velocity $v_\mathrm{F} \approx 10^4 \ldots 10^5 \mathrm{m/s}$

[1]The Rashba spin-orbit interaction in a quantum well is due to structure inversion asymmetry (in z direction) and is of the form $H_R = \alpha_R(p_x\sigma^y - p_y\sigma^x)/\hbar$, where p_i are the in-plane components of the electron momentum, σ^i are the Pauli spin matrices, and α_R is a coefficient that is tunable via external electric gates. For a propagating electron, H_R leads to a momentum-dependent effective magnetic field, inducing spin precession.

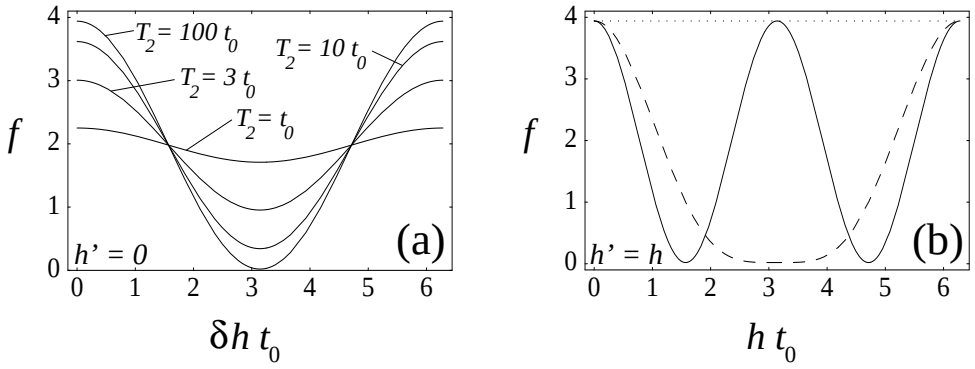

Figure 2.3: The singlet fidelity f [Eq. (2.7)] at time $t = t' = t_0$ (a) as a function of the magnetic field difference $\delta h = h - h'$ for $h' = 0$ and (b) as a function of h with $h' = h$ for different angles β. In (a), $T_1 = 100t_0$ and T_2 is as indicated in the figure. In (b), $T_1 = T_2 = 100t_0$ and $\beta = 0$ (dotted line), $\beta = \pi/2$ (dashed line), and $\beta = \pi$ (solid line).

[92]. For $T_2 = 100\,\mathrm{ns}$ we thus obtain $T_2/t_0 \approx 10^3 \ldots 10^4$. Figure 2.2 (a) shows f for different spin relaxation times T_1 and for $\beta = 0$. In Figure 2.2 (b), f is shown as a function of T_2 for $T_1 = 100t_0$, $\beta = \pi/2$, and for different strengths of the magnetic fields (assuming $h' = h$). The different limits for f that are approached for $T_2 \to \infty$ for different h and $\beta = \pi/2$ are the result of spin precession with a fixed t_0.

We show in Figure 2.3 the dependence of f on the magnetic fields $\mathbf{h}$ and $\mathbf{h}'$. For a given transmission time t_0 for both electrons, electron precession induces an oscillation of f. This oscillation is damped due to T_1 and T_2 and depends on the relative difference of the magnetic field strengths, as shown in Figure 2.3 (a) (where we consider $h' = 0$). The dependence of f on the magnetic field strengths is shown for $h' = h$ in Figure 2.3 (b) for the angles $\beta = 0$, $\pi/2$, and π.

2.3 Dynamics of the conversion process

We describe the dynamics of the electron injection and recombination in the two spin-LEDs using a master equation. The rate for the injection and the subsequent relaxation of electrons into the conduction band ground state in the dot α is denoted by $W_{e\alpha}$. It has been demonstrated that this entire process is spin-conserving and occurs much faster than the optical recombination [87, 88], which is described by the rates $W_{p\alpha}$. Typically, $W_{p\alpha} \sim 1\,\mathrm{ns}^{-1}$ and $W_{e\alpha} \sim 0.1\,\mathrm{ps}^{-1}$ for the incoherent transition rates [93, 94]. We solve the master equation for the classical occupation probabilities and obtain the probability that two photons are emitted after the injection of two electrons into the dots at $t = 0$,

$$P_{2p} = \prod_{\alpha=L,R} \frac{W_{e\alpha}(1 - e^{-tW_{p\alpha}}) - W_{p\alpha}(1 - e^{-tW_{e\alpha}})}{W_{e\alpha} - W_{p\alpha}}. \tag{2.8}$$

For $W_{p\alpha} \ll W_{e\alpha}$, $P_{2p} \approx \prod_{\alpha=L,R}(1-e^{-tW_{p\alpha}})$. After photon emission, an entangled four-photon state can be produced by subsequent injection of another pair of electrons, as we discuss in Section 2.6. Further, bipartite photon entanglement of the two emitted photons can be achieved by a measurement of the hole spins (or equivalently, of the second pair of photons) as we discuss in Section 2.9. The initial state is finally restored by injection of two holes into each of the two dots. We estimate the production rate of entangled photons in a setup to test some of the proposed electron entanglers [76, 77, 78, 79, 80, 75, 81, 82]. E.g., pairs of entangled electrons in a spin singlet state $|\Psi^-\rangle = (|\uparrow\downarrow\rangle - |\downarrow\uparrow\rangle)/\sqrt{2}$ are produced by the Andreev entangler [76] with an average time separation $\Delta t \sim 10^{-5}$s, while for the entangler based on three quantum dots [75], $\Delta t \sim 10^{-8}$s. The two spin-entangled electrons of a pair typically are injected into the current leads with a relative time delay $\tau \simeq 10^{-13}$s for both of these entanglers. Because $\tau, W_{p\alpha}^{-1} \ll \Delta t$, photons originating from a single pair of entangled electrons can be identified with high reliability. In the steady state, the generation rate of entangled photons is determined by the rate at which entangled electron pairs leave the entangler, $1/\Delta t$.

2.4 Interaction of radiation and matter

In this section we review the basics of the interaction of radiation and matter [32, 95]. We derive the interaction of a quantum-mechanical emitter with the quantized electromagnetic field, starting with the classical expression for the electromagnetic field. We then turn to semiconductors and discuss the band structure of zincblende semiconductors. To conclude the section we focus on the optical properties of semiconductor quantum dots.

We consider a system with two electronic levels $|1\rangle$ and $|2\rangle$, for example, an atom or a quantum dot, coupled to the electromagnetic field. The Hamiltonian of an electron with mass m_0 and charge e is in Gaussian units

$$H = \frac{1}{2m_0}\left[\mathbf{p} - \frac{e}{c}\mathbf{A}(\mathbf{r},t)\right]^2 + V(\mathbf{r},t) - \frac{e}{m_0 c}\mathbf{S}\cdot\mathbf{B}(\mathbf{r},t), \tag{2.9}$$

comprising the vector potential $\mathbf{A}(\mathbf{r},t)$, the magnetic field $\mathbf{B}(\mathbf{r},t)$ which couples to the electron spin $\mathbf{S}$, and an external potential $V(\mathbf{r},t)$. For simplicity, we consider a time-independent potential $V(\mathbf{r})$ which gives rise to the stationary electron states $|1\rangle$ and $|2\rangle$ under study. We choose the Coulomb (or transverse) gauge, $\mathrm{div}\mathbf{A}(\mathbf{r},t) = 0$, such that $[\hat{\mathbf{p}}, \hat{\mathbf{A}}] = 0$ for the quantum mechanical operators for the electron momentum $\hat{\mathbf{p}}$ and the quantized expression Eq. (2.18) for the vector potential which we derive below. We obtain

$$H = \frac{\mathbf{p}^2}{2m_0} + V(\mathbf{r}) - \frac{e}{m_0 c}\mathbf{A}(\mathbf{r},t)\cdot\mathbf{p} + \frac{e^2}{2m_0 c^2}\mathbf{A}^2(\mathbf{r},t) - \frac{e}{m_0 c}\mathbf{S}\cdot\mathbf{B}(\mathbf{r},t). \tag{2.10}$$

For the radiation field in vacuum, we consider a cubic volume of length L, with L much bigger than the photon wavelength λ. Then, the vector potential $\mathbf{A}(\mathbf{r},t)$ can be expanded in plane waves,

$$\mathbf{A}(\mathbf{r},t) = \frac{1}{\sqrt{\epsilon_0 L^3}} \sum_{\mathbf{k}} \mathbf{A}_{\mathbf{k}}(t)\, e^{i\mathbf{k}\cdot\mathbf{r}}, \tag{2.11}$$

with Fourier coefficients $\mathbf{A}_{\mathbf{k}}(t)$ and the dielectric constant ϵ_0. The vector $\mathbf{k}$ is discretized, $k_\alpha = 2\pi n_\alpha/L$, where $\alpha = x, y, z$ and $n_\alpha \in \mathbb{Z}$. In the Coulomb gauge, $\mathbf{A}(\mathbf{r},t)$ satisfies the homogeneous wave equation [32]

$$\nabla^2 \mathbf{A}(\mathbf{r},t) - \frac{1}{c^2}\frac{\partial^2}{\partial t^2}\mathbf{A}(\mathbf{r},t) = 0. \tag{2.12}$$

This leads to $\mathbf{A}_{\mathbf{k}}(t) = \mathbf{c}_{\mathbf{k}} \exp(-i\omega_k t) + \mathbf{c}^*_{-\mathbf{k}} \exp(i\omega_k t)$, where $\omega_k = ck$ with $k = |\mathbf{k}|$, and the asterix denotes complex conjugation. We introduce two orthogonal unit polarization vectors $\mathbf{e}_{\mathbf{k}s}$ $(s = 1, 2)$ which satisfy transversality $\mathbf{k}\cdot\mathbf{e}_{\mathbf{k}s} = 0$ $(s = 1, 2)$, orthonormality $\mathbf{e}^*_{\mathbf{k}s}\cdot\mathbf{e}_{\mathbf{k}'s'} = \delta_{ss'}\delta_{\mathbf{k}\mathbf{k}'}$, and right-handedness $\mathbf{e}_{\mathbf{k}1}\times\mathbf{e}_{\mathbf{k}2} = \mathbf{k}/k$. By definition, the unit polarization vectors $\mathbf{e}_{\mathbf{k}s}$ are parallel to the electric field vector. Two real $\mathbf{e}_{\mathbf{k}s}$ correspond to a linear polarization basis. For circular polarization, one usually chooses the complex unit polarization vectors $\mathbf{e}_{\mathbf{k}s} = (1, \pm i)/\sqrt{2}$ in the plane perpendicular to $\mathbf{k}$. Because $\mathbf{A}_{\mathbf{k}} \perp \mathbf{k}$, we can write $\mathbf{c}_{\mathbf{k}} = \sum_{s=1,2} c_{\mathbf{k}s}\mathbf{e}_{\mathbf{k}s}$. We introduce $\mathbf{e}_{\mathbf{k}s}$ in $\mathbf{A}_{\mathbf{k}}(t)$ and define the complex amplitudes $u_{\mathbf{k}s}(t) = c_{\mathbf{k}s}\exp(-i\omega_k t)$ to obtain an expansion in the fundamental vector mode functions $\mathbf{e}_{\mathbf{k}s}\exp(i\mathbf{k}\cdot\mathbf{r})$,

$$\mathbf{A}(\mathbf{r},t) = \frac{1}{\sqrt{\epsilon_0 L^3}} \sum_{\mathbf{k},s} \left(u_{\mathbf{k}s}(t)\,\mathbf{e}_{\mathbf{k}s}e^{i\mathbf{k}\cdot\mathbf{r}} + u^*_{\mathbf{k}s}(t)\,\mathbf{e}^*_{\mathbf{k}s}e^{-i\mathbf{k}\cdot\mathbf{r}}\right). \tag{2.13}$$

We finish the discussion of the classical case here and proceed to the quantization of the electromagnetic field. For this purpose, we introduce a pair of real canonical variables, $q_{\mathbf{k}s}(t) = u_{\mathbf{k}s}(t) + u^*_{\mathbf{k}s}(t)$ and $p_{\mathbf{k}s}(t) = -i\omega_k\left[u_{\mathbf{k}s}(t) - u^*_{\mathbf{k}s}(t)\right]$. The Hamiltonian of the electromagnetic field H_{f} can be derived from the expression of the field energy [32] such that, in terms of $q_{\mathbf{k}s}(t)$ and $p_{\mathbf{k}s}(t)$,

$$H_{\mathrm{f}} = \frac{1}{2}\sum_{\mathbf{k},s}\left[p^2_{\mathbf{k}s}(t) + \omega_k^2 q^2_{\mathbf{k}s}(t)\right]. \tag{2.14}$$

Thus every photon mode $\mathbf{k}$ with polarization s contributes the energy of an independent harmonic oscillator to the field. Expressed in the canonical variables $q_{\mathbf{k}s}(t)$ and $p_{\mathbf{k}s}(t)$, the vector potential reads

$$\mathbf{A}(\mathbf{r},t) = \frac{1}{2\sqrt{\epsilon_0 L^3}} \sum_{\mathbf{k},s}\left[\left(q_{\mathbf{k}s}(t) + \frac{i}{\omega_k}\,p_{\mathbf{k}s}(t)\right)\,\mathbf{e}_{\mathbf{k}s}e^{i\mathbf{k}\cdot\mathbf{r}} + c.c.\right]. \tag{2.15}$$

According to the postulates of quantum mechanics, the canonically conjugate variables $q_{\mathbf{k}s}(t)$ and $p_{\mathbf{k}s}(t)$ are replaced by operators $\hat{q}_{\mathbf{k}s}(t)$ and $\hat{p}_{\mathbf{k}s}(t)$ that satisfy the

commutation relations $[\hat{q}_{\mathbf{k}s}(t),\, \hat{p}_{\mathbf{k}'s'}(t)] = i\hbar\delta_{ss'}\delta_{\mathbf{k}\mathbf{k}'}$ and $[\hat{q}_{\mathbf{k}s}(t),\, \hat{q}_{\mathbf{k}'s'}(t)] = [\hat{p}_{\mathbf{k}s}(t),\, \hat{p}_{\mathbf{k}'s'}(t)] = 0$ for all $\mathbf{k}, \mathbf{k}', s, s'$. We now define the non-Hermitian operators

$$\hat{a}_{\mathbf{k}s}(t) = \frac{1}{\sqrt{2\hbar\omega_k}} \left[\omega_k \hat{q}_{\mathbf{k}s}(t) + i\hat{p}_{\mathbf{k}s}(t)\right] = \hat{a}_{\mathbf{k}s}(0)\, e^{-i\omega_k t}, \tag{2.16a}$$

$$\hat{a}^\dagger_{\mathbf{k}s}(t) = \frac{1}{\sqrt{2\hbar\omega_k}} \left[\omega_k \hat{q}_{\mathbf{k}s}(t) - i\hat{p}_{\mathbf{k}s}(t)\right] = \hat{a}^\dagger_{\mathbf{k}s}(0)\, e^{i\omega_k t}, \tag{2.16b}$$

which satisfy the usual commutation relations of a harmonic oscillator, $\left[\hat{a}_{\mathbf{k}s}(t),\, \hat{a}^\dagger_{\mathbf{k}'s'}(t)\right] = \delta_{\mathbf{k}\mathbf{k}'}\delta_{ss'}$. In the Heisenberg picture, the Hamiltonian of the quantized electromagnetic field can be written as

$$H_\mathrm{f} = \sum_{\mathbf{k},s} \hbar\omega_k \left[\hat{a}^\dagger_{\mathbf{k}s}(t)\hat{a}_{\mathbf{k}s}(t) + \frac{1}{2}\right], \tag{2.17}$$

where the term proportional to $1/2$ is the zero-point contribution. The quantized expression for the vector potential finally reads

$$\mathbf{A}(\mathbf{r},t) = \sqrt{\frac{\hbar}{2\epsilon_0\omega_k L^3}} \sum_{\mathbf{k},s} \left[\hat{a}_{\mathbf{k}s}(0)\, \mathbf{e}_{\mathbf{k}s} e^{i(\mathbf{k}\cdot\mathbf{r}-\omega_k t)} + \hat{a}^\dagger_{\mathbf{k}s}(0)\, \mathbf{e}^*_{\mathbf{k}s} e^{-i(\mathbf{k}\cdot\mathbf{r}-\omega_k t)}\right]. \tag{2.18}$$

In the following, we omit the hat for quantum mechanical operators. For the total Hamiltonian of the electron, interacting with the quantized electromagnetic field, we obtain with Eqs. (2.10), (2.17), and (2.18),

$$H = H_0 + H_\mathrm{f} + H_\mathrm{int}, \tag{2.19}$$

where

$$H_0 = \frac{\mathbf{p}^2}{2m_0} + V(\mathbf{r}), \tag{2.20}$$

$$H_\mathrm{f} = \sum_{\mathbf{k},s} \hbar\omega_k \left[\hat{a}^\dagger_{\mathbf{k}s}(t)\hat{a}_{\mathbf{k}s}(t) + \frac{1}{2}\right], \tag{2.21}$$

$$H_\mathrm{int} = -\frac{e}{m_0 c}\mathbf{A}(\mathbf{r},t)\cdot\mathbf{p} + \frac{e^2}{2m_0c^2}\mathbf{A}^2(\mathbf{r},t) - \frac{e}{m_0 c}\mathbf{S}\cdot\mathbf{B}(\mathbf{r},t). \tag{2.22}$$

In H_int, we neglect the term $\propto \mathbf{A}^2(\mathbf{r},t)$ which describes photon-photon scattering, assuming that it is small compared to the first term in Eq. (2.22) which is linear in $\mathbf{A}$. This is true for low-intensity fields and is a good approximation for most optical experiments. We now transform into the Schrödinger picture where the factors $\exp(\pm i\omega_k t)$ are removed. Defining $A_\mathbf{k} = \sqrt{\hbar/2\omega_k\epsilon_0 L^3}$, we obtain

$$\mathbf{A}(\mathbf{r})\cdot\mathbf{p} = \sum_{\mathbf{k},s} A_\mathbf{k} \left[a_{\mathbf{k}s}\, e^{i\mathbf{k}\cdot\mathbf{r}}\mathbf{e}_{\mathbf{k}s}\cdot\mathbf{p} + a^\dagger_{\mathbf{k}s}\, e^{-i\mathbf{k}\cdot\mathbf{r}}\mathbf{e}^*_{\mathbf{k}s}\cdot\mathbf{p}\right]. \tag{2.23}$$

For atoms or quantum dots[2] , the wavelength of the coupled photon mode is typically much larger than the spatial extension of the corresponding electron wave functions. In this limit, one can perform a multipole expansion $\exp(\pm i\mathbf{k}\cdot\mathbf{r}) = 1 \pm i\mathbf{k}\cdot\mathbf{r} + \ldots$ in Eq. (2.23) and truncate the series after the lowest non-vanishing term in the transition matrix elements. In the following, we discuss the first two interaction terms of the multipole expansion. The first term gives rise to electric dipole transitions, whereas the second term gives rise to magnetic dipole and electric quadrupole transitions.

2.4.1 Electric dipole transitions

Most optical transitions are electric dipole transitions [95], which are described by Eq. (2.22) (with the term $\propto \mathbf{A}^2$ neglected) in the electric dipole approximation, $\exp(\pm i\mathbf{k}\cdot\mathbf{r}) \approx 1$. The dipole approximation is exact for a point-like emitter, where $r = 0$ and the spatial variation of the electromagnetic field is not important for the interaction. Further, the term $e\mathbf{S}\cdot\mathbf{B}(\mathbf{r},t)/m_0c$ in Eq. (2.22) can safely be neglected in the dipole approximation because its transition matrix elements are smaller by a factor $kr\,(\ll 1)$ than the transition matrix elements of $\mathbf{A}\cdot\mathbf{p}$ [95]. Eq. (2.22) then simplifies to

$$H_{\rm int} = -\frac{e}{m_0 c}\sum_{\mathbf{k},s} A_{\mathbf{k}}\left[a_{\mathbf{k}s}\,\mathbf{e}_{\mathbf{k}s}\cdot\mathbf{p} + a^\dagger_{\mathbf{k}s}\,\mathbf{e}^*_{\mathbf{k}s}\cdot\mathbf{p}\right]. \tag{2.24}$$

In the following we consider coupling of the states $|2\rangle$ and $|1\rangle$ with one single photon mode and drop the summation over $\mathbf{k}$ and s. In the basis of the states $|1\rangle$ and $|2\rangle$ we obtain

$$\begin{aligned} H_{\rm int} \;=\; & -\frac{e}{m_0 c}A_{\mathbf{k}}\Big[a_{\mathbf{k}s}\left(|2\rangle\langle 1|\langle 2|\mathbf{e}_{\mathbf{k}s}\cdot\mathbf{p}|1\rangle + |1\rangle\langle 2|\langle 1|\mathbf{e}_{\mathbf{k}s}\cdot\mathbf{p}|2\rangle\right) \\ & + a^\dagger_{\mathbf{k}s}\left(|2\rangle\langle 1|\langle 2|\mathbf{e}^*_{\mathbf{k}s}\cdot\mathbf{p}|1\rangle + |1\rangle\langle 2|\langle 1|\mathbf{e}^*_{\mathbf{k}s}\cdot\mathbf{p}|2\rangle\right)\Big]. \end{aligned} \tag{2.25}$$

The momentum matrix elements in the above expression, $\langle 2|\mathbf{e}_{\mathbf{k}s}\cdot\mathbf{p}|1\rangle$, etc., are non-zero only if the states $|1\rangle$ and $|2\rangle$ satisfy certain symmetry criteria, which are called selection rules. First of all, for a non-zero momentum matrix element the states $|1\rangle$ and $|2\rangle$ must have different parity. For the orbital angular momentum eigenstates $|l,m\rangle$ and $|l',m'\rangle$, respectively, the so-called electric dipole transition selection rules $l - l' = \pm 1$ and $m - m' = 0, \pm 1$ must be satisfied [95]. $|1\rangle$ and $|2\rangle$ must also have the same spin state. In the presence of spin-orbit coupling $H_{\rm so} = \lambda\mathbf{L}\cdot\mathbf{S}$ the angular momentum eigenstates are classified according to the total angular momentum $\mathbf{J} = \mathbf{L}+\mathbf{S}$ with eigenstates $|j,m_j\rangle$. The dipole selection rules then transform into $j - j' = 0, \pm 1$, $l - l' = \pm 1$, and $m_j - m_{j'} = 0, \pm 1$. Note that a $j - j' = 0$ transition is only allowed for $j,\, j' \neq 0$ [95].

[2]For InAs or GaAs quantum dots, e.g., the energetically lowest optical transitions are typically in the near infrared (with photon wave number $k \sim 1\,\mu\mathrm{m}^{-1}$) and r is on the order of the quantum dot size (at most a few tens of nanometers). Thus, $kr \approx 10^{-2}$.

The coupling strength is characterized by the (optical) Rabi frequency

$$\hbar\Omega_{\mathbf{k}s} = -\frac{e}{m_0 c} A_{\mathbf{k}} \langle 2|\mathbf{e}_{\mathbf{k}s} \cdot \mathbf{p}|1\rangle = -\frac{e}{m_0 c}\sqrt{\frac{\hbar}{2V\epsilon_0\omega_k}}\,\langle 2|\mathbf{e}_{\mathbf{k}s} \cdot \mathbf{p}|1\rangle. \tag{2.26}$$

We exclude transitions to other levels (which are in principle possible in real atoms). Note that the Hamiltonian Eq. (2.25) contains energy non-conserving terms, namely, the emission of a photon combined with an excitation of the emitter and the Hermitian conjugate expression of this process. However, these terms vanish due to angular momentum selection rules if we consider coupling with a circularly polarized mode (cf. Ref. [32], pp.752). For the coupling with a mode of arbitrary polarization, the rotating wave approximation is usually applied, i.e., only the energy-conserving interaction terms in Eq. (2.25) are kept. This is usually a good approximation when the mode and the emitter are resonant, $\omega_k = |E_2 - E_1|/\hbar$, or quasi-resonant, $\omega_k \approx |E_2 - E_1|/\hbar$, where $H_0|i\rangle = E_i|i\rangle$ for $i = 1, 2$. For a circularly polarized mode, or alternatively, for a mode with non-circular polarization in the rotating wave approximation, we thus obtain the standard interaction Hamiltonian for electric dipole transitions,

$$H_{\text{int}} = -\frac{e}{m_0 c} A_{\mathbf{k}} \left(a_{\mathbf{k}s}\,|2\rangle\langle 1|\langle 2|\mathbf{e}_{\mathbf{k}s} \cdot \mathbf{p}|1\rangle + a^\dagger_{\mathbf{k}s}\,|1\rangle\langle 2|\langle 1|\mathbf{e}^*_{\mathbf{k}s} \cdot \mathbf{p}|2\rangle \right). \tag{2.27}$$

With this interaction Hamiltonian, $H = H_0 + H_{\text{f}} + H_{\text{int}}$ is the well-known Jaynes-Cummings Hamiltonian [96] which has successfully been applied to describe the interaction of atoms and photons in a cavity [97].

Further, if the two-level system is coupled to a laser field, Eq. (2.27) can be simplified by assuming that the laser field is in a coherent state, described by $|\alpha\rangle = \exp\left(\alpha a_L^\dagger - \alpha^* a_L\right)|0\rangle$, where $\alpha \in \mathbb{C}$, $a_L^{(\dagger)}$ are photon operators of the laser mode, and $|0\rangle$ is the photon vacuum. Since coherent states are eigenstates of the annihilation operator, $a_L|\alpha\rangle = \alpha|\alpha\rangle$, the matrix elements of H_{int} can readily be calculated in the laser field subspace. For the coherent state $|\alpha\rangle$ the mean number of photons in the mode is given by $|\alpha|^2$. Thus, the well-known semi-classical expression for the coupling of a two-level system with a classical field is recovered from the fully quantum mechanical expression when a coherent state is taken into account [32].

In the dipole approximation the coupling term $\mathbf{A}\cdot\mathbf{p}$ can be transformed into a coupling of the form $\mathbf{d} \cdot \mathbf{E}$, where $\mathbf{d} = e\mathbf{r}$ is the electric dipole moment operator and $\mathbf{E}$ the electric field. This can be readily understood from the relation [98]

$$\langle 2|\mathbf{p}|1\rangle \;=\; \frac{im_0}{\hbar}\langle 2|[H_0, \mathbf{r}]|1\rangle = \frac{im_0}{\hbar}(E_2 - E_1)\langle 2|\mathbf{r}|1\rangle, \tag{2.28}$$

where we used $[\mathbf{r}, H_0] = i\hbar\mathbf{p}/m_0$. Further, for $(E_2 - E_1)/\hbar = \omega_k$ we can use the definition $\mathbf{E} = -(1/c)(\partial/\partial t)\mathbf{A}$ for the electric field to obtain the desired expression of the form $\mathbf{d} \cdot \mathbf{E}$.

2.4.2 Magnetic dipole and electric quadrupole transitions

The second term in the multipole expansion ($\propto \mathbf{k}\cdot\mathbf{r}$) leads to momentum matrix elements of the form $\langle i|(\mathbf{k}\cdot\mathbf{r})(\mathbf{e}_{\mathbf{k}s}\cdot\mathbf{p})|j\rangle$ in H_{int}. We add to this term the interaction $\propto \mathbf{S}\cdot\mathbf{B}$ of the spin with the magnetic field. The resulting interaction term can be represented as the sum of a magnetic dipole term and an electric quadrupole term [95]. The magnetic dipole term describes the coupling of the total magnetic moment to the magnetic field. For transitions between angular momentum eigenstates $|l, m_l, m_s\rangle$ and $|l', m_{l'}, m_{s'}\rangle$ with orbital and spin magnetic moment m_l and m_s, respectively, the selection rules for magnetic dipole transitions are $l - l' = 0$, $m_l - m_{l'} = 0 \pm 1$, and $m_s - m_{s'} = 0, \pm 1$. In the presence of spin-orbit interaction (defined as in Section 2.4.1), the magnetic dipole selection rules transform into $l - l' = 0$, $j - j' = 0, \pm 1$, and $m_j - m_{j'} = 0, \pm 1$. The selection rules for electric quadrupole transitions are given by $l - l' = 0, \pm 2$ and $m_l - m_{l'} = 0, \pm 1, \pm 2$. The electric quadrupole transition can be interpreted as the interaction of the electric quadrupole moment with the gradient of the electric field [95]. It is usually experimentally possible to place the emitter at a location, e.g., inside a cavity, where the magnetic field is large and the gradient of the electric field is negligible, enabling the excitation of only a magnetic dipole transition. A typical example for magnetic dipole transitions are magnetic resonance transitions, like electron spin resonance which we consider in Chapter 4.

2.4.3 Band structure of III-V semiconductors

In the following, we mainly focus on quantum dots made of III-V semiconductor compounds with zincblende structure [99], e.g., GaAs or InAs. Additionally, the zincblende structure (with an additional anisotropy) can be assumed to a good approximation for small II-VI quantum dots with hexagonal crystal structure (e.g., CdSe), as discussed in Chapter 5.

The electronic bandstructure of a three-dimensional semiconductor with zincblende structure is illustrated in Figure 2.4 (a). The bands are parabolic close to their extrema which are all located at the Γ point, i.e., the center of the Wigner-Seitz cell. The conduction (c) band Bloch states have orbital s symmetry and are spin-degenerate. The valence (v) band consists of three twofold degenerate subbands, the heavy-hole (hh), the light-hole (lh), and the spin-orbit split-off (so) band. The v-band Bloch states have orbital p symmetry. The bottom of the c band and the top of the v band are split by the band-gap energy E_{gap}. Provided the spin-orbit interaction is nearly isotropic ($H_{\text{so}} \approx \lambda \mathbf{L}\cdot\mathbf{S}$, where $\mathbf{L}$ is the orbital angular momentum and $\mathbf{S}$ the spin operator of the electron), the total angular momentum $\mathbf{J}^2 = (\mathbf{L}+\mathbf{S})^2$ provides (to a good approximation) a good quantum number j in semiconductors. The valence-band states with different j ($j = 1/2$ for the so band, $j = 3/2$ for the hh and lh band) are then split by Δ_{so} in energy due to the spin-orbit interaction. The corresponding spinor representations are usually called Γ_8 for the hh and the lh

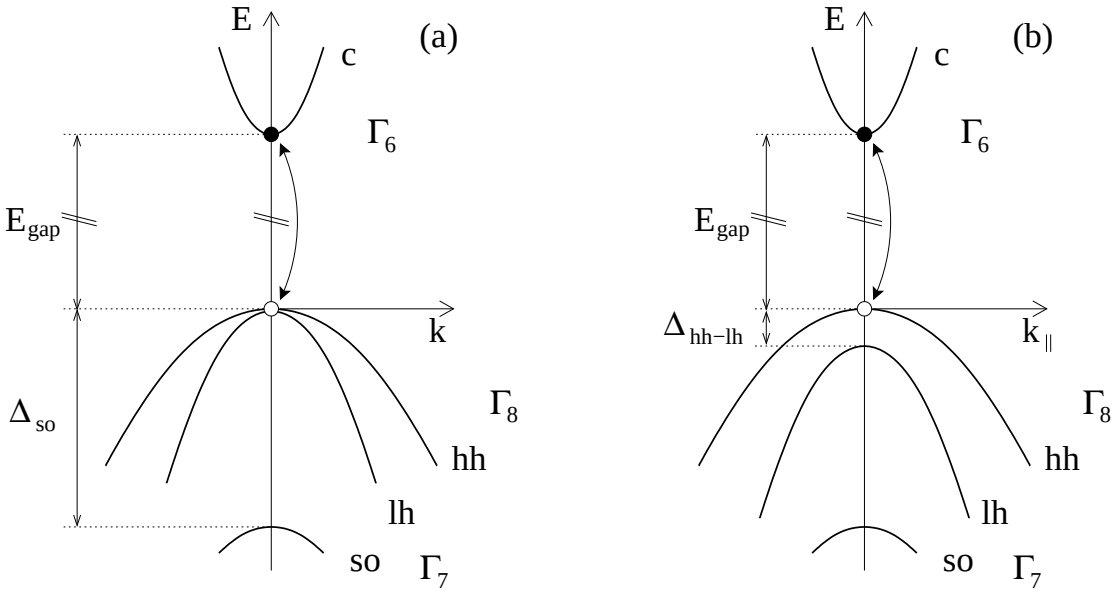

Figure 2.4: Electronic bandstructure (schematically) in the vicinity of the Γ point for (a) a three-dimensional crystal (b) an effectively two-dimensional structure (a quantum well) with zincblende lattice structure. The bands are shown as a function of (a) the wavevector k (b) the in-plane wavevector $k_{\|}$ and are the conduction (c) band, the heavy-hole (hh) band, the light-hole (lh) band, and the spin-orbit split-off (so) band. The spinor representation of the c band is Γ_6, whereas the hh and the lh band have spinor representation Γ_8, and the spinor representation of the so band is Γ_7 [99, 100]. In (b), the hh and the lh bands are split by $\Delta_{\mathrm{hh-lh}}$ due to the uniaxial confinement, as explained in the text. The black and white circles represent electrons and holes, respectively.

band, Γ_7 for the *so* band, and Γ_6 for the *c* band [99, 100]. The *hh* and *lh* subbands are degenerate at the Γ point, see Figure 2.4 (a). The *hh* states have the angular momentum projections $J_z = \pm 3/2$ and the *lh* states $J_z = \pm 1/2$. For finite electron wavevectors $k \neq 0$, the *hh* and *lh* subbands split into two branches, according to the different curvatures of the energy dispersion, which implies different effective masses of heavy and light holes. Further away from the extrema, strong inter-band mixing usually occurs (especially between *hh* and *lh*) and leads to non-parabolic bands.

Quantum confinement along one crystal axis (as in a quantum well), e.g., z, quantizes the momentum component p_z. Consequently, the *hh* and *lh* states of the lowest subband are split by an energy $\Delta_{\mathrm{hh-lh}}$ at the Γ point (because of their different effective masses[3]), as illustrated in Figure 2.4 (b). Such a confinement asymmetry also defines a spin quantization axis for the *v*-band states along z. Typically, $\Delta_{\mathrm{hh-lh}} \sim 10\,\mathrm{meV}$ for a quantum well of thickness $\sim 10\,\mathrm{nm}$ [101]. Uniaxial strain in the semiconductor crystal is another mechanism that lifts the degeneracy of heavy and light holes [99] and can thus define the spin quantization axis. Typically, the energetically lowest interband transitions between the *c* and *v* band in quantum wells are transitions including the *hh* subband, as depicted in Figure 2.4 (b).

Via photon absorption, an electron in a valence-band state (e.g., the *hh* subband) can be excited to a *c*-band state, as shown schematically in Figure 2.4. Such interband transitions are determined by optical selection rules (see Section 2.4.1), which establish conditions on the quantum numbers of the optically coupled states. Due to optical selection rules, the *c*-*hh* transitions between the band extrema are circularly polarized, and there are both circularly and linearly polarized *c*-*lh* and *c*-*so* transitions [99]. Photons with circular polarization $\sigma^{\pm}$ carry an angular momentum with projection ± 1 (in units of $\hbar$) along their propagation direction. Consequently, there is a one-to-one correspondence between circular photon polarization and electron spin for optical excitations of *hh* states.

The electron-hole pair created with an inter-band transition is called an exciton. The electron and hole of an exciton form a bound state due to the Coulomb interaction, similar to that of a hydrogen atom (or rather positronium, depending on the ratio of the effective masses for the electron and the hole). Several excitons can form bound complexes. We refer to the system of two bound excitons as a biexciton. Another type of exciton which is important in the following is the charged exciton: Excitons may bind an extra charge carrier (an electron or a hole), leading to a negatively or a positively charged exciton, respectively.

2.4.4 Optical properties of quantum dots

Due to the usually strong confinement along one direction in semiconductor quantum dots, say z, it is often useful to start with the band structure of a quantum well [shown

[3] The *hh* and *lh* energies for $k_{\parallel} = 0$ are $\langle p_z^2 \rangle / 2m_{hh}$ and $\langle p_z^2 \rangle / 2m_{lh}$, respectively.

in Figure 2.4 (b)] and introduce an additional weak confinement in the plane. By only taking the lowest subband of the quantum well into account we obtain quasi two-dimensional quantum dots. For circular confinement in the xy plane, the z component J_z of $\mathbf{J}$ is a good quantum number. Then, the confined valence band states have pure hh or lh character since they can be classified according to $\mathbf{J}^2$ and J_z. The one-to-one correspondence of electron spin and circular photon polarization (as for a quantum well, see Section 2.4.3) is then preserved for the ground-state transitions since they are related to hh excitons. Taking advantage of this property for the readout of spin states, light-emitting diodes ("spin-LEDs") have been fabricated using quantum wells [83, 84] or quantum dots [85, 87, 88] as the optically active medium, where the polarization of the emitted photons indicates the spin polarization of the electrons (or holes) injected into the spin-LED.

In contrast, an anisotropic quantum dot confinement in the plane induces mixing of angular momentum eigenstates, which weakens the one-to-one correspondence of spin and photon polarizations. Yet, we will mostly discuss quantum dots with a pure hh ground state in the following, motivated by the published results of many experiments. We therefore assume a symmetric parabolic in-plane confinement for the low-energy physics with few carriers in the dot. We will discuss the effect of an anisotropic dot shape or hh-lh mixing directly in the corresponding chapters.

For excitons in quantum dots one can distinguish between different confinement regimes. In the strong-confinement regime, the single-particle confinement energies due to the quantum dot potential are much larger than the electron-hole Coulomb interaction energy. An alternative definition of the strong-confinement regime is obtained in the limit where the quantum dot radius is much smaller than the Bohr radius a_X of a free exciton. Small colloidal semiconductor quantum dots, which we consider in Chapter 5, or small self-assembled quantum dots are examples for dots in the strong confinement regime. In this situation one can use non-interacting wavefunctions for electrons and holes and take the Coulomb interaction into account in the frame of perturbation theory.

2.5 Optical transitions in quantum dots

We turn to a microscopic description of the optical recombination processes of the two electrons which occur independently, except for the entanglement of the spin wave functions. We consider now one single branch $\alpha = L, R$ of the apparatus and omit the index α. The state of the single quantum dot which is charged with two heavy holes (hh's) in the orbital ground state and into which a single electron with spin σ has been injected is given by

$$|e, \sigma\rangle = \int \mathrm{d}^3 r_c \phi_c^*(\mathbf{r}_c, \sigma) b_{c\sigma}^\dagger |\chi\rangle. \tag{2.29}$$

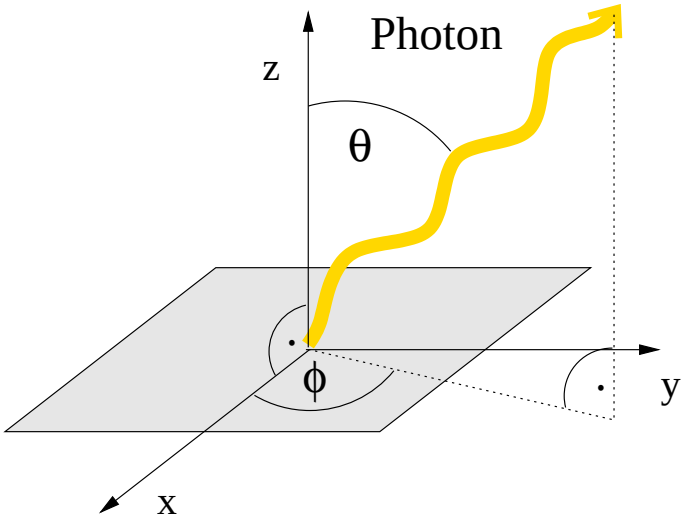

Figure 2.5: Definition of the photon emission angles θ and ϕ. The axes x, y, and z are along the cubic crystal axes [100], [010], and [001], respectively. The spin quantization axis is defined along z.

Here, $b^\dagger_{n\sigma}$ creates an electron with spin $S_z = \sigma/2 = \pm 1/2$ in the state n of the dot, $|\chi\rangle = \sum_{\tau\neq\tau'} \int \mathrm{d}^3 r_{v1} \mathrm{d}^3 r_{v2} \phi_v(\mathbf{r}_{v1}, \tau; \mathbf{r}_{v2}, \tau') b_{v\tau} b_{v\tau'} |g\rangle$, where $|g\rangle$ is the electrostatically neutral ground state of the quantum dot, and $\phi_v(\mathbf{r}_{v1}, \tau; \mathbf{r}_{v2}, \tau')$ is the orbital part of the two-hole wave function. In the strong-confinement regime where Coulomb correlations are negligible, ϕ_v is a product of the single-particle valence-band states. The labels τ, τ' denote the hh spin component $S_z = \tau/2 = \pm 1/2$ that factor out for angular momentum $J_z = \pm 3/2$.

We now calculate the emission matrix element (see Section 2.4.1),

$$\langle f|H_{\mathrm{em}}|i\rangle = -\frac{e}{m_0 c} A_{\mathbf{k}} \langle f| a^\dagger_{\mathbf{k}\lambda} \mathbf{e}^*_{\mathbf{k}\lambda} \cdot \mathbf{p}^*_{cv} |i\rangle, \tag{2.30}$$

for the electric dipole transition with initial state $|i\rangle = |e,\sigma\rangle \otimes |\ldots, n_{\mathbf{k}\lambda}, \ldots\rangle$ and final state $|f\rangle = b_{v\tau'}|g\rangle \otimes |\ldots, n_{\mathbf{k}\lambda}+1, \ldots\rangle$, where $|\ldots, n_{\mathbf{k}\lambda}, \ldots\rangle$ is a Fock state of the electromagnetic field, typically the photon vacuum. Because of quantum mechanical selection rules, the optical transitions connect only states with the same spin such that $\tau = \sigma$ and $\tau' \neq \sigma$. We apply the envelope-function approximation for the single-particle levels and write $\phi_n(\mathbf{r}_n, \sigma) = \psi_n(\mathbf{r}_n) u_{n\sigma}(\mathbf{r}_n)$, where $u_{n\sigma}(\mathbf{r}_n)$ is a Bloch function and $\psi_n(\mathbf{r}_n)$ an envelope function determined by $V_{\mathrm{qd}}(\mathbf{r})$, where $n = c, v_1, v_2$. The orbital part of the c-band Bloch wave function is an s-type function $|s\rangle$, whereas the hh band has a p-type function $|x + i\tau y\rangle$. We obtain

$$|\langle f|H_{\mathrm{em}}|i\rangle| = \frac{e}{m_0 c} A_{\mathbf{k}} \sqrt{n_{\mathbf{k}\lambda}+1}\ |\mathbf{e}^*_{\mathbf{k}\lambda} \cdot \mathbf{p}^*_{cv} C_{eh}|\,, \tag{2.31}$$

where $\mathbf{p}^*_{cv} = \mathbf{p}_{vc} = \langle u_{v\sigma}|\mathbf{p}|u_{c\sigma}\rangle$ is the inter-band momentum matrix element, $\mathbf{e}_{\mathbf{k}\lambda} = (\cos\theta\cos\phi - i\lambda\sin\phi,\ \cos\theta\sin\phi + i\lambda\cos\phi,\ -\sin\theta)/\sqrt{2}$ is the unit polarization vector

for a photon with $\lambda = \pm 1$ for circular polarization $|\sigma^{\pm}\rangle$, and $C_{eh} = \int \mathrm{d}^3 r\, \psi_c^*(\mathbf{r},\sigma)\psi_v(\mathbf{r},\sigma)$. The photon is emitted into a direction given by the polar angle θ and the azimuthal angle ϕ, see Figure 2.5. For cubic symmetry, $\mathbf{e}_{\mathbf{k}\lambda}^* \cdot \mathbf{p}_{cv}^* = p_{cv}(\cos\theta - \sigma\lambda)e^{-i\sigma\phi}/2 \equiv p_{cv} m_{\sigma\lambda}(\theta,\phi)$, where $p_{cv} = \langle s|p_x|x\rangle$. With the transition $|e,\sigma\rangle \rightarrow b_{v-\sigma}|g\rangle$, a photon in the state

$$|\sigma,\theta,\phi\rangle = N(\theta)(m_{\sigma,+1}(\theta,\phi)|\sigma^+\rangle + m_{\sigma,-1}(\theta,\phi)|\sigma^-\rangle) \tag{2.32}$$

is emitted into the direction (θ,ϕ). Here, $N(\theta) = [2/(1+\cos^2\theta)]^{1/2}$ is a normalization factor. Eq. (2.32) shows that for $\theta = 0$, a spin up ($\sigma = +1$) electron generates a $|\sigma^-\rangle$ photon, whereas a $|\sigma^+\rangle$ photon is obtained from a spin down ($\sigma = -1$) electron which ensures a one-to-one correspondence between spin and photon polarization. The admixture of the opposite circular polarization increases with θ, leading to elliptical polarization for $\theta \in (0,\pi/2)$ and linear polarization for $\theta = \pi/2$. For $\theta \neq 0$, the spin-inverted states $|+1,\theta,\phi\rangle$ and $|-1,\theta,\phi\rangle$ have interchanged coefficients for $|\sigma^+\rangle$ and $|\sigma^-\rangle$, up to a relative phase which is determined by the global phase factors $\exp(-i\sigma\phi)$ of the single-photon states. Note that in two-photon states the azimuthal angles thus provide a *relative* phase which we exploit in Section 2.9.

2.6 Entangled four-photon state

Due to the antisymmetric hole ground state, the two photons produced at recombination are entangled with the two holes which remain in the dots. For injection of an electron singlet and subsequent photon emission along z, this state is proportional to

$$|\sigma^+\rangle_L|\sigma^-\rangle_R|-3/2\rangle_L|+3/2\rangle_R - |\sigma^-\rangle_L|\sigma^+\rangle_R|+3/2\rangle_L|-3/2\rangle_R. \tag{2.33}$$

The corresponding expressions for the other Bell states are obtained analogously. If only the two photons in Eq. (2.33) are measured, an incomplete test of the state is performed [102]. No photon correlations due to entanglement can then be measured because of the orthogonal two-hole wave functions. Similarly, no additional holes should be injected into the dots at this point. When the system is in the state Eq. (2.33) and a hole is injected resonantly into one of the dots, the photons are projected into a completely mixed state. For non-resonant injection with subsequent orbital relaxation of the hole, the projection into a mixed photon state occurs on a time scale given by the heavy-hole singlet-triplet decoherence time.

Instead, by injecting a pair of electrons with spins polarized in the xy plane into the dots, a four-photon state of GHZ type can be produced if the T_2-time of the exciton polarization exceeds well the exciton lifetime. For circularly polarized photons emitted along z, the electron Bell states give rise to the states

$$|\Psi^{\pm}\rangle \rightarrow |\sigma^+\sigma^-\sigma^-\sigma^+\rangle \pm |\sigma^-\sigma^+\sigma^+\sigma^-\rangle, \tag{2.34}$$

$$|\Phi^{\pm}\rangle \rightarrow |\sigma^-\sigma^-\sigma^+\sigma^+\rangle \pm |\sigma^+\sigma^+\sigma^-\sigma^-\rangle, \tag{2.35}$$

where the first two entries indicate the first photon pair (L,R) and the third and fourth entry the second photon pair (L,R), respectively. Normalization has been omitted for simplicity. In order to preserve the entanglement in Eq. (2.33), the two electrons with in-plane polarization need to be injected within the hole-spin coherence time after emission of the first photon pair. Yet, the second photon pair is generated by neutral excitons which in asymmetric quantum dots are subject to a significant fine structure splitting, the consequences of which we discuss in Section 2.7.

To switch between the production of entangled and in-plane polarized electron pairs, a double quantum dot can be used with a tunable exchange splitting J and to which an in-plane magnetic field $B_\perp$ is applied [73, 74]. If J is larger than the electron Zeeman energy, the two-electron ground state is a singlet and entangled electrons can be extracted. In contrast, if J is tuned to a value smaller than the electron Zeeman energy, the ground state is a triplet with spins aligned along $B_\perp$. The exchange splitting J can be reduced by applying an electric gate voltage such that the two electrons are pushed apart from each other. See Chapter 3 for a more detailed discussion of double dots. Alternatively, for subsequent injection of *two* entangled electron pairs, $\pm \rightarrow +$ on the right-hand side of Eqs. (2.34) and (2.35). We discuss in the following two sections the criteria which need to be satisfied in experiments to produce the GHZ states Eqs. (2.34) and (2.35).

2.7 Electron-hole exchange interaction

The inter-band Coulomb exchange interaction, which is usually referred to as the electron-hole exchange interaction, leads to a fine structure splitting of excitonic levels. This mechanism has been identified to be responsible for the recent observation that photon pairs produced at the recombination cascade of biexcitons in quantum dots are not entangled [65, 66, 67, 68, 69], in contradiction with theoretical expectations [63, 64]. We review the electron-hole exchange interaction here and discuss its consequences to our scheme.

According to the method of invariants, the exchange splitting of the ground state of a confined exciton with symmetry $\Gamma_6 \times \Gamma_8$ (see Section 2.4.3) can be written as an effective coupling of the electron spin $\mathbf{S}$ and the hole angular momentum $\mathbf{J}$ [100, 103],

$$H_{\rm exc} = -\sum_{i=x,y,z} \left(a_i J_i^h S_i^e + b_i (J_i^h)^3 S_i^e \right). \tag{2.36}$$

Here, a_i, b_i are coupling constants, and the $j = 3/2$ angular momentum operators for the valence-band holes can be represented in the basis $|3/2\rangle$, $|1/2\rangle$, $|-1/2\rangle$, $|-3/2\rangle$,

by

$$J_x^h = \begin{pmatrix} 0 & \sqrt{3}/2 & 0 & 0 \\ \sqrt{3}/2 & 0 & 1 & 0 \\ 0 & 1 & 0 & \sqrt{3}/2 \\ 0 & 0 & \sqrt{3}/2 & 0 \end{pmatrix}, \tag{2.37a}$$

$$J_y^h = \begin{pmatrix} 0 & -i\sqrt{3}/2 & 0 & 0 \\ i\sqrt{3}/2 & 0 & -i & 0 \\ 0 & i & 0 & -i\sqrt{3}/2 \\ 0 & 0 & i\sqrt{3}/2 & 0 \end{pmatrix}, \tag{2.37b}$$

$$J_z^h = \begin{pmatrix} 3/2 & 0 & 0 & 0 \\ 0 & 1/2 & 0 & 0 \\ 0 & 0 & -1/2 & 0 \\ 0 & 0 & 0 & -3/2 \end{pmatrix}. \tag{2.37c}$$

The corresponding cubed matrices are obtained as

$$(J_x^h)^3 = \begin{pmatrix} 0 & 7\sqrt{3}/8 & 0 & 3/4 \\ 7\sqrt{3}/8 & 0 & 5/2 & 0 \\ 0 & 5/2 & 0 & 7\sqrt{3}/8 \\ 3/4 & 0 & 7\sqrt{3}/8 & 0 \end{pmatrix}, \tag{2.38a}$$

$$(J_y^h)^3 = \begin{pmatrix} 0 & -i7\sqrt{3}/8 & 0 & i3/4 \\ i7\sqrt{3}/8 & 0 & -i5/2 & 0 \\ 0 & i5/2 & 0 & -i7\sqrt{3}/8 \\ -i3/4 & 0 & i7\sqrt{3}/8 & 0 \end{pmatrix}, \tag{2.38b}$$

$$(J_z^h)^3 = \begin{pmatrix} 27/8 & 0 & 0 & 0 \\ 0 & 1/8 & 0 & 0 \\ 0 & 0 & -1/8 & 0 \\ 0 & 0 & 0 & -27/8 \end{pmatrix}. \tag{2.38c}$$

In terms of the exciton states $|J_z^h, S_z^e\rangle$, Eq. (2.36) can be represented in the basis $|\frac{3}{2}, -\frac{1}{2}\rangle$, $|-\frac{3}{2}, \frac{1}{2}\rangle$, $|\frac{3}{2}, \frac{1}{2}\rangle$, $|-\frac{3}{2}, -\frac{1}{2}\rangle$, $|\frac{1}{2}, \frac{1}{2}\rangle$, $|-\frac{1}{2}, -\frac{1}{2}\rangle$, $|\frac{1}{2}, -\frac{1}{2}\rangle$, $|-\frac{1}{2}, \frac{1}{2}\rangle$ as

$$H_{\text{exc}} \doteq \begin{pmatrix} A_{\text{hh}} & A_{\text{hh-lh}} \\ A_{\text{hh-lh}}^* & A_{\text{lh}} \end{pmatrix}, \tag{2.39}$$

where A_{hh}, A_{lh}, and $A_{\text{hh-lh}}$ are 4×4 block matrices. Explicitly,

$$A_{\text{hh}} = \begin{pmatrix} \Delta_0 & \Delta_1 & 0 & 0 \\ \Delta_1 & \Delta_0 & 0 & 0 \\ 0 & 0 & -\Delta_0 & \Delta_2 \\ 0 & 0 & \Delta_2 & -\Delta_0 \end{pmatrix} \tag{2.40}$$

couples hh exciton states, and $\Delta_0 = (3/4)a_z + (27/16)b_z$, $\Delta_1 = -(3/8)(b_x - b_y)$, and $\Delta_2 = -(3/8)(b_x + b_y)$. The block matrix

$$A_{\mathrm{hh-lh}} = \begin{pmatrix} \Delta_3 & 0 & 0 & 0 \\ 0 & \Delta_3 & 0 & 0 \\ 0 & 0 & \Delta_4 & 0 \\ 0 & 0 & 0 & \Delta_4 \end{pmatrix} \tag{2.41}$$

mixes hh and lh excitons with $\Delta_3 = -(\sqrt{3}/4)(a_x + a_y) - (7\sqrt{3}/16)(b_x + b_y)$ and $\Delta_4 = -(\sqrt{3}/4)(a_x - a_y) - (7\sqrt{3}/16)(b_x - b_y)$, and

$$A_{\mathrm{lh}} = \begin{pmatrix} -\Delta_5 & \Delta_6 & 0 & 0 \\ \Delta_6 & -\Delta_5 & 0 & 0 \\ 0 & 0 & \Delta_5 & \Delta_7 \\ 0 & 0 & \Delta_7 & \Delta_5 \end{pmatrix} \tag{2.42}$$

couples lh exciton states, where $\Delta_5 = (1/4)a_z + (1/16)b_z$, $\Delta_6 = -(1/2)(a_x - a_y) - (5/4)(b_x - b_y)$, and $\Delta_7 = -(1/2)(a_x + a_y) - (5/4)(b_x + b_y)$.

The electron-hole exchange interaction splits bright and dark hh-exciton states by $2\Delta_0$, whereas the splitting between dark and bright lh states amounts to $2\Delta_5$. For cubic crystal symmetry (which is given for a $\Gamma_6 \times \Gamma_8$ exciton) and rotational symmetry of the dot, $a_x = a_y$ and $b_x = b_y$. In this case H_{exc} is diagonal for the bright excitons ($\Delta_1 = \Delta_6 = 0$), in contrast to the dark excitons which are mixed due to Δ_2 and Δ_7. In quasi two-dimensional systems, the electron-hole exchange interaction can further be simplified because of the splitting $\Delta_{\mathrm{hh-lh}}$ of heavy and light holes [103, 104]. In quantum dots, typically $\Delta_{\mathrm{hh-lh}} \sim 10\,\mathrm{meV}$, being much larger than typical electron-hole exchange interaction energies ($\lesssim 0.05\,\mathrm{meV}$ in "natural" GaAs dots [42], $\lesssim 0.2\,\mathrm{meV}$ in InAs dots [104, 105, 106], $\lesssim 0.3\,\mathrm{meV}$ in CdSe/ZnSe dots [107]). We may therefore restrict ourselves to hh states and the exchange interaction described by Eq. (2.40). For a quantum dot with an asymmetric shape in the xy plane, $b_x \neq b_y$ is possible, leading to a coupling of $|\frac{3}{2}, -\frac{1}{2}\rangle$ and $|-\frac{3}{2}, \frac{1}{2}\rangle$. The new bright exciton eigenstates are the linearly polarized exciton states $(|\frac{3}{2}, -\frac{1}{2}\rangle \pm |-\frac{3}{2}, \frac{1}{2}\rangle)/\sqrt{2}$ which are split by the energy $\delta_{\mathrm{ehx}} = 2\Delta_1$. For elliptic dots these intrinsic basis states are oriented along the major and the minor axis, respectively [108].

The third and the fourth photon of the GHZ states Eqs. (2.34) and (2.35) are emitted from single excitons. For $b_x \neq b_y$ these excitons are subject to a fine structure splitting. It has been pointed out that if δ_{ehx} is larger than the exciton linewidth (which is typically only a few μeV [109]), then a polarization-entangled photon state is also entangled in energy [110], and entanglement is already destroyed after an energy measurement. Further, it is essential for the GHZ states that the photons are emitted from a coherent superposition of exciton polarization states (the same condition applies to the second photon of the biexciton cascade). For such a coherent superposition of exciton spins, the decoherence rate is, e.g., in the frame

of a generalized master equation in the Lindblad form (see Section 4.2.2) given by $1/T_{2,X} = 1/2T_{1,X} + 1/T_{\varphi,X}$, where $T_{1,X}$ is the exciton polarization relaxation time and $T_{\varphi,X}$ is the pure decoherence time. In several experiments [111, 66, 112], exciton spin relaxation times on the order of the exciton lifetime have been reported[4]. It can therefore be expected that with such quantum dots the entanglement of the GHZ states would in most cases be lost. Here, it is important to note that for $\delta_{\mathrm{ehx}} = 0$ the exciton spin relaxation via acoustic phonon processes [113] is suppressed since the phonon density of states is proportional to the phonon frequency squared, leading to a maximization $T_{2,X} \to T_{\varphi,X}$ of the exciton spin decoherence time. It is therefore desirable to compensate the exciton fine structure splitting δ_{ehx}.

To achieve $\delta_{\mathrm{ehx}} = 0$ one could in principle modify the quantum dot potential electrostatically such that $b_x = b_y$ (as for circular dots with cubic crystal symmetry). Another possibility would be to have an extra charge carrier present in the dot. For example, with an additional electron, a negatively charged exciton X^- is formed. In the ground state of an X^-, the two electrons form a spin singlet. It is therefore expected from H_{exc} [Eq. (2.36)] that the fine structure splitting vanishes, which has also been demonstrated experimentally [104, 105, 106]. We discuss in Section 2.8 that this is also true for a positively charged exciton, where an additional hole is bound to the exciton. We thus expect an increased polarization coherence of the first photon pair compared to a transition with neutral excitons. Another way to enhance the polarization coherence of the photons is to reduce the exciton lifetime to a value much smaller than $T_{2,X}$. This could be achieved if the quantum dots are located inside a cavity which couples to the exciton transition, since the exciton lifetime is then reduced due to the Purcell effect. Further, for δ_{ehx} larger than the exciton linewidth and if both exciton lines couple to the same cavity mode, also the photon energy entanglement can be erased [110].

2.8 Fine structure of X^+

We show that the electron-hole exchange interaction of an exciton in a quantum dot can be compensated by adding an extra hole. From this and the results of the previous section, a regime can be identified in which creation of four photons in the GHZ states Eqs. (2.34) and (2.35) can be expected for the scheme discussed in Section 2.6.

Recent experiments have demonstrated the controlled creation of positively charged excitons (X^+) in quantum dots [114, 115]. In contrast to the two electrons of an X^-, the antisymmetric two-hole ground state of an X^+ is not an isotropic singlet because the holes have total angular momentum $j = 3/2$ rather than just spin 1/2. For an X^+ in a quantum dot in the strong-confiment regime, $\left\langle J_z^{h1} + J_z^{h2} \right\rangle = 0$ for

[4] Still, experiments with different types of quantum dots showed much longer exciton polarization relaxation times [120, 121, 122].

the two heavy holes is sufficient for a vanishing δ_{ehx} because $\langle J_x^h \rangle = \langle J_y^h \rangle = 0$ up to corrections of order $\Delta_3/\Delta_{\mathrm{hh-lh}} \ll 1$, cf. Eq. (2.39). We now discuss the stability of the compensation of the electron-hole exchange interaction for an X^+ in the presence of external magnetic fields and anisotropy of the quantum dot shape. The p symmetry of the v-band states is responsible for the hyperfine interaction being much weaker than for the c-band states (which have s symmetry). We therefore neglect the Overhauser field for the holes and discuss external magnetic fields only. We treat the Zeeman interaction H_Z^v for the v-band holes [116] in first-order perturbation theory, where

$$H_Z^v = \frac{e}{m_0 c} \sum_{i=x,y,z} \left[\kappa J_i^h + q (J_i^h)^3\right] B_i, \tag{2.43}$$

with the Zeeman parameters κ and q. The term that is cubic in J^h is usually much smaller than the linear term and is often neglected [103]. Yet, by restricting ourselves to heavy holes we can use $(J_i^h)^2 = 9/4$ and define an effective hole g-factor $g_i^h = \kappa + 9q/4$ such that the (exact) Zeeman interaction is given by $H_Z = \sum_i g_i^h J_i^h B_i$. For $B = 0$, $\langle J_z^{h1} + J_z^{h2} \rangle = 0$ is satisfied due to the Kramers theorem and the electron-hole exchange interaction vanishes exactly for an X^+ in a quantum dot. For a circular quantum dot, $\langle J_z^{h1} + J_z^{h2} \rangle = 0$ remains true for $\mathbf{B}$ along z ($\mathbf{B} = \mathbf{B}_\perp$) or in the xy plane ($\mathbf{B} = \mathbf{B}_\parallel$). In the latter case, this is because the lh components $|\pm 1/2\rangle$ are admixed with equal weight. Yet, for $\mathbf{B} = c_\perp \mathbf{B}_\perp + c_\parallel \mathbf{B}_\parallel$ this is no longer true and $\langle J_z^{h1} + J_z^{h2} \rangle \propto (g_\parallel^h c_\parallel B_\parallel)(g_z^h c_\perp B_\perp)/\Delta_{\mathrm{hh-lh}}^2$. Typically, $(g_z^h c_\perp B_\perp)/\Delta_{\mathrm{hh-lh}} < 0.1$ for magnetic fields $B < 10\,\mathrm{T}$, and the in-plane hole g factor $g_\parallel^h$ is very small, $g_\parallel^h \approx 0$. For heavy holes $g_\parallel^h = 0$ is even satisfied exactly, which follows directly from $\langle J_x \rangle = \langle J_y \rangle = 0$. Only the admixture of light holes leads to a non-zero $g_\parallel^h$. For a more detailed discussion of angular momentum $j = 3/2$ states in quasi two-dimensional systems see Ref. [117]. We have shown above that the admixture of light holes is negligible for circular dots. We therefore conclude that for a X^+ in a circular dot a perturbation by a (weak) magnetic field only induces a negligible exchange splitting. Moreover, for strong magnetic fields which induce a Zeeman splitting that is much larger than the electron-hole exchange splitting, the electron-hole exchange can be neglected even for neutral excitons, for which circularly polarized states $|\pm\frac{3}{2}, \mp\frac{1}{2}\rangle$ are then good eigenstates [118]. For a quantum dot with broken rotational symmetry in the xy plane, $\langle J_z^{h1} + J_z^{h2} \rangle = 0$ is still obtained as long as reflection symmetry along the z axis is given. In this case, the states with opposite z component are admixed with equal amplitudes, similarly as for a magnetic field $\mathbf{B}_\parallel$, and there is no exchange splitting. If reflection symmetry along z is broken, then the mixing of hh and lh states is determined by a new parameter, the anisotropy energy divided by $\Delta_{\mathrm{hh-lh}}$. The exciton fine structure splitting can only be neglected if this parameter is small. The anisotropy energy depends crucially on the individual quantum dot shape. For further predictions on the anisotropy energy and related effects, a more detailed numerical modelling of the quantum dot is usually required [119], which is not within the scope of this thesis.

2.9 Entangled two-photon state

Full *bipartite* photon entanglement of the first photon pair is obtained in Eqs. (2.34) and (2.35) by a measurement of the second photon pair which projects the GHZ state into a state where the two photon pairs form a product state. This can be achieved, e.g., by directing the second photon pair (which is emitted some time after the first photon pair) via secondary optical paths to a linear polarization measurement which is performed *before* the first photon pair is measured, see Figure 2.6. Even different bases $\{|H\rangle, |V\rangle\}$ and $\{|H'\rangle, |V'\rangle\}$ can be chosen for the two photons of the second pair. The four-photon states Eqs. (2.34) and (2.35) read in this basis

$$\begin{aligned} |\Psi^{\pm}\rangle &\rightarrow \left(|\sigma^+\sigma^-\rangle \pm |\sigma^-\sigma^+\rangle\right)\left(|HH'\rangle - |VV'\rangle\right) \\ &\quad + \left(|\sigma^+\sigma^-\rangle \mp |\sigma^-\sigma^+\rangle\right)\left(|HV'\rangle - |VH'\rangle\right), \qquad (2.44) \\ |\Phi^{\pm}\rangle &\rightarrow \left(|\sigma^-\sigma^-\rangle \pm |\sigma^+\sigma^+\rangle\right)\left(|HH'\rangle + |VV'\rangle\right) \\ &\quad + \left(|\sigma^-\sigma^-\rangle \mp |\sigma^+\sigma^+\rangle\right)\left(|HV'\rangle + |VH'\rangle\right). \qquad (2.45) \end{aligned}$$

Note that the electron-hole exchange interaction in elliptical dots assists this projection into a linear basis, as discussed in Section 2.7. Further, even loss of the (linear) polarization coherence of the second photon pair is tolerable in Eqs. (2.44) and (2.45) if the intrinsic linear polarization bases of the dots are chosen for H, V and H', V', respectively. Yet, the entanglement of the first photon pair is only preserved if the *relaxation* time $T_{1,X}$ of the linear exciton polarization is longer than the exciton lifetime τ_X. Otherwise, the four photons are in a completely mixed state. However, such long exciton polarization relaxation times have been reported in several experiments [120, 121, 122]. We therefore assume $T_{1,X} \gg \tau_X$ in the following. If the second photon pair is measured in the state $|HH'\rangle$ or $|VV'\rangle$, the electron Bell states have given rise to the two-photon states

$$\begin{aligned} |\Psi^{\pm}\rangle &\rightarrow |{+1}, \theta_1, \phi_1\rangle_L\, |{-1}, \theta_2, \phi_2\rangle_R \pm |{-1}, \theta_1, \phi_1\rangle_L\, |{+1}, \theta_2, \phi_2\rangle_R, \qquad (2.46) \\ |\Phi^{\pm}\rangle &\rightarrow |{+1}, \theta_1, \phi_1\rangle_L\, |{+1}, \theta_2, \phi_2\rangle_R \pm |{-1}, \theta_1, \phi_1\rangle_L\, |{-1}, \theta_2, \phi_2\rangle_R. \qquad (2.47) \end{aligned}$$

Here, we consider arbitrary emission directions and have omitted normalization for simplicity. Obviously, the two-photon states (2.46) and (2.47) are maximally entangled for $\theta_1 = \theta_2 = 0$. For $\theta_1 = \theta_2 \in (0, \pi/2)$, the total relative phase factor between the two-photon states in Eq. (2.46) is $\exp(i\gamma + 2i\Delta\phi)$. Here, $\Delta\phi = \phi_1 - \phi_2$, $\gamma = \pi$ for $|\Psi^-\rangle$, and $\gamma = 0$ for $|\Psi^+\rangle$. For Eq. (2.47), the relative phase factor is $\exp[i\gamma + 2i(\phi_1 + \phi_2)]$, with $\gamma = \pi$ for $|\Phi^-\rangle$ and $\gamma = 0$ for $|\Phi^+\rangle$. By tuning the relative phase factors in Eqs. (2.46) and (2.47) to -1, two circularly polarized photons can be recovered for $\theta_1 = \theta_2 \in (0, \pi/2)$ from the elliptically polarized single-photon states due to quantum mechanical interference. Explicitly, the maximally entangled two-photon state $\left(|\sigma^+\rangle_L|\sigma^-\rangle_R - |\sigma^-\rangle_L|\sigma^+\rangle_R\right)/\sqrt{2}$ is created from $|\Psi^-\rangle$ for $\Delta\phi = 0\ (\mathrm{mod}\pi)$ and from $|\Psi^+\rangle$ for $\Delta\phi = \pi/2\ (\mathrm{mod}\pi)$. Further, another maximally entangled two-photon state $\left(|\sigma^-\rangle_L|\sigma^-\rangle_R - |\sigma^+\rangle_L|\sigma^+\rangle_R\right)/\sqrt{2}$ is obtained from $|\Phi^-\rangle$ for $\phi_1 + \phi_2 = 0\ (\mathrm{mod}\pi)$,

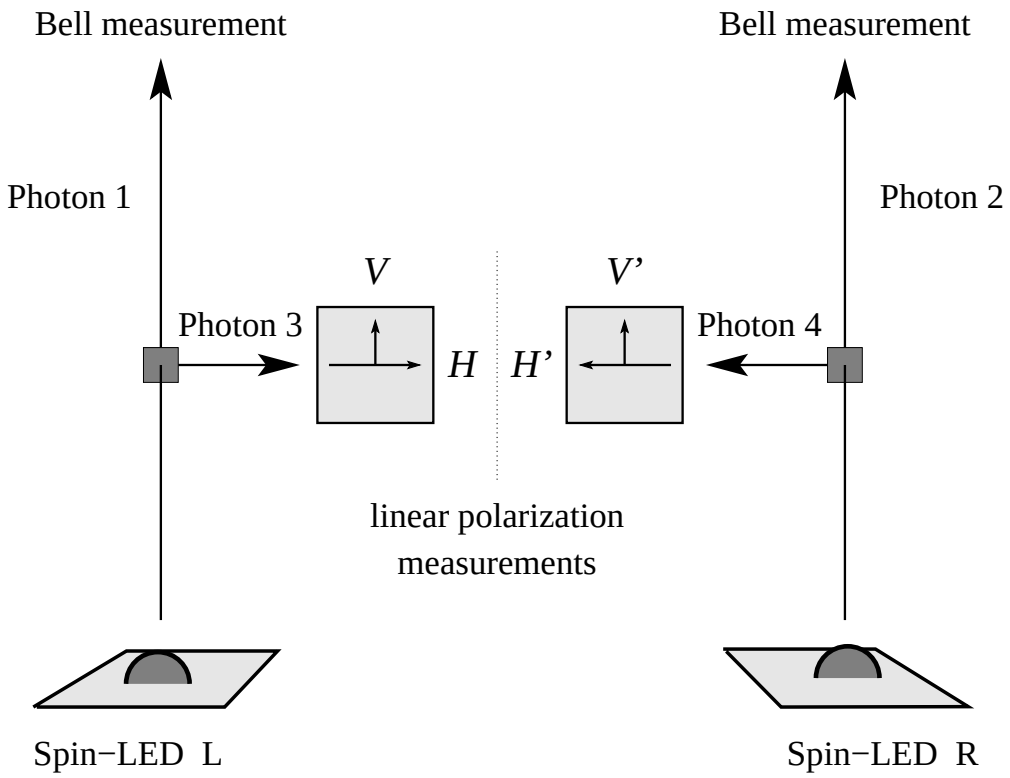

Figure 2.6: A scheme how to extract and measure two-photon entanglement of the four-photon GHZ states Eqs. (2.34) and (2.35). Photons 3 and 4 are directed towards a measurement in linear polarization. For asymmetric quantum dots, the linear bases H, V and H', V' are preferably chosen along the (intrinsic) exciton polarization axes. As described in the text, the photons 1 and 2 are entangled after detection of the photons 3 and 4, which can be detected with a subsequent Bell measurement.

and from $|\Phi^+\rangle$ for $\phi_1+\phi_2=\pi/2$ (modπ). Thus, maximal entanglement is transferred from two electron spins to the polarizations of two photons for certain ideal emission angles. Further, such ideal angles can readily be identified for an arbitrary relative phase γ of the two-electron state. Note that for $\theta_1=\theta_2=\pi/2$ the two-photon states vanish completely due to destructive interference.

The conditions for maximum entanglement of the four-photon GHZ states Eqs. (2.34) and (2.35) for arbitrary emission directions can be obtained analogously to the two-photon states. If the entangled electron pair is in the state $|\Psi_-\rangle$, $\phi_1-\phi_2-\phi_3+\phi_4=0$ (modπ) must be satisfied, and $\phi_1-\phi_2-\phi_3+\phi_4=\pi/2$ (modπ) for $|\Psi_+\rangle$. Further, $\phi_1+\phi_2-\phi_3-\phi_4=0$ (modπ) must be satisfied for $|\Phi_-\rangle$, and $\phi_1+\phi_2-\phi_3-\phi_4=\pi/2$ (modπ) for $|\Phi_+\rangle$.

We finally mention that an alternative scheme to achieve bipartite photon entanglement can be realized as follows [123]. After emission of the first photon pair the two photons and the two holes are in the state Eq. (2.33). A Hadamard operation can now be performed on the hh states, e.g., via an optical Raman transition [124]. This produces states that are analogous to Eqs. (2.44) and (2.45), since the holes are brought into a coherent superposition $\propto|3/2\rangle\pm|-3/2\rangle$, respectively. The hole spins can now be measured in the z basis, e.g., via state-selective absorption of circularly polarized photons [125]. This procedure projects Eq. (2.33) into a state with full entanglement of the photons, where the relative phase of the two-photon state is different for aligned or anti-aligned hole spins (similarly as for the linear polarizations H,V and H',V').

2.10 Polarization entanglement of the photons

For arbitrary emission directions of the two photons, described by the pure states Eqs. (2.46) and (2.47), the degree of polarization entanglement can be quantified by the von Neumann entropy $E=-\mathrm{tr}_2(\tilde{\rho}\log_2\tilde{\rho})$ [8]. Here, $\tilde{\rho}=\mathrm{tr}_1\rho_{2ph}$, where ρ_{2ph} is the two-photon density operator and tr_i is the trace taken over the Hilbert space of photon i. For a maximally entangled two-photon state $E=1$, while $E=0$ represents a pure state $\tilde{\rho}$ (which implies the absence of bipartite entanglement). If the two electrons recombine after times much shorter than the spin lifetimes T_1, T_1', T_2, T_2', E oscillates for Eq. (2.46) as a function of $\Delta\phi$ of the two emitted photons between a minimal value,

$$E_{\min}=\log_2(1+x_1x_2)-\frac{x_1x_2}{1+x_1x_2}\log_2(x_1x_2), \tag{2.48}$$

and a maximal value that is (only) obtained for the ideal angles ϕ_1 and ϕ_2 mentioned above,

$$E_{\max}=\log_2(x_1+x_2)-\frac{x_1\log_2(x_1)}{x_1+x_2}-\frac{x_2\log_2(x_2)}{x_1+x_2}, \tag{2.49}$$

see Figure 2.7. In Eqs. (2.48) and (2.49), $x_i=\cos^2\theta_i$. For Eq. (2.47), E oscillates between $E_{\min}$ and $E_{\max}$ as a function of $\phi_1+\phi_2$. As expected, $E_{\max}=1$ for all

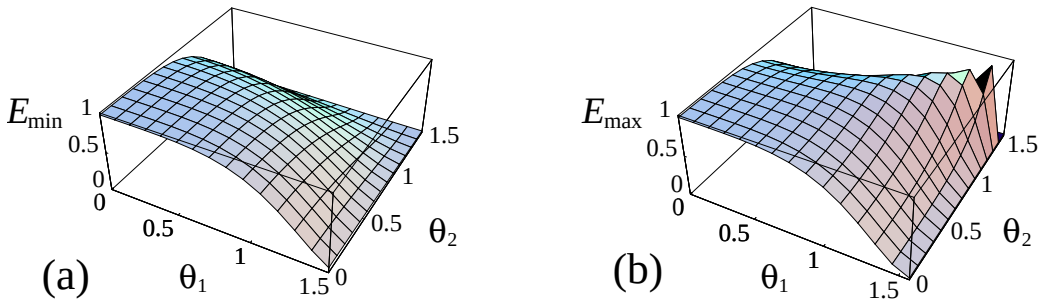

Figure 2.7: The von Neuman entropy (a) $E = E_{\min}$ and (b) $E = E_{\max}$ as a function of the polar angles θ_1 and θ_2 for photon emission. Depending on the azimuthal angles ϕ_1 and ϕ_2, E oscillates between (a) and (b). The photon-polarization entanglement is maximal for emission along the spin quantization axis ($\theta_1 = \theta_2 = 0$). For small θ_i entanglement is only weakly reduced, while even $E_{\max} = 1$ is exactly satisfied for the continuous set of directions $\theta_1 = \theta_2 \in [0, \pi/2)$, as explained in Section 2.9. If at least one of the photons is emitted in-plane ($\theta_i = \pi/2$), entanglement is absent.

$\theta_1 = \theta_2 \in [0, \pi/2)$. Note that the discontinuity in $E_{\max}$ for $\theta_1 = \theta_2 = \pi/2$ is due to the vanishing two-photon state.

Allowing for small deviations $\delta\theta = \theta_1 - \theta_2$ and $\delta\phi = \phi_1 - \phi_2$ from the ideal emission angles, we expand the two-photon density matrix in $\delta\phi$ and $\delta\theta$ and recalculate the von Neumann entropy. For $|\Psi^-\rangle$ we obtain, e.g., for the ideal configuration with $\theta = \pi/11$ and $\phi = 0$ a maximum reduction of E by less than 6% with $\delta\theta \in [-\pi/11, 0]$ and $\delta\phi \in [0, \pi/4]$.

2.11 Conclusion

In this chapter, we have studied the transfer of entanglement from electron spins to photon polarizations [71]. We have discussed the generation of entangled four-photon and two-photon states by the injection of spin-entangled electrons into quantum dots with two excess holes. We have proposed a scheme to achieve complete entanglement transfer from two electron spins to two photons with state-of-the-art quantum dots. We have shown the dependence of the entanglement on the emission angles and identified the conditions for maximal entanglement. Surprisingly, due to quantum mechanical interference, the fidelity for the entanglement conversion approaches unity not only for photon emission along the spin quantization axis, but for a continuous set of observation directions. This offers the possibility to efficiently test Bell's inequalities for electron spins. We have also discussed the influence of deviations from the ideal configuration. We have estimated that the loss of entanglement under realistic experimental conditions is smaller than a few percent.

Chapter 3

Biexcitons in coupled quantum dots as a source of entangled photons

Biexcitons consist of two excitons, bound together by an (all in all) attractive Coulomb interaction. Biexcitonic states have been investigated in many experiments in single quantum dots [126, 127, 128, 129, 130, 131, 132, 65, 133, 66]. In this chapter we study biexcitons in two tunnel-coupled quantum dots [134]. In view of the comparison of quantum dots with artificial atoms, coupled quantum dots are similar to artificial molecules. In tunnel-coupled dots, charge carriers are delocalized due to an overlap of the single-dot wave functions. Coupling of quantum dots can also be established via the electromagnetic field, e.g., via a cavity mode (see Chapter 6), via the electrostatic interaction of excitons, or via Förster transfer of excitons. Electrostatically coupled quantum dots have been theoretically studied with respect to applications in quantum information processing [135]. Förster transfer between quantum dots has been shown to induce entanglement of exciton number states [136] and to transfer spin and energy of excitons [137].

Here, we study the production of polarization-entangled photons using two tunnel-coupled quantum dots, including the electrostatic interaction of excitons. Tunnel-coupled double quantum dots can be formed with cleaved-edge overgrowth [138] or with self-assembled dots, e.g., by prepatterning of the substrate for lateral coupling [139] or by growth of vertically stacked dots [140, 141, 142, 143]. Single excitons in coupled dots have been observed in experiment [138, 142, 143] and have also been studied numerically using correlated pseudopotential calculations [144]. We show within a (analytical) model from molecular physics that for a ground-state biexciton, spin entanglement is provided by delocalized pairs of charge carriers and is transferred to polarization-entangled photons through a decay cascade. Alternatively, spin-entangled electrons can be optically generated with this scheme. Here, a double dot simplifies the spatial separation of the entangled electrons. Biexcitons in quantum

dots can be generated by electrical injection of two electrons and two holes [63] or by optical excitation with sufficiently low laser intensities [133].

In Section 3.1 we present our model for the double dot and for the single-particle wave functions. In Section 3.2 we use the Heitler-London method for a variational ansatz for the biexciton wave function in the double dot. We obtain analytical expressions for the low-lying energies of biexciton states in the presence of externally applied magnetic and electric fields. Using a Heitler-London ansatz for delocalized electrons, in Section 3.3 we calculate the low-lying energies of two positively charged excitons in a double dot. In Section 3.4 we calculate oscillator strengths for the optical transitions that give rise to the emission of entangled photons. In Section 3.5 we discuss the conditions that need to be satisfied for the production of polarization-entangled photons and we conclude in Section 3.6.

3.1 Model

We consider two identical two-dimensional quantum dots labeled by $D = 1, 2$ which are laterally tunnel-coupled. An external magnetic field $\mathbf{B} = B\hat{\mathbf{z}}$ with $\hat{\mathbf{z}} = (0, 0, 1)$ is applied perpendicular to the plane and an electric field $\mathbf{E} = \varepsilon \mathbf{n}_\parallel$ is applied in the plane, where $\mathbf{n}_\parallel = (n_x, n_y, 0)$ with $n_x^2 + n_y^2 = 1$. We formulate our model here already in the form used in Section 3.3, i.e., for two electrons and four holes. The Hamiltonian for the particles $\alpha_i \in \{e_1, e_2, h_1, h_2, h_3, h_4\}$ in the double dot is given by

$$H = \sum_{\alpha i} H_{\alpha i} + H_C + H_Z. \tag{3.1}$$

In Section 3.2 we consider two neutral excitons in the double dot and the holes h_3 and h_4 are discarded. As introduced in Section 1.3, we consider type I quantum dots with zincblende structure and restrict the valence band to the heavy-hole states. The orbital single-particle energy of a carrier is given by

$$H_{\alpha i} = \frac{1}{2m_\alpha}\left[\mathbf{p}_{\alpha i} + \frac{q_\alpha}{c}\mathbf{A}(r_{\alpha i})\right]^2 + V_\alpha(\mathbf{r}_{\alpha i}) - q_\alpha \mathbf{E}\cdot\mathbf{r}_{\alpha i}. \tag{3.2}$$

For electrons ($\alpha = e$), the charge is $q_\alpha = -e$ and the effective mass $m_\alpha = m_e$, whereas for holes ($\alpha = h$), $q_\alpha = +e$ and $m_\alpha = m_h$. The vector potential is taken in the symmetric gauge, $\mathbf{A}(\mathbf{r}) = (\mathbf{B}\times\mathbf{r})/2$. The double dot potential is chosen as

$$V_\alpha(\mathbf{r}) = \frac{m_\alpha \omega_\alpha^2}{2}\left[\frac{1}{4a^2}\left(x^2 - a^2\right)^2 + y^2\right], \tag{3.3}$$

where the two dots are centered at $(\pm a, 0, 0)$ and ω_α are confinement frequencies. Using the Zeeman term Eq. (2.43) for the holes, the Zeeman interaction is obtained as

$$H_Z = \mu_\mathrm{B} B\left(g_z^e \sum_i S_z^{e,i} + g_z^h \sum_i J_z^{h,i}\right) \tag{3.4}$$

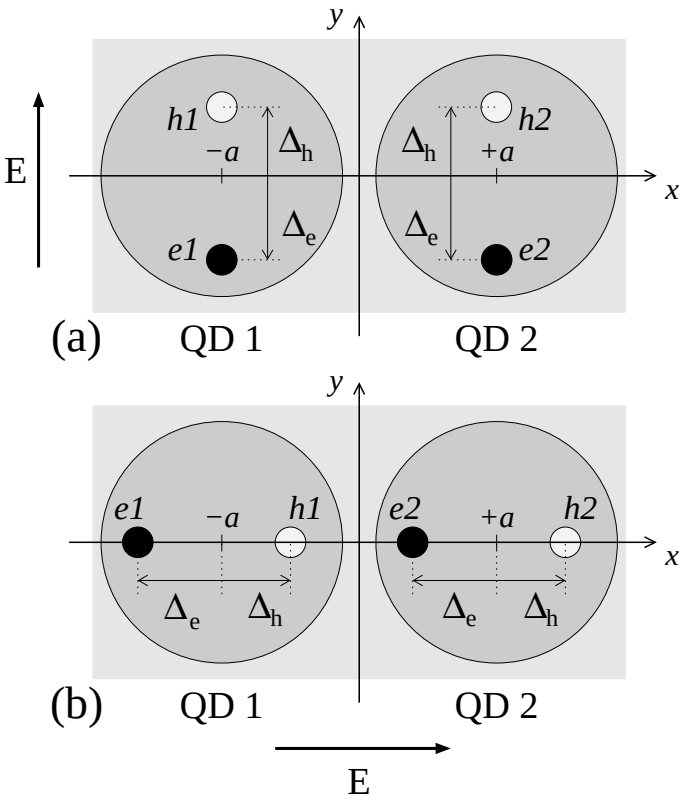

Figure 3.1: Scheme of the mean positions of electrons (black circles) and holes (white circles) in parabolic quantum dots located at $(\pm a, 0, 0)$ in presence of an in-plane electric field (a) $\mathbf{E} = \epsilon\hat{\mathbf{y}}$ and (b) $\mathbf{E} = \epsilon\hat{\mathbf{x}}$. The particles are shifted away from the dot centers due to $\mathbf{E}$ by distances $\Delta_\alpha = q_\alpha \varepsilon / m_\alpha \omega_\alpha^2$. Note that the inter-dot distances between electrons and holes are different in (a) and (b).

and comprises the Bohr magneton μ_B, the effective g factors g_z^α, the spin $S_z^{e,i}$ of the conduction-band electrons, and the total angular momentum projection $J_z^{h,i}$ of the heavy holes. Using $(J_z^h)^2 = 9/4$, we have defined g_z^h such that the typically small cubic term $\propto (J_z^h)^3$ is absorbed in the linear term.

The Coulomb interaction between the carriers in the double dot is described by $H_C = (1/2)\sum_{\alpha i \neq \beta j} C_{\alpha i,\beta j}$, where $C_{\alpha i,\beta j} = q_\alpha q_\beta / \kappa |\mathbf{r}_{\alpha i} - \mathbf{r}_{\beta j}|$ with the (low-frequency) dielectric constant κ.

Below, we use Fock-Darwin states [145, 146] as approximate solutions of the single-particle Hamiltonians Eq. (3.2). Fock-Darwin states are harmonic oscillator states that are obtained for a harmonic confinement in the presence of a perpendicular magnetic field. In the single-particle Hamiltonians $H_{\alpha i}$ we form Fock-Darwin Hamiltonians $h_{\alpha i}^{\pm a}(\mathbf{r}_{\alpha i})$ which contain parabolic potentials $v_\alpha^{\pm a}(\mathbf{r}_{\alpha i})$ centered at $(\pm a, 0, 0)$ and with frequencies ω_α. For compensation, we obtain in $H_{\alpha i}$ an additional term describing the difference of the double dot potential Eq. (3.3) and the parabolic po-

tentials,

$$H_W = \sum_{\alpha i} V_\alpha(\mathbf{r}_{\alpha i}) - v_e^{-a}(\mathbf{r}_{e1}) - v_e^{+a}(\mathbf{r}_{e2}) - \sum_{i=1}^{2}[v_h^{-a}(\mathbf{r}_{h,2i-1}) + v_h^{+a}(\mathbf{r}_{h,2i})]. \tag{3.5}$$

The single-particle Fock-Darwin ground-state energies are given by $b_\alpha \hbar\omega_\alpha$, where $b_\alpha = \sqrt{1 + (eB/2cm_\alpha\omega_\alpha)^2}$ characterizes the effect of the magnetic field on the confinement. Further, the electric field $\mathbf{E} = \varepsilon \mathbf{n}_\parallel$ shifts the parabolas $v_\alpha^{\pm a}(\mathbf{r})$ in the xy plane by distances $\Delta_\alpha = q_\alpha \varepsilon / m_\alpha \omega_\alpha^2$ to the final positions $\mathbf{a}_{\alpha 1} = (-a + n_x\Delta_\alpha, n_y\Delta_\alpha, 0)$ and $\mathbf{a}_{\alpha 2} = (a + n_x\Delta_\alpha, n_y\Delta_\alpha, 0)$, respectively, see Figure 3.1. Consequently, the electric field is readily included into the Fock-Darwin Hamiltonians by the transformations $h_{\alpha i}^{\pm a}(\mathbf{r}_{\alpha i}) \to h_{\alpha i}^{\mathbf{a}_{\alpha D}}(\mathbf{r}_{\alpha i})$. Additionally, the field component in the x direction shifts the energy levels of dot 1 and 2 relative to each other by $2n_x ae\varepsilon$. In the case of dots with misaligned levels (e.g., for dots with different sizes), this energy shift can be used to tune levels of the two dots into resonance [74, 147]. Resonant coupling of the ground state of carrier α in one dot with the first excited state of the other dot is avoided for electric fields satisfying $\varepsilon < \varepsilon_{\max} = \hbar\omega_\alpha / 2n_x ae$.

Finally, the total orbital single-particle energies in Eq. (3.1) are given by $\sum_{\alpha i} H_{\alpha i} = H_0 + H_W$, where H_W is given by Eq. (3.5) and

$$H_0 = \sum_{\alpha i} \left[h_{\alpha i}^{\mathbf{a}_{\alpha D}}(\mathbf{r}_{\alpha i}) - \frac{\hbar\omega_\alpha}{2} \left(\frac{\Delta_\alpha}{a_\alpha} \right)^2 \right], \tag{3.6}$$

with $a_\alpha = \sqrt{\hbar / m_\alpha \omega_\alpha}$.

For the excitonic wave functions, we assume the strong confinement regime $a_X \gg a_e, a_h$, where a_X is the exciton radius in the bulk crystal and a_α the effective Bohr radius of the electron or the hole inside the dot. In this regime, the single-particle envelope wave functions are defined by the quantum dot potential and the Coulomb interaction can be included as a perturbation in first order. According to the Hamiltonians $h_{\alpha i}^{\mathbf{a}_{\alpha D}}(\mathbf{r}_{\alpha i})$, we use Fock-Darwin ground states

$$\langle \mathbf{r}|D\rangle_\alpha = \sqrt{\frac{b_\alpha}{\pi a_\alpha^2}} \exp\left(-\frac{b_\alpha}{2a_\alpha^2} (\mathbf{r} - \mathbf{a}_{\alpha D})^2 \right) \exp\left(\frac{iq_\alpha}{2el_B^2} (\hat{\mathbf{z}} \times \mathbf{a}_{\alpha D}) \cdot \mathbf{r} \right) \tag{3.7}$$

for the envelope functions centered at $\mathbf{a}_{\alpha D}$. Here, the phase factor containing the magnetic length $l_B = \sqrt{\hbar c / eB}$ is obtained from a gauge transformation of the vector potential, $\mathbf{A}_{\mathbf{a}_{\alpha D}} = (1/2)\mathbf{B} \times (\mathbf{r} - \mathbf{a}_{\alpha D}) \to \mathbf{A} = (1/2)\mathbf{B} \times \mathbf{r}$.

3.2 Biexciton in a double dot

For the orbital biexciton wave function in the double dot we form the product $|\Phi_e\rangle^e \otimes |\Phi_h\rangle^h$ of a two-electron and a two-hole orbital wave function. This product ansatz

for the biexciton wave function is suitable for the strong-confinement regime where the Coulomb interaction between carriers can be treated as a perturbation. For the biexciton we consider two situations. The carriers can be delocalized in the double dot, similarly as for a dimer in molecular physics. Alternatively, the carriers can be localized in one of the dots. For the delocalized case, we form two-particle states $|\Phi_\alpha\rangle^\alpha$ according to the Heitler-London method [148, 72, 74],

$$|\Phi_\alpha\rangle^\alpha \equiv |I\rangle^\alpha = N_{\alpha I}(|12\rangle_\alpha + (-1)^I|21\rangle_\alpha), \tag{3.8}$$

where $I = 0$ ($I = 1$) for the spin singlet (triplet). For simplicity, we use here the terms singlet and triplet also for the holes (in spite of their different spin algebra). In the two-particle states $|DD'\rangle_\alpha = |D\rangle_{\alpha 1}\otimes|D'\rangle_{\alpha 2}$ the particle α_1 is located on dot D and the particle α_2 on dot D'. Furthermore, $N_{\alpha I} = 1/\sqrt{2(1+(-1)^I|S_\alpha|^2)}$ is a normalization constant where $S_\alpha = {}_\alpha\langle 1|2\rangle_\alpha$ denotes the overlap (or tunneling amplitude) between the two orbital wave functions $|1\rangle_\alpha$ and $|2\rangle_\alpha$ [Eq. (3.7)]. A Heitler-London ansatz is suitable for a tunnel-coupled double dot because the single-particle orbitals are defined by the strong quantum dot confinement. A tunnel-coupled system of two identical dots is with this respect very similar to a H_2 molecule. This is in stark contrast to biexcitons in the bulk for which the Heitler-London ansatz fails for some values of $\xi = m_e/m_h$ [149]. The four resulting orbital biexciton states are

$$|IJ\rangle = |I\rangle^e \otimes |J\rangle^h = \frac{|1212\rangle + (-1)^I|2112\rangle + (-1)^J|1221\rangle + (-1)^{I+J}|2121\rangle}{2\sqrt{(1+(-1)^I|S_e|^2)(1+(-1)^J|S_h|^2)}}, \tag{3.9}$$

where the entries of the four-particle kets indicate the dot D of e_1, e_2, h_1, and h_2. We apply the notation $|IJ\rangle \in \{|ss\rangle, |st\rangle, |ts\rangle, |tt\rangle\}$ for the biexciton states, according to the spin configuration, where $s \equiv 0$ and $t \equiv 1$. The corresponding singlet and triplet spin wave functions for the two electrons are

$$|\chi_s\rangle_e = \frac{1}{\sqrt{2}}\left(|u_{c,+\frac{1}{2}}\rangle|u_{c,-\frac{1}{2}}\rangle - |u_{c,-\frac{1}{2}}\rangle|u_{c,+\frac{1}{2}}\rangle\right), \tag{3.10a}$$

$$|\chi_{t_0}\rangle_e = \frac{1}{\sqrt{2}}\left(|u_{c,+\frac{1}{2}}\rangle|u_{c,-\frac{1}{2}}\rangle + |u_{c,-\frac{1}{2}}\rangle|u_{c,+\frac{1}{2}}\rangle\right), \tag{3.10b}$$

$$|\chi_{t_\uparrow}\rangle_e = |u_{c,+\frac{1}{2}}\rangle|u_{c,+\frac{1}{2}}\rangle, \tag{3.10c}$$

$$|\chi_{t_\downarrow}\rangle_e = |u_{c,-\frac{1}{2}}\rangle|u_{c,-\frac{1}{2}}\rangle, \tag{3.10d}$$

where $|u_{c,\pm\frac{1}{2}}\rangle$ is a conduction-band (c-band) Bloch function for spin $\pm 1/2$. For the valence-band (v-band) holes, we form wave functions $|\chi_s\rangle_h$, $|\chi_{t_0}\rangle_h$, $|\chi_{t_\uparrow}\rangle_h$, $|\chi_{t_\downarrow}\rangle_h$ analogously to Eq. (3.10) by replacing $|u_{c,\pm\frac{1}{2}}\rangle \to |u_{v,\pm\frac{3}{2}}\rangle$.

The energies of the biexciton states $|IJ\rangle$ can be calculated analytically using the Hamiltonian (3.1),

$$E_{IJ} = \langle IJ|H|IJ\rangle = E^0 + E^W_{IJ} + E^C_{IJ} + E^Z, \tag{3.11}$$

where we define $E^A_{IJ} \equiv \langle IJ|H_A|IJ\rangle$. In units of $\hbar\omega_e$, we obtain the single-particle energies

$$E^0 \equiv E^0_{IJ} = 2\left(b_e + \frac{b_h}{\eta}\right) - \left(\frac{\Delta_e}{a_e}\right)^2 - \frac{1}{\eta}\left(\frac{\Delta_h}{a_h}\right)^2, \tag{3.12}$$

where $\eta = \omega_e/\omega_h$. Further, the Coulomb energy is obtained as

$$\begin{aligned} E^C_{IJ} &= \frac{E_{ee} + (-1)^I \tilde{E}_{ee}}{1 + (-1)^I S_e^2} + \frac{E_{hh} + (-1)^J \tilde{E}_{hh}}{1 + (-1)^J S_h^2} \\ &\quad + 2\frac{E_X + E_{eh} + (-1)^I S_e \tilde{E}_{Xe} + (-1)^J S_h \tilde{E}_{Xh} + (-1)^{I+J} S_e S_h \tilde{E}_{Xeh}}{[1 + (-1)^I S_e^2][1 + (-1)^J S_h^2]}. \end{aligned} \tag{3.13}$$

Here, $S_e = \exp[-d^2(2b_e - 1/b_e)]$ and $S_h = \exp[-d^2(2b_h - 1/b_h)/\xi\eta]$ (see Appendix A.1), where $\xi = m_e/m_h$ and $d = a/a_e$ is half the inter-dot distance in units of the electron Bohr radius. The results for the different matrix elements represented by symbols $E_{\alpha\beta}, \tilde{E}_{\alpha\beta}$ in above expression are given in the Appendix A, where we have considered the orientations $\mathbf{E} = \varepsilon\hat{\mathbf{y}}$ and $\mathbf{E} = \varepsilon\hat{\mathbf{x}}$ of the electric field. Note that an electric field in general does not change the relative distance of two carriers with identical charge. Consequently, an electric field reduces the attractive Coulomb interaction but does not alter the repulsive interaction of the carriers in the double dot. For an in-plane electric field $\mathbf{E} = \varepsilon(n_x, n_y, 0)$, we obtain for the matrix element of the term H_W,

$$\begin{aligned} E^W_{IJ} &= \frac{3}{16d^2}\left(\frac{1}{b_e^2} + \frac{\xi}{b_h^2}\right) - \frac{3d^2}{4}\left(1 + \frac{1}{\xi\eta^2}\right) \\ &\quad + \frac{(n_x\Delta_e)^2}{4d^2a_e^2}\left(\frac{3}{b_e} + \frac{(n_x\Delta_e)^2}{a_e^2}\right) + \frac{(n_x\Delta_h)^2}{4\xi\eta^2 d^2 a_e^2}\left(\frac{3\xi\eta}{b_h} + \frac{(n_x\Delta_h)^2}{a_e^2}\right) \\ &\quad + 3N_{IJ}\left[d^2\left(1 + \frac{1}{\xi\eta^2}\right) + (-1)^J S_h^2\left(d^2 - \frac{1}{\eta b_h} - 2\frac{(n_x\Delta_h)^2}{a_e^2}\right)\right. \\ &\quad + (-1)^I S_e^2\left(\frac{d^2}{\xi\eta^2} - \frac{1}{b_e} - 2\frac{(n_x\Delta_e)^2}{a_e^2}\right) \\ &\quad \left. - (-1)^{I+J} S_e^2 S_h^2\left(\frac{1}{b_e} + \frac{1}{\eta b_h} + 2\frac{n_x^2(\Delta_e^2 + \Delta_h^2)}{a_e^2}\right)\right], \end{aligned} \tag{3.14}$$

which only depends on the electric field component εn_x along the inter-dot axis because H_W is independent of the coordinates $y_{\alpha i}$. Further, we define $N_{IJ} = N_{eI}^2 N_{hJ}^2$.

Up to this point we have focused on a delocalized biexciton in the double dot. We next consider the energy $\bar{E}_D$ of the states $|DDDD\rangle$ where all carriers occupy the same dot D. Unlike carriers of equal charge, two electron-hole pairs can attract or repel each other, depending on their wave functions. It therefore depends on various parameters if the biexciton ground state is a localized or a delocalized state in a double dot. In units of $\hbar\omega_e$, we obtain $\bar{E}_D = E^0 + E^Z + \bar{E}^W_D + \bar{E}^C$, where E^0 and E^Z

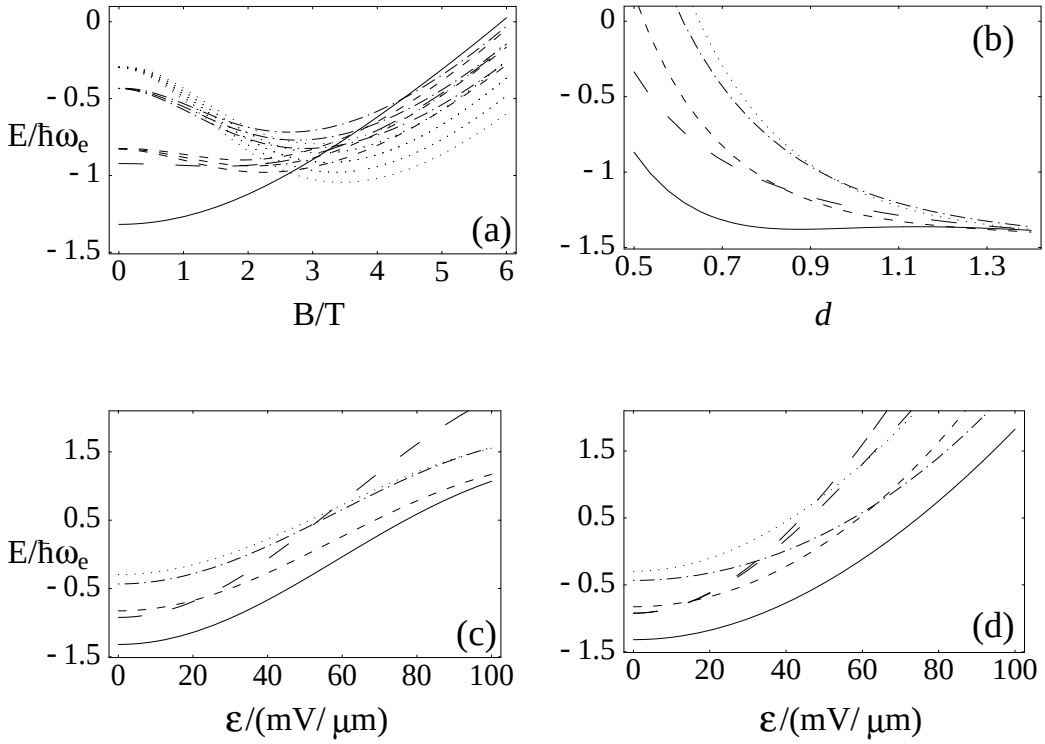

Figure 3.2: Biexciton energies in units of $\hbar\omega_e$ as a function of (a) a magnetic field $\mathbf{B} = B\hat{\mathbf{z}}$ (including the Zeeman interaction with $|g_e| = |g_h| = 1$), (b) half the inter-dot distance $d = a/a_e$, (c) an electric field $\mathbf{E} = \varepsilon\hat{\mathbf{y}}$, (d) an electric field $\mathbf{E} = \varepsilon\hat{\mathbf{x}}$. We have set $\varepsilon = 0$ in (a) and (b), $B = 0$ in (b), (c), and (d), and $d = 0.7$ in (a), (c) and (d). Further, we have used effective masses for a GaAs quantum well, $m_e = 0.067m_0$, $m_{hh} = 0.112m_0$, and $\hbar\omega_e = 3$ meV, $\eta = 1/\xi = 1.67$ (implying $a_e = a_h$). For these parameters, $a_e \approx 20\,\mathrm{nm}$. The plotted single-occupancy energies E_{IJ} are E_{ss} (solid line), E_{st} (short-dashed line), E_{ts} (dot-dashed line), and E_{tt} (dotted line). The exciton double-occupancy energies $\bar{E}_1$ and $\bar{E}_2$ (long-dashed lines) coincide in (a), (b), and (c), whereas they satisfy $\bar{E}_1 \leq \bar{E}_2$ in (d).

are the same as above,

$$\begin{aligned}\bar{E}_D^W &= \frac{3}{16d^2}\left(\frac{1}{b_e^2}+\frac{\xi}{b_h^2}\right) \pm \frac{n_x\Delta_e}{da_e}\left[\frac{3}{2b_e}+\left(\frac{n_x\Delta_e}{a_e}\right)^2\right] \\ &\quad \mp\frac{n_x\Delta_h}{da_e\eta}\left[\frac{3}{2b_h}+\frac{1}{\xi\eta}\left(\frac{n_x\Delta_h}{a_e}\right)^2\right] \\ &\quad +\frac{1}{4d^2}\left(\frac{n_x\Delta_e}{a_e}\right)^2\left[\frac{3}{b_e}+\left(\frac{n_x\Delta_e}{a_e}\right)^2\right] \\ &\quad +\frac{1}{4\eta d^2}\left(\frac{n_x\Delta_h}{a_e}\right)^2\left[\frac{3}{b_h}+\frac{1}{\xi\eta}\left(\frac{n_x\Delta_h}{a_e}\right)^2\right], \end{aligned} \tag{3.15}$$

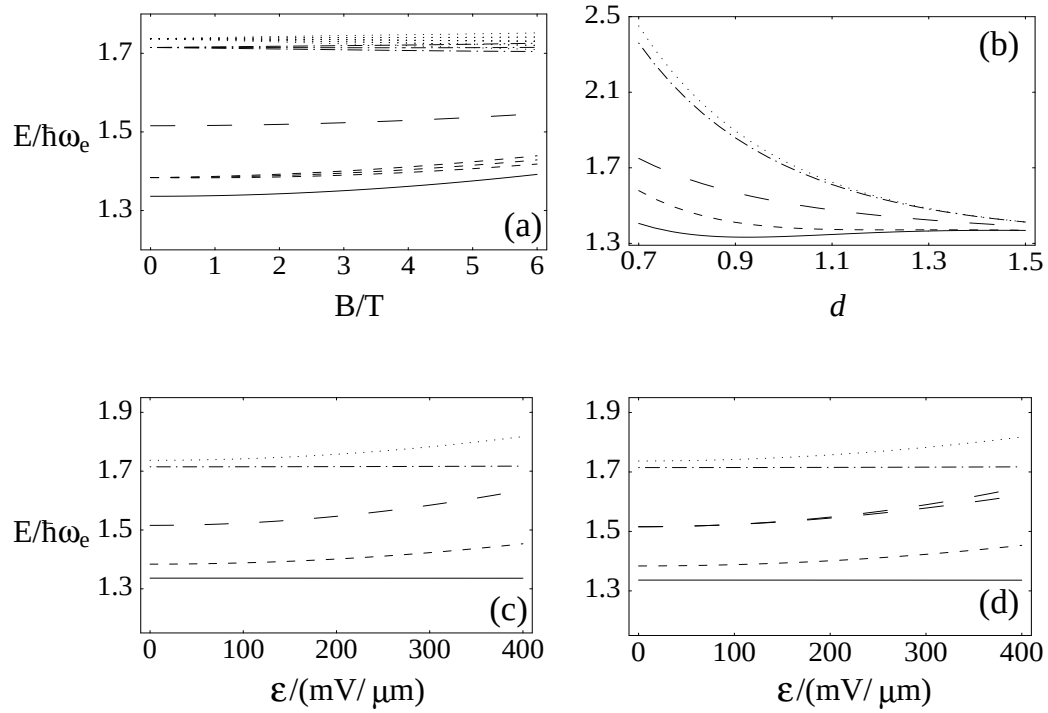

Figure 3.3: Biexciton energies in units of $\hbar\omega_e$ for InAs quantum dots as a function of (a) a magnetic field $\mathbf{B} = B\hat{\mathbf{z}}$ (including the Zeeman interaction with $|g_e| = |g_h| = 1$), (b) half the inter-dot distance $d = a/a_e$, (c) an electric field $\mathbf{E} = \varepsilon\hat{\mathbf{y}}$, (d) an electric field $\mathbf{E} = \varepsilon\hat{\mathbf{x}}$. We have set $\varepsilon = 0$ in (a) and (b), $B = 0$ in (b), (c), and (d), and $d = 1$ in (a), (c) and (d). Further, we have used effective masses for InAs quantum dots [146], $m_e = 0.05m_0$, $m_{hh} = 0.25m_0$, and $\hbar\omega_e = 33$ meV, $\eta = 1/\xi = 5$ (implying $a_e = a_h$). For these parameters, $a_e \approx 7\,\mathrm{nm}$. The plotted single-occupancy energies E_{IJ} are E_{ss} (solid line), E_{st} (short-dashed line), E_{ts} (dot-dashed line), and E_{tt} (dotted line). The exciton double-occupancy energies $\bar{E}_1$ and $\bar{E}_2$ (long-dashed lines) coincide in (a), (b), and (c), whereas they satisfy $\bar{E}_1 \leq \bar{E}_2$ in (d).

where the upper (lower) sign holds for $D = 1$ (2), and

$$\bar{E}^C = c\left(\sqrt{b_e} + \sqrt{\frac{b_h}{\xi\eta}}\right) - 4c\sqrt{\bar{b}}\,\exp\left(-\frac{\bar{b}\,\Delta^2}{4}\right) I_0\left(\frac{\bar{b}\,\Delta^2}{4}\right), \tag{3.16}$$

where $\Delta = (|\Delta_e| + |\Delta_h|)/a_e$, $\bar{b} = 2b_e b_h/(b_h + \xi\eta b_e)$, I_0 is the zeroth-order modified Bessel function, and $c = e^2\sqrt{\pi/2}\,/\kappa a_e\hbar\omega_e$ is a dimensionless parameter characterizing the strength of the Coulomb interaction.

In Figures 3.2 and 3.3 the biexciton energies E_{IJ} $(I, J = 0, 1 = s, t)$ and $\bar{E}_D$ in the double dot are shown for typical parameters for GaAs and InAs quantum dots, respectively. In both figures, the energies are shown (a) as a function of a magnetic field in the z direction, (b) as a function of half the inter-dot distance $d = a/a_e$,

(c) as a function of an electric field in the y direction, and (d) as a function of an electric field in the x direction, with all other parameters kept fixed, respectively. The Zeeman interaction H_Z is included in (a) and causes an additional level splitting of the triplet states. We assume $|g_e| = |g_h| = 1$. For GaAs dots, $|ss\rangle$ is the biexciton ground state in a large parameter regime (see Figure 3.2), whereas this is true for almost the complete regime considered for InAs dots in Figure 3.3. For magnetic fields larger than a critical field B^*, the state $|tt\rangle$ is the biexciton ground state (not shown in Figure 3.3), mainly as a result of the orbital effect of $\mathbf{B}$. Note that because of the Zeeman interaction the biexciton ground state is for $B > B^*$ an unentangled spin state (with polarized spins at temperatures which are low compared to the Zeeman splitting). We find $B^* \approx 2.7\,\mathrm{T}$ in Figure 3.2 (a). The Heitler-London ansatz is self-consistent as long as $E_{IJ}^C + E_{IJ}^W$ is smaller than the dot level spacing $\hbar\omega_\alpha$. For the parameters used in Figure 3.2, this criterion is satisfied for $2a \gtrsim 20\,\mathrm{nm}$, and we further require $k_B T < \hbar\omega_\alpha$ (i.e., $T < 20\,\mathrm{K}$) and $\epsilon < \epsilon_{\max} \approx 128\,\mathrm{mV}/\mu\mathrm{m}$ for the electric field in the x direction to avoid coupling to the first excited hole level. For Figure 3.3, $2a \gtrsim 10\,\mathrm{nm}$ is required for self-consistency and $\varepsilon < \varepsilon_{\max} \approx 470\,\mathrm{mV}/\mu\mathrm{m}$. Before discussing optical properties of the biexciton states in Section 3.4 we present in the following section results for the energies of two positively charged excitons in the double dot.

3.3 Two X^+ in a double dot

We calculate the low-lying energy spectrum of two positively charged excitons (X^+) in a double dot, following the model of Section 3.1. As discussed in Chapter 2, an additional hole suppresses the exciton fine structure splitting, and we show in Section 3.5 that the schemes for the production of entangled photons discussed in Chapter 2 can also be realized with a double dot.

Within the strong confinement regime and with lh states neglected, the ground state of a positively charged exciton in a *single* quantum dot D is given by

$$|X_\sigma^+\rangle_D = |D\rangle_e |u_{c\sigma}\rangle \otimes |DD\rangle_{h1,h2} |\chi_s\rangle_h. \tag{3.17}$$

Here, σ denotes the electron spin state and $|DD\rangle_{h1,h2} = |D\rangle_{h1}|D\rangle_{h2}$. For the heavy holes h_1 and h_2, $|\chi_s\rangle_h = (|u_{v,+3/2}\rangle|u_{v,-3/2}\rangle - |u_{v,-3/2}\rangle|u_{v,+3/2}\rangle)/\sqrt{2}$.

For simplicity, we consider holes that are localized within each quantum dot. Tunneling between v-band states is typically much weaker than for c-band states because of the larger effective mass. Tunneling of the holes is even further suppressed if the hole levels of the two dots are not of the same energy. Such misaligned hole levels are given, e.g., if two dots with different sizes are coupled. Then, the conduction-band levels can be tuned into resonance by an electric field, as discussed in Section 3.1. Typically, the hole levels are then not aligned because of the different confinement energies for electrons and holes. The overlap integral for electrons in dots with different

sizes is given by

$$S_e = \exp\left[-d^2\left(b_e\frac{3+\rho^2}{1+\rho^2}-\frac{1}{b_e}\right)\right], \tag{3.18}$$

where $\rho = a_{e2}/a_{e1}$ is the ratio of the two electron Bohr radii of the two dots[1]. For simplicity, we consider $\rho = 1$ in the following. We then apply the Heitler-London method to the conduction band electrons [72, 74] to take tunneling into account. We obtain for the two charged excitons the orbital states

$$|s\rangle = N_+\left(|12\rangle^e + |21\rangle^e\right)\otimes|11\rangle_{h1,h2}\otimes|22\rangle_{h3,h4}, \tag{3.19}$$

$$|t\rangle = N_-\left(|12\rangle^e - |21\rangle^e\right)\otimes|11\rangle_{h1,h2}\otimes|22\rangle_{h3,h4}, \tag{3.20}$$

where $N_\pm = 1/\sqrt{2\pm 2|S_e|^2}$. The corresponding electron spin singlet (s) and triplet (t) states with $t \in \{t_0, t_\uparrow, t_\downarrow\}$ are defined by Eq. (3.10). The remaining symbols are defined as in Section 3.2.

We now calculate the energies

$$E_n = \langle n|H|n\rangle = E^0 + E_n^Z + E_n^W + E_n^C \tag{3.21}$$

for $n \in \{s, t_0, t_\uparrow, t_\downarrow\}$. In units of $\hbar\omega_e$, we find

$$E_0 = 2b_e + \frac{4b_h}{\eta} - \left(\frac{\Delta_e}{a_e}\right)^2 - \frac{2}{\eta}\left(\frac{\Delta_h}{a_h}\right)^2. \tag{3.22}$$

Again, both E_n^W and E_n^C depend on the magnitude ε as well as on the direction $\mathbf{n}_\parallel$ of the electric field. For the Coulomb interaction energy $E_n^C = \langle n|H_C|n\rangle$ we obtain

$$E_n^C = \frac{E_{ee} \pm \widetilde{E}_{ee} + 4E_X + 4E_{eh} \pm 4S_e\widetilde{E}_{Xe}}{1\pm S_e^2} + 4E_{hh} + 2E_h, \tag{3.23}$$

where $E_h = E_{hh}(d=0)$ and the remaining symbols are the same as in Eq. (3.13) and are given in the Appendix A. For E_n^W, we obtain now

$$\begin{aligned} E_n^W = {} & \frac{3}{16d^2}\left(\frac{1}{b_e^2}+\frac{2\xi}{b_h^2}\right) + \frac{1}{4d^2}\left[\frac{3}{b_e}\left(\frac{n_x\Delta_e}{a_e}\right)^2 + \left(\frac{n_x\Delta_e}{a_e}\right)^4\right] \\ & + \frac{1}{4d^2}\left[\frac{6}{\eta b_h}\left(\frac{n_x\Delta_h}{a_e}\right)^2 + \frac{2}{\xi\eta^2}\left(\frac{n_x\Delta_h}{a_e}\right)^4\right] \\ & \mp \frac{3S_e^2}{4(1\pm S_e^2)}\left[\frac{1}{b_e} + d^2 + 2\left(\frac{n_x\Delta_e}{a_e}\right)^2\right]. \end{aligned} \tag{3.24}$$

[1]Further, if the two excitonic recombinations occur at different dots, the energy separation of the two photons is (in addition to the biexciton binding energy) increased by the difference of the dot confinement energies. This is useful for the subsequent separation of the optical paths of the two photons, e.g., using a cavity with a low Q-factor.

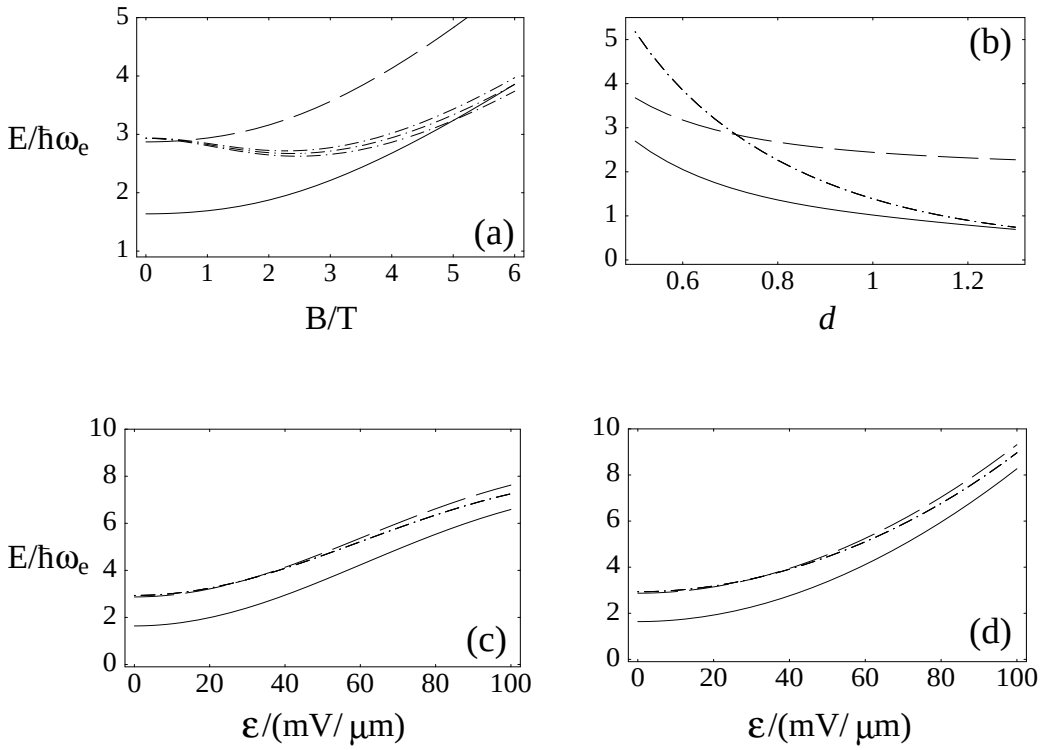

Figure 3.4: Energies of two X^+ in units of $\hbar\omega_e$ as a function of (a) a magnetic field $\mathbf{B} = B\hat{\mathbf{z}}$ for $|g_e| = 1$, (b) half the inter-dot distance $d = a/a_e$, (c) an electric field $\mathbf{E} = \varepsilon\hat{\mathbf{y}}$, (d) an electric field $\mathbf{E} = \varepsilon\hat{\mathbf{x}}$. All parameters are the same as in Figure 3.2. The plotted single-occupancy energies E_n are E_s (solid line), $E_{t\downarrow}$, E_{t0}, and $E_{t\uparrow}$ (dot-dashed lines). The energy E_D (dashed line) belongs to the state with both electrons in the same dot.

We further consider the energy E_D of the orbital states

$$|DD\rangle^e \otimes |11\rangle_{h1,h2} \otimes |22\rangle_{h3,h4}, \tag{3.25}$$

where both electrons are on the same dot D. We obtain $E_D = E^0 + E_D^W + E_D^C$, where

$$E_D^C = E_e + 4E_X + 4E_{eh} + 4E_{hh} + 2E_h, \tag{3.26}$$

$$E_D^W = \frac{3}{16d^2}\left(\frac{1}{b_e^2} + \frac{2\xi}{b_h^2}\right) + \frac{1}{4d^2}\left[\frac{3}{b_e}\left(\frac{n_x\Delta_e}{a_e}\right)^2 + \left(\frac{n_x\Delta_e}{a_e}\right)^4\right] + \frac{1}{4d^2}\left[\frac{6}{\eta b_h}\left(\frac{n_x\Delta_h}{a_e}\right)^2 + \frac{2}{\xi\eta^2}\left(\frac{n_x\Delta_h}{a_e}\right)^4\right]. \tag{3.27}$$

In Figure 3.4, the energies of two X^+ in a double dot are shown. The characteristic exchange splitting between the singlet and triplet states of the electrons are clearly visible, similar to the case with only two electrons in the dots (without holes) [72]. For large magnetic fields or large dot separations, $S_e \to 0$ and the exchange splitting between E_s and E_t vanishes, as shown in Figures 3.4 (a) and (b).

3.4 Oscillator strengths

We discuss optical properties of excitonic states in a double dot. The oscillator strength f is a measure for the coupling of exciton states to the electromagnetic field and is proportional to the optical transition rates. For an electric dipole transition between the states with $N+1$ and N excitons, $|N+1\rangle$ and $|N\rangle$, the oscillator strength is defined as

$$f_{N+1,N} = \frac{2|p_{N\mathbf{k}\lambda}|^2}{m_0\hbar\omega_{N+1,N}}, \tag{3.28}$$

where m_0 is the (bare) electron mass, $\hbar\omega_{N+1,N} = E_{N+1} - E_N$, and $p_{N\mathbf{k}\lambda} = \langle N+1|\mathbf{e}_{\mathbf{k}\lambda}\cdot\mathbf{p}|N\rangle$ is the usual matrix element of the projection of the electron momentum operator $\mathbf{p}$ on the photon polarization vector $\mathbf{e}_{\mathbf{k}\lambda}$, as introduced in Section 2.4. Explicitly,

$$p_{N\mathbf{k}\lambda} = [(N+1)!]^2 \sum_{\{\sigma_i,\tau_j\},\sigma} M_{\sigma\lambda}(\theta,\phi) \int d^3r \prod_{i,j} d^3r_i d^3s_j \times \Phi_N(\{\mathbf{r}_i,\sigma_i\};\{\mathbf{s}_j,\tau_j\})\Phi^*_{N+1}(\{\mathbf{r}_i,\sigma_i\},\mathbf{r},\sigma;\{\mathbf{s}_j,\tau_j\},\mathbf{r},\sigma\}), \tag{3.29}$$

where Φ_N is the N-exciton wavefunction, depending on the conduction-band electron (valence-band hole) coordinates $\mathbf{r}_i$ ($\mathbf{s}_j$) and their spins σ_i (τ_j) ($i,j = 1\ldots N$). The coordinate and spin of the electron and the hole created or annihilated during the optical transition are denoted by $\mathbf{r}$ and σ. Obviously, by varying the wave functions of the electron and the hole which recombine, e.g., with external magnetic and/or electric fields, the optical recombination rates are modified. The inter-band

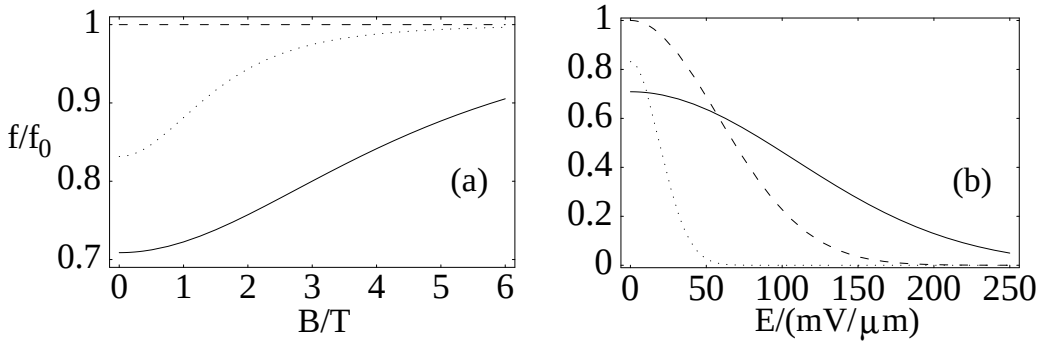

Figure 3.5: Oscillator strength $f_{X,0}$ for GaAs quantum dots in units of f_0 as a function of (a) a magnetic field B (in Tesla) at $E = 0$ and (b) an electric field E along y (in mV/μm) at $B = 0$, with $\eta = \omega_e/\omega_h = 1/2$ (solid line), $\eta = 1/\xi$ (dashed), $\eta = 4$ (dotted). For $\eta = 1/\xi$ the B field has no effect on C_{eh}.

momentum matrix element for a cubic crystal symmetry in Eq. (3.29) is given by $M_{\sigma\lambda}(\theta,\phi) = \mathbf{e}_{\mathbf{k}\lambda} \cdot \mathbf{p}_{cv}(\sigma) = p_{cv} e^{i\sigma\phi}(\cos\theta - \sigma\lambda)/2 = p_{cv} m_{\sigma\lambda}(\theta,\phi)$, where the photon emission angles θ and ϕ are defined as in Section 1.3, and $E_p = 2p_{cv}^2/m_0$ (= 25.7 eV for GaAs).

For the charged excitons discussed in Section 3.3, we obtain the same momentum matrix element Eq. (3.29) in the strong-confinement regime. For the oscillator strengths we replace in this case $\hbar\omega_{N+1,N}$ by the energy difference $\hbar\widetilde{\omega}_{N+1,N}$ of the charged excitons, which takes the Coulomb interaction energy with the additional charges into account.

For the case $N = 0$ and Fock-Darwin ground states we obtain

$$p_0 = M_{\sigma\lambda}(\theta,\phi) P_{eh}(R^2), \tag{3.30}$$

$$f_{X,0} = \frac{2|p_0|^2}{m_0 \hbar\omega_{X,0}} = \frac{E_p}{\hbar\omega_{X,0}} |m_{\sigma\lambda}(\theta,\phi)|^2 \, |P_{eh}(R^2)|^2, \tag{3.31}$$

with

$$P_{eh}(R^2) = \frac{2\sqrt{\xi\eta b_e b_h}}{b_h + \xi\eta b_e} \exp\left[-\left(b_e - \frac{\xi\eta}{b_h + \xi\eta b_e} \right) \frac{R^2}{2} \right], \tag{3.32}$$

for the integral over the envelope functions, where R is the distance (in units of a_e) between the maxima of the electron and the hole wave functions Eq. (3.7). For R there are basically three possibilities. If the electron and the hole are in the same quantum dot, $R = \Delta = (|\Delta_e| + |\Delta_h|)/a_e$. If the electron and the hole are in different dots they can still recombine due to the inter-dot overlap. There are two possibilities in this case [see Figure 3.1 (b)], either $R^2 = (2d - n_x\Delta)^2 + n_y^2\Delta^2$ or $R^2 = (2d + n_x\Delta)^2 + n_y^2\Delta^2$. For arbitrary N, the momentum matrix element $p_{N\mathbf{k}\lambda}$ contains terms of the form Eq. (3.32).

In Figure 3.5 (a) we plot $f_{X,0}/f_0$ as a function of the magnetic field, where $f_0 = E_p |m_{\sigma\lambda}(\theta,\phi)|^2/E_g$ denotes the oscillator strength for (bulk) inter-band transitions,

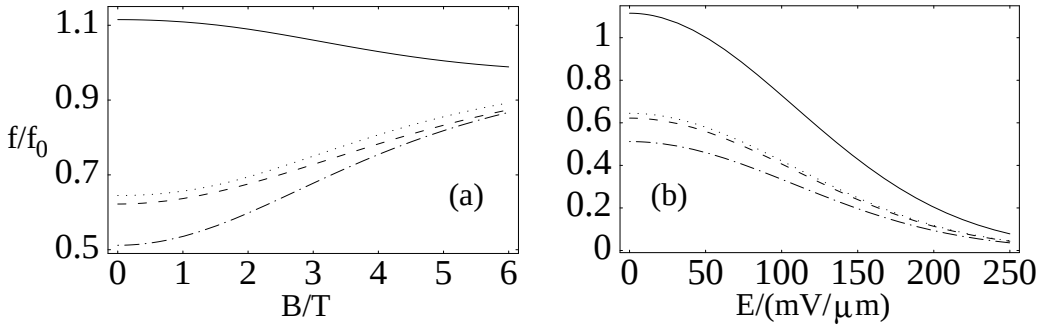

Figure 3.6: Oscillator strengths $f_{XX,X}$ for transitions between the biexciton states $|XX\rangle = |IJ\rangle$ and a single remaining exciton on one quantum dot in units of f_0 as a function of (a) a magnetic field B (in Tesla) at $E = 0$ and (b) an electric field E along y (in mV/μm) at $B = 0$. The parameters were chosen for GaAs with $\eta = \omega_e/\omega_h = 1/2$. The line styles correspond to those for E_{IJ} in Figure 3.2.

equating $\hbar\omega_{X,0}$ with the band-gap energy E_{gap}. Since we have made a strong confinement ansatz, the obtained oscillator strength is independent of the quantum dot volume V. For weak confinement, one would expect $f \propto V$. Figure 3.5 (b) shows the suppression of the exciton transition rate by an electric field. As can be seen from Eq. (3.32), excitonic recombination can be exponentially suppressed by means of an in-plane electric field which is preferably applied in the y direction to avoid inter-dot tunnelling. This enables in principle the deterministic emission of the two photons.

The momentum matrix element p_1 for transitions from an exciton state $|X\rangle$ to a biexciton state $|XX\rangle$ is given by

$$p_1 = -2|M_{\sigma\lambda}(\theta,\phi)\int d^3r_e d^3r_h d^3r \Phi_2^*(\mathbf{r}_e,\mathbf{r};\mathbf{r}_h,\mathbf{r})\Phi_1(\mathbf{r}_e,\mathbf{r}_h)|. \tag{3.33}$$

We give here the result for p_1 for a transition between the Heitler-London biexciton states $|XX\rangle = |IJ\rangle$ and a single exciton in the final state $|X\rangle = |DD\rangle$ (i.e., a single exciton in dot $D = 1, 2$) for an electric field in y direction,

$$\begin{aligned} |\langle IJ|\mathbf{e}_{\mathbf{k}\lambda}\cdot\mathbf{p}|DD\rangle| &= 2M_{\sigma\lambda}(\theta,\phi)\sqrt{N_{IJ}}\left(C_{eh}\left[(-1)^{I+J}+S_eS_h\right]\right. \\ &\quad \left.+S_{eh}\left[(-1)^J S_e+(-1)^I S_h\right]\right). \end{aligned} \tag{3.34}$$

Here, $C_{eh} = P_{eh}(\Delta^2)$ and $S_{eh} = P_{eh}(4d^2+\Delta^2)$. Approximating $\hbar\omega_{XX,X} \approx E_{\text{gap}}$, we plot the oscillator strength $f_{XX,X}$ corresponding to Eq. (3.34) versus B and E in Figures 3.6 (a) and (b). Further results for p_1, including the localized biexciton $|DDDD\rangle$ and also more exciton states are given in the Appendix B.

3.5 Production of entangled photons or entangled electrons

For the biexciton discussed in Section 3.2, we transform the Heitler-London biexciton states $|IJ\rangle$ into the picture where electrons and holes are coupled and form excitons with angular momentum projection $J_z^X = \pm 1$ (bright excitons) or $J_z^X = \pm 2$ (dark excitons). By coupling the entangled Bloch wave functions of the form Eq. (3.10a) and (3.10b) for electrons and holes, we obtain for the biexciton spin wave function

$$\begin{aligned} |IJ\rangle \;\propto\; & |{+2}\rangle|{-2}\rangle + (-1)^{I+J}|{-2}\rangle|{+2}\rangle \\ & -(-1)^{I}|{+1}\rangle|{-1}\rangle - (-1)^{J}|{-1}\rangle|{+1}\rangle. \end{aligned} \tag{3.35}$$

Here, the first ket of the two-exciton states $|\pm J_z^X\rangle|\mp J_z^X\rangle$ refers to dot $D = 1$ and the second to $D = 2$, respectively. The hh exciton states $|\pm 1\rangle$ couple to circularly polarized photon modes for emission along the spin quantization axis, as shown in Section 2.4. Note that $|ss\rangle$ and $|tt\rangle$ contain the same optically active biexciton state $|{+1}\rangle|{-1}\rangle + |{-1}\rangle|{+1}\rangle$, whereas $|st\rangle$ and $|ts\rangle$ both contain $|{+1}\rangle|{-1}\rangle - |{-1}\rangle|{+1}\rangle$. However, if for $|st\rangle$ or $|ts\rangle$ the first photon is emitted from a direct exciton (with electron and hole located in the same dot), then the second exciton remains in an antisymmetric orbital state in the double dot. Such a state does not satisfy the parity selection rule and therefore does not couple to the electromagnetic field. The states $|st\rangle$ or $|ts\rangle$ can therefore only give rise to the emission of two photons after an incoherent orbital relaxation of the second exciton. For the biexciton states $|IJ\rangle$ which contain exactly one unentangled triplet state [as Eqs. (3.10c) and (3.10d)] a superposition of states with a bright exciton in one dot and a dark exciton in the other dot is obtained. The biexciton states containing unentangled triplet states for electrons *and* holes represent product states with identical excitons in the dots. These latter two types of states do not give rise to entangled photons and are not further discussed here. In contrast, the bright exciton states in Eq. (3.35) give rise to an entangled two-photon state that is given by Eq. (2.46) in the previous chapter. If, e.g., only the electrons were delocalized in the double dot and the holes were localized, the biexciton states $|{+1}\rangle|{-1}\rangle \mp |{-1}\rangle|{+1}\rangle$ would also be obtained, namely, from the recombination of the electron singlet and triplet states, respectively. For the efficiency of this process it would be essential that the holes are unpolarized in order to enable recombination of the electrons with arbitrary spin states. This can be achieved, e.g., by excitation of the carriers within the barrier, where the hole spins relax quickly (on the order of the momentum relaxation time [99]). The localization of one carrier type (particularly the hole) is expected for double dots with weak tunnel coupling, and, e.g., also for molecularly coupled quantum dots which we consider in Chapter 5. Because of the electron-electron exchange splitting, the ground state biexciton contains in such systems $|{+1}\rangle|{-1}\rangle - |{-1}\rangle|{+1}\rangle$ rather than $|{+1}\rangle|{-1}\rangle + |{-1}\rangle|{+1}\rangle$. Here, the phase of the two-photon state indicates if electrons and holes are delocalized or, rather, only one type of carriers.

However, in typical quantum dots the exciton eigenstates are linearly polarized due to the anisotropic electron-hole exchange interaction, as discussed in Section 2.7. In the linear polarization basis $|H\rangle = (|+1\rangle - |-1\rangle)/\sqrt{2}$ and $|V\rangle = (|+1\rangle + |-1\rangle)/\sqrt{2}$, we find for the biexciton states $|ss\rangle$ and $|tt\rangle$,

$$|ss\rangle, |tt\rangle \quad \propto \quad |V\rangle|V\rangle - |H\rangle|H\rangle, \tag{3.36}$$

After emission of the first photon, the above state forms a superposition of a photon and an exciton. If the splitting δ_{ehx} between the exciton states $|H\rangle$ and $|V\rangle$ is non-zero, polarization relaxation is enhanced and contributes to polarization decoherence as discussed in Section 2.7. Further, if δ_{ehx} is larger than the exciton linewidth, the exciton and the photon are not only entangled in polarization but also in energy. Thus, the same problems as in single dots would be encountered for biexcitons in coupled asymmetric dots (which could possibly be overcome using a cavity [110]).

However, the scheme for the production of entangled photons we discussed in Chapter 2 can be adapted to the setup with two positively charged excitons in the double dot which we introduced in Section 3.3. After recombination of the first X^+, one hole is left in one dot and the second X^+ in the other dot. The electron of the X^+ will now localize in the dot with the two holes if the electron-hole binding energy E_X is larger than the energy splitting of the bonding and the antibonding single-electron state. The second photon is then with high probability produced by the recombination of the X^+. The two photons and the two holes are then in the state Eq. (2.33) and the procedures discussed in Chapter 2 can be applied to the double dot in order to achieve an entangled four-photon GHZ state Eq. (2.34) or an entangled two-photon state Eq. (2.46) from the ground state of the two X^+ which contains an electron singlet. In case the electron recombines with the single hole that has remained in the other dot, a photon is produced from a neutral exciton. This case can be distinguished from the case of recombination in the dot with two holes, since the exciton and the X^+ have different transition energies $\hbar\omega_{X,0}$ and $\hbar\widetilde{\omega}_{X,0}$, respectively. The two photons of this decay cascade are only polarization-entangled for sufficiently small δ_{ehx}, since the same restrictions apply in this situation as for the decay cascade of two neutral excitons.

Biexciton states in tunnel-coupled double dots can also be used for the production of spin-entangled electrons. After the optical creation of two electron-hole pairs in the double dot, the carriers relax into the (spin-entangled) biexciton ground state, where there is one exciton per dot, see Section 3.2. An electric field can be used to suppress the recombination of the biexciton, as we discussed in Section 3.4, and to subsequently separate electrons and holes by tunnelling into, e.g., adjacent quantum dots or separate current leads.

3.6 Conclusion

We have studied biexcitonic states in a tunnel-coupled double quantum dot [134]. As a special quality of a double dot, we find that in the (spin-entangled) biexcitonic ground state, the biexciton favors a configuration with each quantum dot occupied by one exciton, thus providing a basis for the separation of the entangled particles. The spin entanglement of the ground-state biexciton can be transferred to two photons for symmetric dots, similarly to the case of a single quantum dot [63]. The addition of two holes to the double dot enables the generation of entangled four-photon states after injection of an electron pair, as in the case discussed in Chapter 2 for two uncoupled dots. Analogously, full bipartite photon entanglement can also be obtained in the double dot setup for the first two photons after a linear polarization measurement of the third and the fourth photon as described in Section 2.9, even for asymmetric quantum dots with a non-vanishing exciton fine structure splitting.

Chapter 4

Optical detection of single-electron spin decoherence in a quantum dot

We propose and theoretically analyze several methods to optically measure the decoherence time T_2 of a single electron spin in a quantum dot [150, 151]. In Section 4.1 we give a motivation for T_2-measurements. We then discuss the optical detection of single-electron spin resonance in Section 4.2 in the framework of a generalized master equation. The detection of the photocurrent is discussed as an alternative possibility for the readout. We then study alternative schemes to optically measure T_2 in the remaining sections. In Section 4.3 a setup is considered enabling the observation of spin Rabi-oscillations in the luminescence intensity autocorrelation function and also a measurement of the single-spin relaxation time T_1. In Section 4.4 the detection of spin Rabi-oscillations in the photoluminescence is discussed, and we show in Section 4.5 that a similar scheme is possible to detect spin precession. We conclude the chapter in Section 4.6.

4.1 Electron spin coherence in quantum dots

As already mentioned in Section 1.1, the spin 1/2 states $|\uparrow\rangle$ and $|\downarrow\rangle$ of an electron in a semiconductor quantum dot can be used as an implementation of a qubit. Single-spin relaxation times T_1 have been reported to be on the order of milliseconds in quantum dots (see Section 1.1). To our current knowledge, there are only very few results published on measurements of the T_2 time of single electron spins in quantum dots. The dominant mechanisms for electron spin decoherence in quantum dots have been identified to be the coupling to phonons via the spin-orbit interaction and the contact hyperfine interaction with the nuclei of the quantum dot [10]. For the coupling to phonons in leading order of the Rashba and Dresselhaus spin-orbit coupling terms,

$T_2 = 2T_1$ has been obtained [152]. It therefore seems that the hyperfine interaction imposes the stricter limitation on electron spin coherence in GaAs or InAs dots, unless the nuclear spins are highly polarized. The contact hyperfine interaction even exhibits non-Markovian dynamics, leading to power-law decay rather than exponential decay of spin coherence [153, 154, 155].

For optical experiments, the interaction of the electron and the hole of the exciton usually imposes a principal difficulty: The electron spin and the hole spin are only decoupled if the hole spin couples stronger to the environment than to the electron spin. However, time-resolved Faraday rotation[1] experiments suggest that there is significant coupling of electron and hole spins in quantum dots [22]. Still, the decoherence time of exciton spins might provide a lower bound on T_2. In many other experiments, electron-hole pairs are excited inside the barrier material of a quantum dot heterostructure. After their creation, the carriers diffuse into the dots within typically tens of picoseconds [93, 94]. Due to the fast relaxation time of the hole spin in the barrier, electron and hole spins decouple during this time. One would thus expect that in such a setup only the spin decoherence of electrons can be measured, e.g., by the Hanle effect. This approach has given the result $g_e T_2^* \approx 210\,\mathrm{ps}$ for an ensemble of InAs self-assembled dots at $T = 6\,\mathrm{K}$ [23], where g_e is the electron g-factor. In contrast to the single-spin decoherence time T_2, the ensemble dephasing time $T_2^* \leq T_2$ might be reduced from $T_2^* = T_2$ by dephasing among the spins of the measured ensemble. It might thus be possible that the coherence of single electron spins is larger than the values obtained from these experiments. In fact, recent Hanle measurements on individual quantum dots [25] have indicated an electron decoherence time $T_2 \approx 16\,\mathrm{ns}$. Yet, this result may have slightly exceeded the expected value $T_2 \approx \hbar\sqrt{N}/A$, where N is the number of nuclei in the dot and A the hyperfine coupling constant (see also Ref. [10] for a further discussion).

Alternatively, T_2 can be measured via currents through quantum dots where ESR is induced [156, 157, 158]. However, this requires contacting of the dots with current leads which reduces coherence, while with an optical detection scheme one can also benefit from the high sensitivity of photodetectors.

4.2 Optical detection of single-electron spin resonance

Optical detection of magnetic resonance (ODMR) is a double resonance technique where transitions between spin sublevels are detected via optical transitions. If only one of the spin sublevels is coupled to an optical transition, then the optical dynamics depends conditionally on the spin dynamics, enabling, for example, the study of spin coherence [159, 160, 161, 162, 163] or of g-factor anisotropy [164, 165]. ODMR has

[1] See Section 5.2 for a discussion of Faraday rotation.

already been applied to measure the coherence of *single* spins in various systems, including single molecules [160, 161] and single nitrogen-vacancy centers in diamond [162, 163]. Recent ODMR experiments on charge-neutral semiconductor quantum dots [164, 165] have demonstrated the feasibility of the combination of ESR and optical methods in quantum dot experiments, but have not considered single-spin coherence.

We assume that a quantum dot is charged with one single electron. This can be achieved experimentally, e.g., by n-doping [166], or by electrical injection if the dot is embedded inside a photodiode structure [167, 168, 19]. The single-electron state of the dot can be optically excited, creating a negatively charged exciton (X^-) which consists of two electrons and one hole. In the X^- ground state, the two electrons form a spin singlet in the lowest (conduction-band) electron level and the hole occupies the lowest (valence-band) hole level, as shown in recent experiments with InAs dots [104, 105] and GaAs dots [169]. Such negatively charged excitons can be used to read out and initialize a single electron spin [170]. We assume that the lowest heavy hole (hh) dot level (with total angular momentum projection $J_z = \pm 3/2$) and the lowest light hole (lh) dot level (with $J_z = \pm 1/2$) are split by an energy $\Delta_{\mathrm{hh-lh}}$ and that mixing of hh and lh states is negligible. These conditions are satisfied for several types of quantum dots [104, 105, 169, 170, 171, 172]. Then, if excitation is restricted to either hh or lh states, the circularly polarized optical transitions σ^+ and σ^- are unambigously related to one spin polarization of the conduction-band electron because of optical selection rules, see also Figure 4.1. Here, we assume a hh ground state for holes.

For the proposed ODMR scheme, we consider the following dot states (see also Figure 4.1). In the presence of an external static magnetic field, a single electron in the lowest orbital state can be in the spin ground state $|\uparrow\rangle$ or in the excited spin state $|\downarrow\rangle$. Similarly, an X^- in the orbital ground state can either be in the excited spin state $|X^-_\downarrow\rangle$ or in the spin ground state $|X^-_\uparrow\rangle$, where the subscripts $\downarrow$ and $\uparrow$ refer to the hh spin. In contrast to the other chapters we apply the time-inverted notation for hole spins, here. For simplicity, we have assumed equal signs for the electron and the hh g factors in z direction. Here, we exclude X^- states where one electron is in an excited orbital state. The lowest X^- state of this type contains an electron triplet and requires an additional energy $\delta\epsilon \approx 40$ meV in InAs dots [166]. This energy difference $\delta\epsilon$ is mainly given by the single-electron level spacing (≈ 50 meV [173]) and the electron-electron exchange interaction. Consequently, the state $|X^-_\downarrow\rangle$ can be excited resonantly by a circularly polarized laser with a bandwidth lower than $\delta\epsilon$ and $\Delta_{\mathrm{hh-lh}}$. An ODMR scheme including an X^- state with an excited hole is also possible, as we discuss in Section 4.2.3.

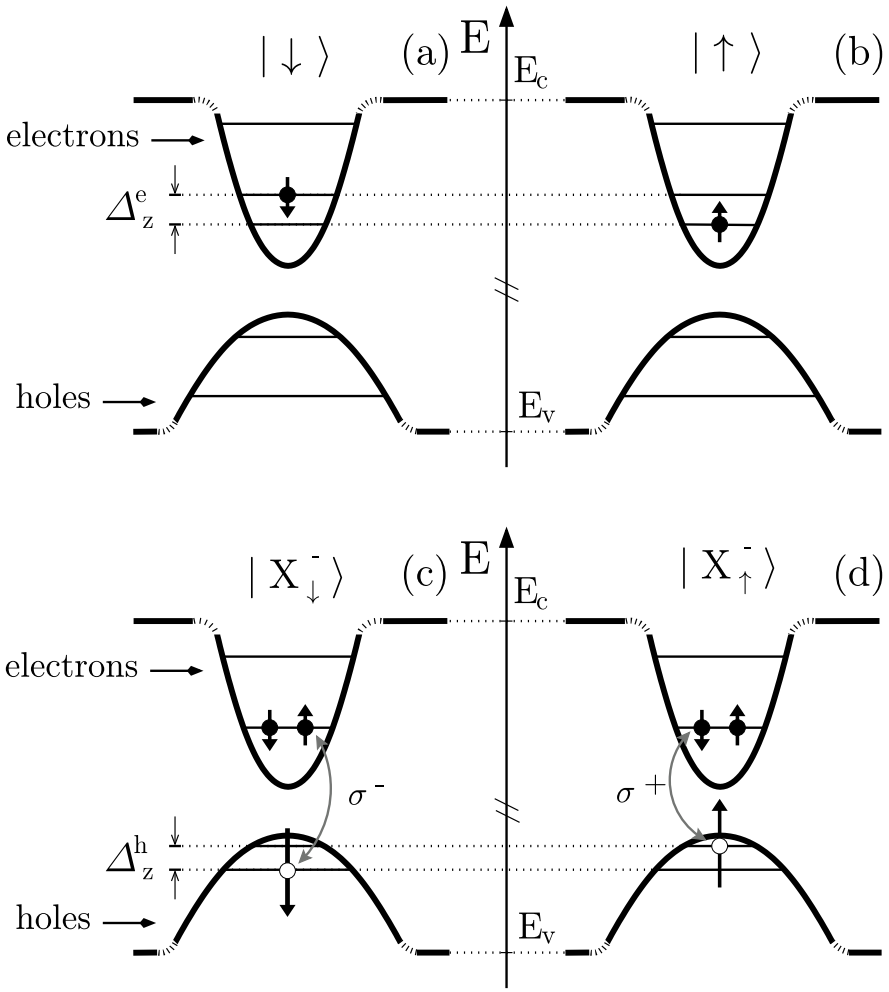

Figure 4.1: (a)-(d): The states of a single quantum dot in a static magnetic field. The Zeeman splittings are $\Delta_z^e = g_e^z \mu_B B_z$ for the electron and $\Delta_z^h = g_{hh}^z \mu_B B_z$ for the hole. Coherent transitions occur between (a) and (b) due to ESR and between (a) and (c) due to a σ^--polarized laser field. The grey arrows in (c) and (d) indicate which electron-hole pair couples with the photon field of polarization $\sigma^\pm$.

4.2.1 Hamiltonian

In an ODMR setup with a quantum dot containing a single excess electron, we describe the energy-conserving dynamics with the Hamiltonian

$$H = H_{\mathrm{dot}} + H_{\mathrm{ESR}} + H_{\mathrm{L}} + H_{\mathrm{d-L}}, \tag{4.1}$$

which couples the three states $|\uparrow\rangle$, $|\downarrow\rangle$, and $|X_{\downarrow}^{-}\rangle$.

Here, H_{dot} contains the quantum dot potential, the Zeeman energies due to a constant magnetic field B_z in the z direction, and the Coulomb interaction of electrons and holes. The dot energy E_n is defined by $H_{\mathrm{dot}}|n\rangle = E_n|n\rangle$. We set $\hbar = 1$ in the following. The electron Zeeman splitting is $\Delta_z^e = g_e^z \mu_{\mathrm{B}} B_z = E_{\downarrow} - E_{\uparrow}$, where g_e^z is the electron g factor and μ_{B} is the Bohr magneton. In B_z, we also include the Overhauser field which could possibly arise from dynamically polarized nuclear spins.

The ESR term $H_{\mathrm{ESR}}(t)$ couples the two electron Zeeman levels $|\uparrow\rangle$ and $|\downarrow\rangle$ via a magnetic dipole transition (see Section 2.4.2), induced by the magnetic field $\mathbf{B}_{\perp}(t)$, which rotates with frequency ω_{ESR} in the xy plane. Note that a linearly oscillating magnetic field, $\mathbf{B}_x(t) = B_x^0 \cos(\omega_{\mathrm{ESR}} t)\hat{\mathbf{x}}$, can be applied instead of $\mathbf{B}_{\perp}(t)$ [98]. The linearly oscillating field can be decomposed in a clockwise and a counterclockwise rotating component. In the rotating wave approximation this field leads to the same result as the rotating field with $B_{\perp} \to B_x^0/2$. The ESR Rabi frequency is $\Omega_{\mathrm{ESR}} = g_e^{\perp} \mu_{\mathrm{B}} B_{\perp}$, with in-plane g factor $g_e^{\perp}$ (typically, $g_e^{\perp} = g_e^z$). Even if the frequency ω_{ESR} is also resonant with the hole Zeeman splitting, the Rabi oscillations of the holes have a negligible effect since the charged exciton states recombine quickly. As an alternative to a radio-frequency (rf) field $\mathbf{B}_{\perp}(t)$, an oscillating field $\mu_{\mathrm{B}}\mathbf{gB}$ could also be produced using voltage-controlled modulation of the electron g-tensor $\mathbf{g}$, which has already been achieved experimentally in quantum wells [174].

A σ^--polarized laser of frequency ω_{L} is applied in z direction (typically parallel to [001]), with the free laser field Hamiltonian $H_{\mathrm{L}} = \omega_{\mathrm{L}} a_{\mathrm{L}}^{\dagger} a_{\mathrm{L}}$, where $a_{\mathrm{L}}^{(\dagger)}$are photon operators. The optical interaction term $H_{\mathrm{d-L}}$ describes the coupling of $|\downarrow\rangle$ and $|X_{\downarrow}^{-}\rangle$ to the laser field with the complex optical Rabi frequency $\Omega_{\mathrm{L}} = \alpha e \langle X_{\downarrow}^{-}|\mathbf{e}_{\mathrm{L}} \cdot \mathbf{p}|\downarrow\rangle \sqrt{\hbar/2m_0^2 c^2 V \epsilon_0 \epsilon_r \omega_{\mathrm{L}}}$, where V, ω_{L}, and $\mathbf{e}_{\mathrm{L}} = (1, -i, 0)/\sqrt{2}$ are the volume, the frequency and the unit polarization vector of the left-circularly polarized laser mode, respectively, and $|\alpha|^2$ is the mean number of photons present in the coherent state $|\alpha\rangle$ of the laser, see Section 2.4.1. The relative permittivity of the semiconductor is ϵ_r, and ϵ_0 is the dielectric constant. Because the laser is circularly polarized, the terms that violate energy conservation vanish due to selection rules. Further, the absorption of a σ^- photon in the spin ground state $|\uparrow\rangle$ is excluded due to Pauli blocking because we assume that the laser bandwidth is smaller than $\Delta_{\mathrm{hh-lh}}$ and $\delta\epsilon$, as discussed in Section 4.2. Note that the very same scheme can also be applied if the sign of the hole g factor is reversed, since a σ^+ laser field can then be used and all results apply after interchanging $|X_{\downarrow}^{-}\rangle$ and $|X_{\uparrow}^{-}\rangle$. The laser bandwidth and also the temperature can safely exceed the electron Zeeman splitting. Finally, we exclude all

multi-photon processes via other levels since they are only relevant to high-intensity laser fields. In this configuration, the σ^- photon absorption is switched "on" and "off" by the electron spin flips driven by the ESR. As an important experimental step towards this direction, spin-dependent absorption as described above has recently been demonstrated in a high-resolution absorption spectroscopy setup with a single InGaAs/GaAs quantum dot charged with a single electron [125].

We next set the energy scale zero at $(E_{X\downarrow} - E_\downarrow)/2$ and transform H into the frame rotating with respect to the field frequencies $\omega_{\rm ESR}$ and $\omega_{\rm L}$,

$$H' = U^\dagger H U - iU^\dagger \frac{\partial U}{\partial t}, \tag{4.2}$$

with the unitary operator

$$U = \exp\left\{-i\omega_{\rm L} t\left[a_{\rm L}^\dagger a_{\rm L} + \frac{1}{2}\left(|X_\downarrow^-\rangle\langle X_\downarrow^-| - |\downarrow\rangle\langle\downarrow|\right)\right] + it\left(\frac{\omega_{\rm L}}{2} + \omega_{\rm ESR}\right)|\uparrow\rangle\langle\uparrow|\right\}. \tag{4.3}$$

We introduce the laser detuning $\delta_{\rm L} = (E_{X\downarrow} - E_\downarrow) - \omega_{\rm L}$ and the ESR detuning $\delta_{\rm ESR} = g_e^z \mu_{\rm B} B_z - \omega_{\rm ESR}$ and obtain

$$\begin{aligned} H' \;=\; & \frac{\delta_{\rm L}}{2}|X_\downarrow^-\rangle\langle X_\downarrow^-| - \frac{\delta_{\rm L}}{2}|\downarrow\rangle\langle\downarrow| - \left(\frac{\delta_{\rm L}}{2} + \delta_{\rm ESR}\right)|\uparrow\rangle\langle\uparrow| \\ & + \frac{1}{2}\left(\Omega_{\rm L}|X_\downarrow^-\rangle\langle\downarrow| + \Omega_{\rm L}^*|\downarrow\rangle\langle X_\downarrow^-|\right) + \frac{1}{2}\Omega_{\rm ESR}\left(|\uparrow\rangle\langle\downarrow| + |\downarrow\rangle\langle\uparrow|\right). \end{aligned} \tag{4.4}$$

4.2.2 Generalized master equation

For the dot dynamics including relaxation and decoherence processes, we consider the reduced density matrix for the dot, $\rho = {\rm Tr}_{\rm R}\,\rho_{\rm F}$. Here, $\rho_{\rm F}$ is the full density matrix of the dot and its environment (or reservoir), i.e., the unobserved degrees of freedom, and ${\rm Tr}_{\rm R}$ is the trace taken over the reservoir. We take the interaction of the dot states with the rf field and the laser field exactly into account using the Hamiltonian Eq. (4.4) in the rotating frame. With a generalized master equation in the Lindblad form [175, 176],

$$\dot\rho = -i[H', \rho] + \mathcal{L}\rho, \tag{4.5}$$

we further take the coupling with the environment (radiation field, nuclear spins, phonons, spin-orbit interaction, etc.) into account with the Liouvillian superoperator $\mathcal{L}$ which introduces phenomenological rates. We use the rates $W_{nm} \equiv W_{n\leftarrow m}$ for the incoherent transitions from state $|m\rangle$ to $|n\rangle$ and the rates V_{nm} for the decay of the corresponding off-diagonal matrix elements of ρ. These decoherence rates V_{nm} have the structure $V_{nm} = \frac{1}{2}\sum_k (W_{kn} + W_{km}) + V_n + V_m$, where the rate $V_n + V_m$ is usually called the pure decoherence rate. Further, the electron spin relaxation time is $T_1 = (W_{\uparrow\downarrow} + W_{\downarrow\uparrow})^{-1}$, with spin flip rates $W_{\uparrow\downarrow}, W_{\downarrow\uparrow}$. (In Section 4.3 below, we point out a

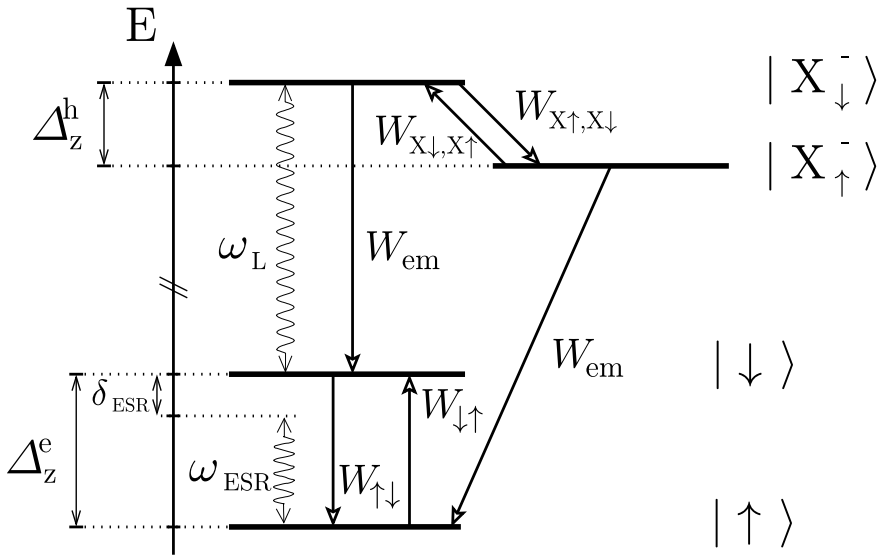

Figure 4.2: Level scheme of the four states shown in Figure 4.1. Wavy arrows describe the transitions driven by the rf field and the laser field with frequencies $\omega_{\rm ESR}$ and $\omega_{\rm L}$, respectively. The corresponding Rabi frequencies are $\Omega_{\rm ESR}$ and $|\Omega_{\rm L}|$. A detuning $\delta_{\rm ESR} = \Delta_z^e - \omega_{\rm ESR}$ is shown for the rf field, with Zeeman splitting Δ_z^e. Incoherent transitions are shown with arrows and occur at rates W_{nm}. We consider $W_{\downarrow,X\downarrow} = W_{\uparrow,X\uparrow} =: W_{\rm em}$.

method to measure T_1 in a similar setup as discussed here.) In the absence of the ESR field and the laser field, the off-diagonal matrix elements of the electron spin decay with the (intrinsic) single-spin decoherence rate $V_{\downarrow\uparrow} = \frac{1}{2}(W_{\uparrow\downarrow}+W_{\downarrow\uparrow})+V_\uparrow+V_\downarrow = 1/T_2$. Further, the linewidth of the optical σ^- transition is denoted by $V_{\rm X} = V_{X\downarrow,\downarrow}$. We use the notation $\rho_n = \langle n|\rho|n\rangle$ and $\rho_{n,m} = \langle n|\rho|m\rangle$ for the matrix elements of ρ. In the rotated basis $|\uparrow\rangle$, $|\downarrow\rangle$, $|X_\uparrow^-\rangle$, $|X_\downarrow^-\rangle$, the generalized master equation is given by $\dot\rho = \mathcal{M}\rho$, where $\mathcal{M}$ is a superoperator. Explicitly,

$$\dot\rho_\uparrow = \Omega_{\rm ESR}{\rm Im}\rho_{\downarrow,\uparrow} + W_{\rm em}\rho_{X\uparrow} + W_{\uparrow\downarrow}\rho_\downarrow - W_{\downarrow\uparrow}\rho_\uparrow, \tag{4.6}$$

$$\dot\rho_\downarrow = -\Omega_{\rm ESR}{\rm Im}\rho_{\downarrow,\uparrow} + {\rm Im}(\Omega_{\rm L}^*\,\rho_{X\downarrow,\downarrow}) + W_{\rm em}\,\rho_{X\downarrow} + W_{\downarrow\uparrow}\,\rho_\uparrow - W_{\uparrow\downarrow}\,\rho_\downarrow, \tag{4.7}$$

$$\dot\rho_{X\downarrow} = -{\rm Im}(\Omega_{\rm L}^*\,\rho_{X\downarrow,\downarrow}) + W_{X\downarrow,X\uparrow}\,\rho_{X\uparrow} - (W_{\rm em}+W_{X\uparrow,X\downarrow})\,\rho_{X\downarrow}, \tag{4.8}$$

$$\dot\rho_{X\uparrow} = W_{X\uparrow,X\downarrow}\,\rho_{X\downarrow} - (W_{\rm em}+W_{X\downarrow,X\uparrow})\,\rho_{X\uparrow}, \tag{4.9}$$

$$\dot\rho_{\downarrow,\uparrow} = \frac{i}{2}\Omega_{\rm ESR}\,(\rho_\downarrow-\rho_\uparrow) - \frac{i}{2}\Omega_{\rm L}^*\rho_{X\downarrow,\uparrow} - \left(i\delta_{\rm ESR}+T_2^{-1}\right)\,\rho_{\downarrow,\uparrow}, \tag{4.10}$$

$$\dot\rho_{X\downarrow,\uparrow} = \frac{i}{2}\Omega_{\rm ESR}\,\rho_{X\downarrow,\downarrow} - \frac{i}{2}\Omega_{\rm L}\rho_{\downarrow,\uparrow} - [i(\delta_{\rm ESR}+\delta_{\rm L})+V_{X\downarrow,\uparrow}]\,\rho_{X\downarrow,\uparrow}, \tag{4.11}$$

$$\dot\rho_{X\downarrow,\downarrow} = \frac{i}{2}\Omega_{\rm ESR}\rho_{X\downarrow,\uparrow} - \frac{i}{2}\Omega_{\rm L}(\rho_\downarrow-\rho_{X\downarrow}) - (i\delta_{\rm L}+V_{\rm X})\rho_{X\downarrow,\downarrow}. \tag{4.12}$$

The remaining (off-diagonal) matrix elements of ρ are decoupled from these equations and are not further important here.

4.2.3 ESR linewidth in the photoluminescence

We now calculate the stationary photoluminescence for a cw ESR field and a cw laser field. For this, we evaluate the stationary density matrix $\bar{\rho}$, which satisfies $\dot{\bar{\rho}} = 0$. We introduce the effective rate

$$W_{\mathrm{L}} = \frac{|\Omega_{\mathrm{L}}|^2}{2} \frac{V_{\mathrm{X}}}{V_{\mathrm{X}}^2 + \delta_{\mathrm{L}}^2} \tag{4.13}$$

for the optical excitation, which takes its maximum value $W_{\mathrm{L}}^{\max}$ for $\delta_{\mathrm{L}} = 0$. We first solve $\dot{\bar{\rho}}_{X\downarrow,\uparrow} = 0$. We find that the coupling to the laser field produces an additional decoherence channel to the electron spin. We thus obtain a renormalized spin decoherence rate V_{ESR}, which satisfies

$$V_{\mathrm{ESR}} \leq \frac{1}{T_2} + \frac{|\Omega_{\mathrm{L}}|^2}{4V_{X\downarrow,\uparrow}} \approx \frac{1}{T_2} + \frac{1}{2} W_{\mathrm{L}}^{\max}. \tag{4.14}$$

Similarly, the ESR detuning δ_{ESR} is also renormalized,

$$\tilde{\delta}_{\mathrm{ESR}} \geq \delta_{\mathrm{ESR}} \left[1 - \frac{|\Omega_{\mathrm{L}}|^2}{(W_{\mathrm{em}} + W_{X\uparrow,X\downarrow})^2} \right]. \tag{4.15}$$

We assume that these renormalizations and δ_{L} are small compared to the optical linewidth V_{X}, i.e., $W_{\mathrm{L}}^{\max}$, $|\tilde{\delta}_{\mathrm{ESR}} - \delta_{\mathrm{ESR}}| < V_{\mathrm{X}}$. Further, if both transitions are near resonance, $\delta_{\mathrm{L}} \lesssim V_{\mathrm{X}}$ and $|\tilde{\delta}_{\mathrm{ESR}}| \lesssim V_{\mathrm{ESR}}$, no additional terms appear in the renormalized master equation. We then solve $\dot{\bar{\rho}}_{X\downarrow,\downarrow} = 0$ and $\dot{\bar{\rho}}_{\downarrow,\uparrow} = 0$ and introduce the effective Rabi spin-flip rate

$$W_{\mathrm{ESR}} = \frac{\Omega_{\mathrm{ESR}}^2}{2} \frac{V_{\mathrm{ESR}}}{V_{\mathrm{ESR}}^2 + \tilde{\delta}_{\mathrm{ESR}}^2}, \tag{4.16}$$

which together with W_{L} eliminates the parameters Ω_{L}, V_{X}, δ_{L}, Ω_{ESR}, V_{ESR}, and $\tilde{\delta}_{\mathrm{ESR}}$ in the remaining equations for the diagonal elements of ρ. Further, these now contain the total spin flip rates $\tilde{W}_{\uparrow\downarrow} = W_{\uparrow\downarrow} + W_{\mathrm{ESR}}$ and $\tilde{W}_{\downarrow\uparrow} = W_{\downarrow\uparrow} + W_{\mathrm{ESR}}$. We obtain the stationary solution

$$\begin{aligned}
\bar{\rho}_{\uparrow} &= \eta W_{\mathrm{L}} W_{\mathrm{em}} W_{X\uparrow,X\downarrow} + \eta \tilde{W}_{\uparrow\downarrow} W_{\mathrm{em}} W_{X\uparrow,X\downarrow} \\
&\quad + \eta \tilde{W}_{\uparrow\downarrow} (W_{\mathrm{L}} + W_{\mathrm{em}}) (W_{\mathrm{em}} + W_{X\downarrow,X\uparrow}), && (4.17) \\
\bar{\rho}_{\downarrow} &= \eta \tilde{W}_{\downarrow\uparrow} (W_{\mathrm{L}} + W_{\mathrm{em}}) (W_{\mathrm{em}} + W_{X\downarrow,X\uparrow}) + \eta \tilde{W}_{\downarrow\uparrow} W_{\mathrm{em}} W_{X\uparrow,X\downarrow}, && (4.18) \\
\bar{\rho}_{X\downarrow} &= \eta W_{\mathrm{L}} \tilde{W}_{\downarrow\uparrow} (W_{\mathrm{em}} + W_{X\downarrow,X\uparrow}), && (4.19) \\
\bar{\rho}_{X\uparrow} &= \eta W_{\mathrm{L}} \tilde{W}_{\downarrow\uparrow} W_{X\uparrow,X\downarrow}, && (4.20)
\end{aligned}$$

where the normalization factor η is chosen such that $\sum_n \rho_n = 1$. Comparing the expressions for $\bar{\rho}_{\uparrow}$ and $\bar{\rho}_{\downarrow}$ above, we see that $\bar{\rho}_{\uparrow} \geq \bar{\rho}_{\downarrow}$ is satisfied for $W_{\uparrow\downarrow} \geq W_{\downarrow\uparrow}$. This electron spin polarization is due to the hole spin relaxation channel, analogous as in an optical pumping scheme. A hole spin flip corresponds to leakage out of the states

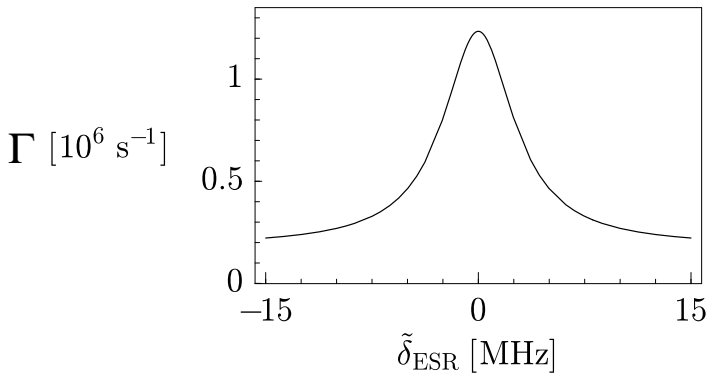

Figure 4.3: The stationary photoluminescence rate Γ as a function of the ESR detuning $\tilde{\delta}_{\rm ESR}$. As described in the text, Γ is a Lorentzian and its linewidth w gives an upper bound for $2/T_2$. Here, we use $g_e = 0.5$, $B_\perp = 1$G, $T_2 = 100$ns, $W_{\uparrow\downarrow} = W_{\downarrow\uparrow} = (20\mu{\rm s})^{-1}$, $W_{\rm em} = 10^9 {\rm s}^{-1}$, $W_{X\uparrow,X\downarrow} = W_{X\downarrow,X\uparrow} = W_{\rm em}/2$, $\delta_{\rm L} = 0$, $V_{X\downarrow,\uparrow} = V_{\rm X} = (W_{\rm em} + W_{X\uparrow,X\downarrow})/2$, and $\Omega_{\rm L} = 2\Omega_{\rm ESR}\sqrt{T_2 V_{\rm X}}$. With these parameters, $W_{\rm L} \lesssim T_2^{-1} \lesssim V_{\rm ESR}$ is satisfied.

that are driven by the external fields. Since the dynamics due to the ESR is much slower than the optical recombination, there is an increased population of the state $|\uparrow\rangle$.

The stationary photoluminescence $\Gamma = \Gamma^- + \Gamma^+$ consists of a σ^-- and a σ^+- polarized contribution, $\Gamma^- = W_{\rm em}\bar{\rho}_{X\downarrow}$ and $\Gamma^+ = W_{\rm em}\bar{\rho}_{X\uparrow}$, respectively. We find that the rates Γ^- and Γ^+ are proportional to $W_{\rm ESR}/(\gamma + W_{\rm ESR})$ for a given γ, up to a constant background which is negligible for $W_{\downarrow\uparrow} < W_{\rm ESR}$. In particular, the total emission rate $\Gamma = \Gamma^- + \Gamma^+$ as a function of $\tilde{\delta}_{\rm ESR}$ is a Lorentzian with linewidth

$$w = 2\,V_{\rm ESR}\sqrt{1 + \frac{W_{\rm ESR}^{\rm max}}{\gamma}}, \tag{4.21}$$

see also Figure 4.3. By analyzing the expression for γ, we find the relevant parameter regime with the inequality

$$\begin{aligned} w \;\leq\; & 2V_{\rm ESR}\Bigg[1 + \frac{2W_{\rm ESR}^{\rm max}}{W_{\rm L}}\left(1 + \frac{W_{\rm em}}{W_{\rm r}} + \frac{W_{X\downarrow,X\uparrow}}{W_{\rm r}}\right) \\ & + \frac{3W_{\rm ESR}^{\rm max}}{W_{\rm r}} + \frac{W_{\rm ESR}^{\rm max}}{W_{\rm em}}\left(1 + \frac{3\,W_{X\downarrow,X\uparrow}}{W_{\rm r}}\right)\Bigg]^{1/2}, \end{aligned} \tag{4.22}$$

which saturates for vanishing spin flip rates $W_{\downarrow\uparrow}$ and $W_{\uparrow\downarrow}$. Here, we have introduced the rate $W_{\rm r} = W_{X\uparrow,X\downarrow} + W_{\uparrow\downarrow}\,(1 + W_{\rm em}/W_{\rm L})$ which describes different relaxation channels that lead to the ground state $|\uparrow\rangle$. These correspond to "switching off" the laser excitations because of Pauli blocking. The linewidth w thus provides a *lower bound* for T_2:

$$T_2 \geq V_{\rm ESR}^{-1} \geq \frac{2}{w}. \tag{4.23}$$

Here, the second inequality saturates when the expression in brackets in Eq. (4.22) becomes close to 1 (e.g., for efficient hole spin relaxation [184, 185] W_r is large and $w \approx 2\,V_\mathrm{ESR}$). For the first inequality, $T_2 \approx V_\mathrm{ESR}^{-1}$ for $W_\mathrm{L}^\mathrm{max} < 1/T_2$, see Eq. (4.14). To check our analytical approximation for Γ, we have solved the generalized master equation numerically using the parameters given in the caption of Figure 4.3. Comparing the two results for Γ, we find that the relative difference is less than 0.2 %.

Due to possible experimental imperfections in the ODMR scheme described above, e.g., due to mixing of hh and lh states or due to a small contribution of the σ^+ polarization in the laser light, there can be a small probability that the Pauli blocking of absorption is somewhat lifted and the state $|\uparrow\rangle$ can be optically excited. We describe this process with the effective rate $W_{\mathrm{L},\uparrow}$. It leads to an additional linewidth broadening, similar to the one described with Eq. (4.22). We find that this effect is small if $W_{\mathrm{L},\uparrow} < W_\mathrm{ESR}$.

The setup discussed in this section combines optical excitation and detection at the same wavelength. The laser stray light is an undesirable background here and its detection can be avoided, e.g., by using a polarization filter and by measuring only Γ^+. The laser could also be distinguished from Γ^- if two-photon excitation is applied, which is, e.g., possible with excitons in II-VI (e.g., CdSe [177] or CdS [178]) and I-VII (e.g., CuCl [179]) semiconductor nanocrystals. As another alternative, the optical excitation could be tuned to an excited hole state (hh or lh) [180], possibly with a reversal of laser polarization. Using a *pulsed* laser would enable the distinction between luminescence and laser light by time-gated detection. See also Section 4.4 for another detection scheme with a pulsed laser. Another option is to detect the resonant absorption instead of the photoluminescence, using an optical transmission setup [106, 125]. Finally, one can also measure the photocurrent [181, 182, 62] instead of the photoluminescence, which we discuss in the following subsection.

4.2.4 Readout via photocurrent

As an alternative to photon detection, the presence of a charged exciton X^- in the dot can also be read out via an electric current (the so-called photocurrent) [181, 182, 62]. Here, an electric field is applied across the quantum dot such that one electron and one hole tunnel out of the dot into two adjacent current leads. Thus, the total charge e is transported through the dot per optical excitation, where e is the elementary charge. Because the tunneling process is spin-independent, the remaining electron on the dot has equal probabilities to be in state $|\uparrow\rangle$ or in state $|\downarrow\rangle$, in contrast to the readout using photoluminescence. We now calculate the stationary photocurrent. For this, we apply a generalized master equation description, similarly as in Section 4.2.2 for the photoluminescence. We introduce phenomenological photocurrent rates W_pc as shown in Figure 4.4. For strong tunneling ($W_\mathrm{pc} > W_\mathrm{em}$), optical recombination is negligible and the X^- are predominantly detected via the photocurrent. The generalized master equation is then given by

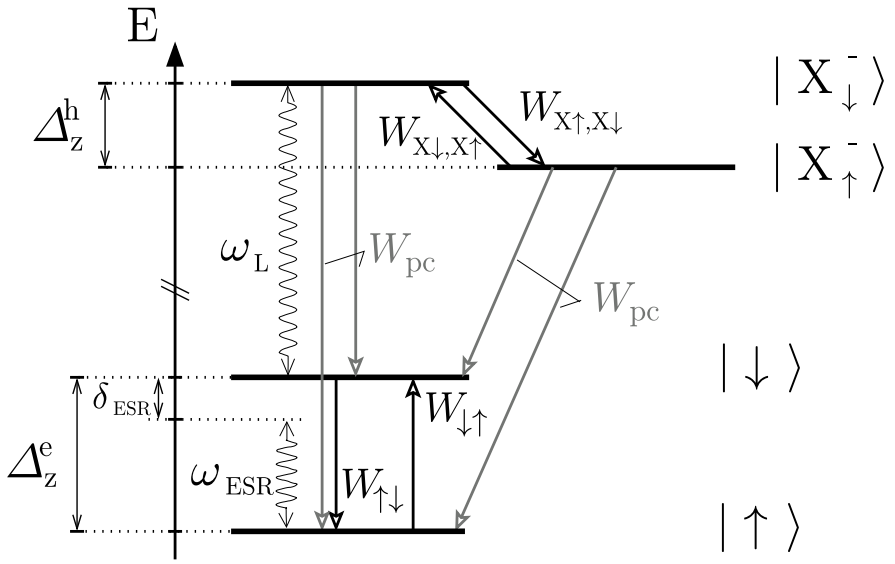

Figure 4.4: Scheme of the transitions for the readout via photocurrent. The tunneling of the electron and the hole out of the dot is spin-independent. Therefore, transitions occuring at a rate $W_{\rm pc}$ lead from the charged exciton states $|X_\uparrow^-\rangle$, $|X_\downarrow^-\rangle$ to both spin states $|\uparrow\rangle$ and $|\downarrow\rangle$, respectively. The remaining symbols are defined as in Figure 4.2.

$$\dot{\rho}_\uparrow = \Omega_{\rm ESR}{\rm Im}\rho_{\downarrow,\uparrow} + W_{\rm pc}(\rho_{X\uparrow}+\rho_{X\downarrow}) + W_{\uparrow\downarrow}\rho_\downarrow - W_{\downarrow\uparrow}\rho_\uparrow, \tag{4.24}$$

$$\dot{\rho}_\downarrow = -\Omega_{\rm ESR}{\rm Im}\rho_{\downarrow,\uparrow} + {\rm Im}(\Omega_{\rm L}^*\rho_{X\downarrow,\downarrow}) + W_{\downarrow\uparrow}\,\rho_\uparrow + W_{\rm pc}(\rho_{X\uparrow}+\rho_{X\downarrow}) - W_{\uparrow\downarrow}\,\rho_\downarrow, \tag{4.25}$$

$$\dot{\rho}_{X\downarrow} = -{\rm Im}(\Omega_{\rm L}^*\rho_{X\downarrow,\downarrow}) + W_{X\downarrow,X\uparrow}\,\rho_{X\uparrow} - (2W_{\rm pc}+W_{X\uparrow,X\downarrow})\,\rho_{X\downarrow}, \tag{4.26}$$

$$\dot{\rho}_{X\uparrow} = W_{X\uparrow,X\downarrow}\,\rho_{X\downarrow} - (2W_{\rm pc}+W_{X\downarrow,X\uparrow})\,\rho_{X\uparrow}, \tag{4.27}$$

$$\dot{\rho}_{\downarrow,\uparrow} = \frac{i}{2}\Omega_{\rm ESR}\,(\rho_\downarrow-\rho_\uparrow) - \frac{i}{2}\Omega_{\rm L}^*\rho_{X\downarrow,\uparrow} - \left(i\delta_{\rm ESR}+T_2^{-1}\right)\,\rho_{\downarrow,\uparrow}, \tag{4.28}$$

$$\dot{\rho}_{X\downarrow,\uparrow} = \frac{i}{2}\Omega_{\rm ESR}\,\rho_{X\downarrow,\downarrow} - \frac{i}{2}\Omega_{\rm L}\rho_{\downarrow,\uparrow} - [i(\delta_{\rm ESR}+\delta_{\rm L})+V_{X\downarrow,\uparrow}]\,\rho_{X\downarrow,\uparrow}, \tag{4.29}$$

$$\dot{\rho}_{X\downarrow,\downarrow} = \frac{i}{2}\Omega_{\rm ESR}\rho_{X\downarrow,\uparrow} - \frac{i}{2}\Omega_{\rm L}(\rho_\downarrow-\rho_{X\downarrow}) - (i\delta_{\rm L}+V_{\rm X})\rho_{X\downarrow,\downarrow}. \tag{4.30}$$

Note that in the expressions for $V_{\rm X}$ and $V_{X\downarrow,\uparrow}$, the previous relaxation rate $W_{\rm em}$ is now replaced by $\tilde{W}_{\rm pc}=2W_{\rm pc}$. We then obtain for the stationary solution

$$\bar{\rho}_\uparrow = \tilde{\eta}W_{\rm L}\tilde{W}_{\rm pc} + \tilde{\eta}\tilde{W}_{\uparrow\downarrow}\,\tilde{W}_{\rm pc} + \tilde{\eta}\tilde{W}_{\uparrow\downarrow}\left(W_{\rm L}+\tilde{W}_{\rm pc}\right), \tag{4.31}$$

$$\bar{\rho}_\downarrow = \tilde{\eta}\tilde{W}_{\downarrow\uparrow}\left(W_{\rm L}+\tilde{W}_{\rm pc}\right) + \tilde{\eta}\tilde{W}_{\downarrow\uparrow}\,\tilde{W}_{\rm pc}, \tag{4.32}$$

$$\bar{\rho}_{X\downarrow} = \tilde{\eta}W_{\rm L}\,\tilde{W}_{\downarrow\uparrow}, \tag{4.33}$$

$$\bar{\rho}_{X\uparrow} = \tilde{\eta}W_{\rm L}\,\tilde{W}_{\downarrow\uparrow}. \tag{4.34}$$

Here, $\tilde{\eta}$ is a normalization factor such that $\sum_n \rho_n = 1$. The photocurrent $I_{\rm pc} = e\tilde{W}_{\rm pc}(\bar{\rho}_{X\downarrow}+\bar{\rho}_{X\uparrow})$ is a Lorentzian as a function of the ESR detuning $\tilde{\delta}_{\rm ESR}$. The linewidth is bound by the inequality

$$w \;\leq\; 2\,V_{\rm ESR}\left[1+4W_{\rm ESR}^{\rm max}\left(\frac{1}{W_{\rm L}}+\frac{1}{\tilde{W}_{\rm pc}}\right)\right]^{1/2}, \tag{4.35}$$

where the right-hand side is a smaller upper bound for w than the one obtained for the photoluminescence, Eq. (4.22). This can be understood by noting that above result for the photocurrent can also be obtained from the expression for the stationary photoluminescence (see Section 4.2.3) by replacing $W_{\rm em} \to \tilde{W}_{\rm pc}$ and in the limit $W_{X\uparrow,X\downarrow}$, $W_{X\downarrow,X\uparrow} \to \infty$. The limit of infinite hole spin flip rates is responsible for the reduction of the linewidth Eq. (4.22) to the value given by Eq. (4.35) after replacing $W_{\rm em}$ with $\tilde{W}_{\rm pc}$.

4.3 Luminescence intensity autocorrelation function

The luminescence intensity autocorrelation function $\langle I(t)I(t+\tau)\rangle$ has recently been used in experiments to demonstrate the suitability of single quantum dots for single-photon sources [51, 53]. We discuss here that electron spin Rabi oscillations can be detected via $\langle I(t)I(t+\tau)\rangle$. For this, we assume that the laser polarization is changed to σ^+. At low temperatures ($kT < g_{hh}^z\mu_{\rm B}B_z$, where k is the Boltzmann constant), excitations of the hole spin are negligible since $W_{X\downarrow,X\uparrow} \ll W_{\rm em}$. Then, the energetically highest state $|X_\downarrow^-\rangle$ is decoupled from the three-level system $|\uparrow\rangle$, $|\downarrow\rangle$, and $|X_\uparrow^-\rangle$, cf. Figure 4.5. After emission of a σ^+ photon, the dot is in the state $|\uparrow\rangle$. For the transitions shown in Figure 4.5, we derive a generalized master equation similarly as Eqs. (4.6)-(4.12) were derived according to Figure 4.2. We model the time evolution of the dot state $|\uparrow\rangle$ in lowest order in $W_{\rm L}$ and obtain the probability to be in the final state $|X_\uparrow^-\rangle$ after some time τ. We consider the regime $W_{\rm L} \leq V_{\rm ESR}$ and $V_{\rm ESR} \ll \Omega_{\rm ESR} < W_{\rm em}$ and obtain for the luminescence intensity autocorrelation function

$$\langle I(t)I(t+\tau)\rangle = W_{\rm L}^2\bar{\rho}_\uparrow^2 P_\uparrow(\tau) + o(W_{\rm L}^3). \tag{4.36}$$

Here, $I(t)$ is the σ^+ luminescence intensity, $\bar{\rho}_\uparrow \approx \tilde{W}_{\uparrow\downarrow}/(\tilde{W}_{\uparrow\downarrow}+\tilde{W}_{\downarrow\uparrow})$ is the stationary occupation of $|\uparrow\rangle$, and $P_\uparrow(\tau)$ is the conditional probability to be again in the state $|\uparrow\rangle$ after the time $t+\tau$ if the state was $|\uparrow\rangle$ at time t. For $\delta_{\rm ESR} = 0$ and $W_{\uparrow\downarrow} = W_{\downarrow\uparrow}$, we find $P_\uparrow(\tau) \approx 1/2 + (1/2)\exp\left[-(\tau/2)\,(1/T_2+1/T_1)\right]\cos(\Omega_{\rm ESR}\tau)$. Thus, the inverse decay rate of the detected oscillations in $\langle I(t)I(t+\tau)\rangle$ [Eq. (4.36)] gives a lower bound on $2T_2$.

To conclude this section we stress that the single-spin relaxation time T_1 can be measured via a similar double resonance scheme as discussed for $\langle I(t)I(t+\tau)\rangle$ above.

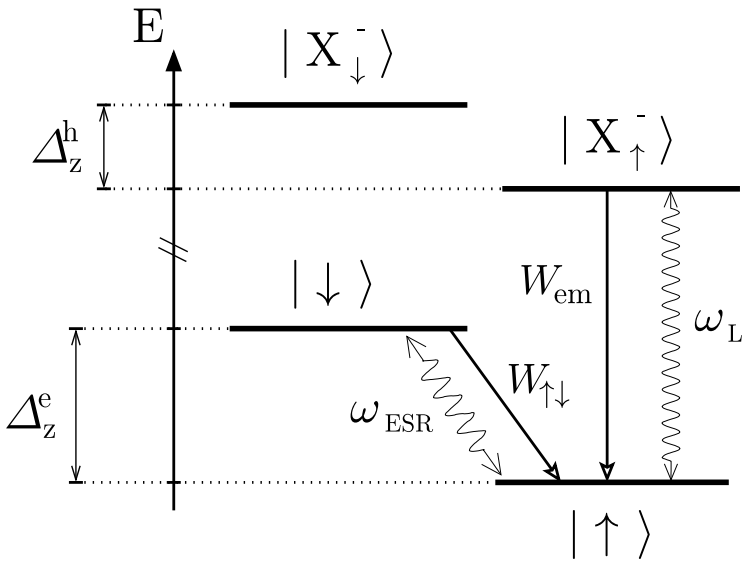

Figure 4.5: Scheme of the transitions if an ESR field and a σ^+ polarized laser field are applied. As described in the text, $|X_{\downarrow}^{-}\rangle$ is decoupled from the other three states at low temperatures. In this setup, the luminescence intensity autocorrelation function $\langle I(t)I(t+\tau)\rangle$ can be used to detect the decay of spin oscillations. Further, for a larger laser intensity, T_1 can be measured as explained in Section 4.3.

This can be done in the regime Ω_L, $W_{em} \gg \Omega_{ESR}$, $W_{\uparrow\downarrow}$, i.e., we require a larger intensity of the σ^+ laser as considered for the T_2 measurement. Then, the system is predominantly driven by the laser field. Occasionally, an ESR excitation of the electron spin interrupts the optical excitations. After relaxation of the spin, the laser again acts on the dot and gives rise to photoluminescence. The mean time of photoluminescence interruptions due to ESR excitation is thus given by T_1, similarly as for a single atom [183].

4.4 Spin Rabi-oscillations via photoluminescence

The photoluminescence Γ can be measured as a function of the pulse repetition time τ_{rep} of a pulsed laser while keeping δ_{ESR} constant. We again consider cw ESR and choose σ^- for the laser polarization, while the laser bandwidth should still be smaller than $\delta\epsilon$ and Δ_{hh-lh}, see Section 4.2. Since excessive population is trapped in the state $|\uparrow\rangle$ during a laser pulse due to hole spin flips and subsequent emission of a photon, the dot is preferably in the state $|\uparrow\rangle$ (rather than $|\downarrow\rangle$) at the end of a laser pulse. During the "off" time of the laser between two pulses, the rf field rotates the electron spin. The next laser pulse then reads out the spin state $|\downarrow\rangle$. Thus, as a function of τ_{rep}, the spin Rabi oscillations can be observed in the photoluminescence

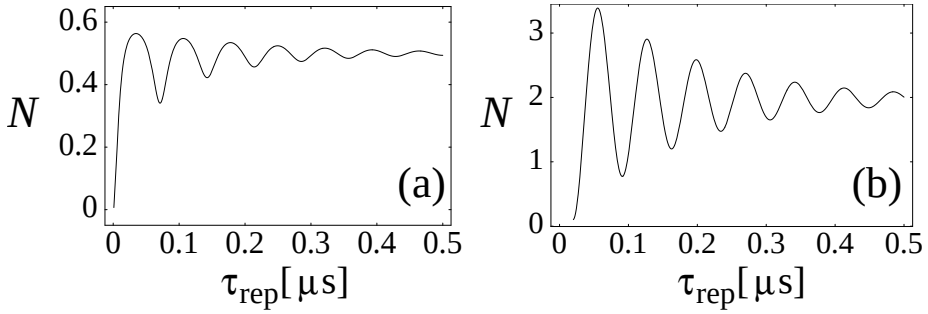

Figure 4.6: The average number $N = \Gamma\tau_{\rm rep}$ of photons emitted per period $\tau_{\rm rep}$ as a function of the laser pulse repetition time $\tau_{\rm rep}$. In (a), π pulses are used for the laser with $\Delta t = 5\,\text{ps}$ and $\Omega_{\rm L} = \pi/\Delta t$. In (b), N is shown for pulses with $\Delta t = 20\,\text{ns}$ and $\Omega_{\rm L} = \pi/(500\,\text{ps})$. We have set $\delta_{\rm ESR} = 0$. The other parameters are the same as in Figure 4.3. The decay of the oscillation depends on T_2.

(similarly as in $\langle I(t)I(t+\tau)\rangle$), see Figure 4.6. To model the pulsed laser excitation, we consider square pulses of length Δt, for simplicity. In the generalized master equation $\dot\rho(t) = \mathcal{M}(t)\rho(t)$, we write $\mathcal{M}(t) = \mathcal{M}_{\rm L}$ [where $\mathcal{M}_{\rm L}$ is defined via Eqs. (4.6) - (4.12)] during a laser pulse and $\mathcal{M}(t) = \mathcal{M}_0$ otherwise, setting $\Omega_{\rm L} = 0$. We obtain the steady-state density matrix ρ_∞ of the dot state just after the pulse from $U_p\rho_\infty = \rho_\infty$, where $U_p = \exp(\mathcal{M}_{\rm L}\Delta t)\exp[\mathcal{M}_0(\tau_{\rm rep} - \Delta t)]$ describes the time evolution of ρ during $\tau_{\rm rep}$.

The steady-state photoluminescence is now calculated by $\Gamma = W_{\rm em}\overline{(\rho_{X\downarrow} + \rho_{X\uparrow})}$, where the bar symbolizes time averaging over many periods $\tau_{\rm rep}$. If the laser pulse duration is longer than the lifetime of a negatively charged exciton, $\Delta t > W_{\rm em}^{-1}$ (and not shorter than an optical π-pulse), the spin oscillations become more pronounced, see Figure 4.6 (b). This is because after an optical recombination of the state $|X_\downarrow^-\rangle$, the laser pulse is still on and excites the state $|\downarrow\rangle$ again to $|X_\downarrow^-\rangle$. This iterated excitation increases the total probability of a hole-spin flip during a laser pulse and therefore the total population trapped in the state $|\uparrow\rangle$.

4.5 Spin precession via photoluminescence

Similar to Rabi oscillations, the precession of a single electron spin in a static magnetic field can also be observed if pulsed laser excitation is applied to a quantum dot charged with a single excess electron. For this, we consider the Voigt geometry, i.e., a static magnetic field is applied in a direction x, transverse to the laser beam direction z. We again assume circular polarization of the laser. Consequently, the optical transitions are between the spin states along the quantization axis in z direction, see Figure 4.7. For low temperatures [185] and for $W_{\rm em} \gg \Omega_x^h = g_h^x\mu_{\rm B}B_x/2$, where Ω_x^h is the hole-spin precession frequency, we can neglect hole-spin flips. Then, a state $|\downarrow\rangle$ is

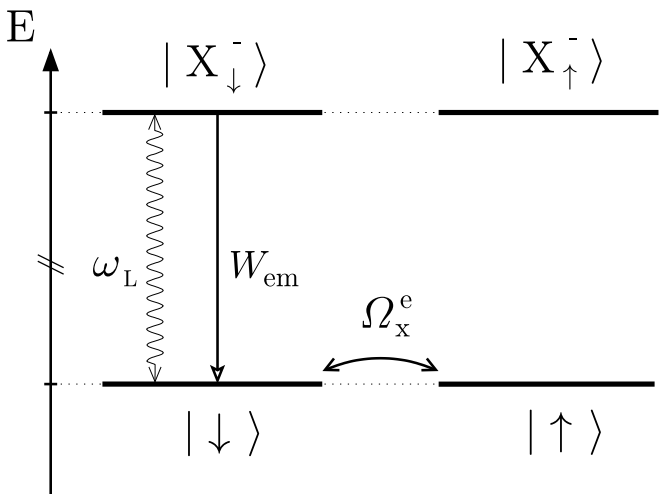

Figure 4.7: Level scheme of the spin states in the z direction in the Voigt geometry. Optical transitions with circular polarization occur vertically in this scheme. The transverse magnetic field B_x leads to spin precession, i.e., periodic oscillations between the spin states $|\uparrow\rangle$ and $|\downarrow\rangle$ at a frequency $\Omega_x^e = g_e^x \mu_{\rm B} B_x/2$. In this figure, we do not illustrate the precession of hole spins, assuming that $W_{\rm em} \gg \Omega_x^h = g_h^x \mu_{\rm B} B_x/2$.

obtained in the dot after the absorption of a σ^- laser pulse and subsequent optical recombination. This is not an eigenstate of the quantum dot in the presence of the magnetic field B_x. In the absence of an environment, the initial spin state $|\downarrow\rangle$ (at $t = 0$) evolves in time according to $\cos(\Omega_x^e t)|\downarrow\rangle - i\sin(\Omega_x^e t)|\uparrow\rangle$ with precession frequency $\Omega_x^e = g_e^x \mu_{\rm B} B_x/2$. However, the spin precession decays due to decoherence. Using pulsed laser excitation, the photoluminescence $\Gamma(\tau_{\rm rep})$ as a function of the pulse repetition time $\tau_{\rm rep}$ oscillates according to the spin precession and damping is induced by the spin decoherence, similarly as with ESR (see Sections 4.3 and 4.4). In the regime where the hole-spin flip rate is not small compared to $W_{\rm em}$, the visibility of these photoluminescence oscillations is reduced, similarly as in Section 4.4, where the spin polarization was decreased for short laser pulses, see Figure 4.6 (a). Finally, we underline that in contrast to the detection of spin Rabi oscillations (driven by ESR), in this setup spin decoherence is measured in the absence of a driving field.

4.6 Conclusion

In this chapter we have proposed to measure T_2 of a single electron spin in a semiconductor quantum dot via ODMR [150, 151]. We have shown in Section 4.2.3 that the linewidth of the photoluminescence as a function of the ESR frequency provides a lower bound on T_2. Extending this result [151], we have elaborated on the readout via photocurrent in Section 4.2.4 and in Section 4.3 we have discussed the autocorrelation function of the luminescence intensity as another possible detection scheme.

Further, we have identified a regime where T_1 can be measured optically. We have shownn in Section 4.4 that electron spin Rabi oscillations can be detected via the photoluminescence if pulsed laser and cw ESR excitation is applied. Using pulsed laser excitation, electron spin precession can be detected with similar schemes, as we have discussed in Section 4.5. The discussed cw and pulsed optical detection schemes can also be combined with pulsed instead of cw ESR, allowing spin echo and similar standard techniques to be used. Such pulsed ESR can be induced, e.g., optically via the ac Stark effect [186, 187].

Chapter 5

Molecular spintronics: Coherent spin transfer in coupled quantum dots

Recently, coherent transfer of electron spin has been observed between colloidal CdSe quantum dots with different radii $r_A \simeq 1.7\,\mathrm{nm}$ (quantum dot A) and $r_B \simeq 3.5\,\mathrm{nm}$ (quantum dot B) coupled by a benzene ring [70]. The different dot size allows one to selectively pump and probe the spin polarization for dots of species A and B. The main result of Ref. [70] is that an electron spin polarization created by optical pumping in dot B is transferred 'instantaneously' to dot A. The efficiency of this transfer mechanism is of order 10% at low temperatures $T < 50\,\mathrm{K}$ and increases to approximately 20% for $T \gtrsim 100\,\mathrm{K}$. The observed shift of the exciton energies to lower values compared to isolated dots is also consistent with a coherent delocalization of the electron or hole over the system formed by the quantum dots and the bridging molecule.

The purpose of this chapter is to show that a two-site Hamiltonian with a transfer term captures some of the essential experimental features of the described system [188]. We aim at calculating the dependence of the experimentally observed Faraday rotation signal as a function of probe energy on microscopic parameters such as spin transfer probabilities. The Faraday rotation angle θ_F is proportional to the difference in refractive indices for $\sigma^{\pm}$ circularly polarized light which is determined by the difference of the dielectric response functions. We calculate the dielectric response functions of coupled quantum dots and derive an analytical expression for the Faraday rotation angle in terms of electron transfer probabilities and Heisenberg exchange splittings. The experimental data provide strong evidence that the spin transfer is mediated by the π-conjugated molecule. We do not aim to describe this transfer mechanism microscopically, but consider the transfer matrix elements for electrons and holes as parameters of the Hamiltonian.

In Section 5.1 we present our model for the system of two molecularly coupled quan-

tum dots. Faraday rotation is introduced in Section 5.2 and we study its time-resolved application to a toy model of an electron delocalized over two dots A and B in Section 5.3. In Section 5.4, we calculate the Faraday rotation angle as a function of the probe energy for an initial spin polarization created by optical pumping, the method that was studied experimentally [70]. We take into account both electron transfer processes and the Coulomb interaction and show that these terms give rise to an exchange splitting of the two-exciton eigenstates. In Section 5.5, we perform the related analysis for a system in which an initial spin polarization is created not by optical pumping but by doping of the dots. In Section 5.6, we discuss our results for the parameters of CdSe quantum dots coupled by benzene molecules [70], calculate the transfer matrix element and spin transfer probabilities. We conclude in Section 5.7.

5.1 Model for molecularly coupled quantum dots

For CdSe quantum dots with radii r_A and r_B, the single-particle level spacing for electrons and holes is large compared to the temperatures $T \leq 200\,\mathrm{K}$ explored experimentally. This allows us to restrict our attention to the lowest orbital levels in the conduction and valence band of both dots. A possible admixing of higher orbital levels caused by the Coulomb interaction is determined by the parameter $r_{A,B}/a_X$, where $a_X \simeq 5.4\,\mathrm{nm}$ is the exciton radius for CdSe [189]. For the small dots in Ref. [70], the Coulomb interaction is small compared to the single-particle level spacing, such that the admixing of higher orbital levels to the ground state is small as well. (For details on experimental parameters, see Section 5.6.) This allows us to describe the coupled quantum dots by the Hamiltonian

$$\hat{H} = \hat{H}_0 + \hat{H}_{\mathrm{Coul}} + \hat{H}_T, \tag{5.1}$$

where

$$\hat{H}_0 = \sum_{\nu=A,B} \sum_{\sigma=\pm} \left(E_c^\nu \hat{c}_{c,\sigma}^{\nu\dagger} \hat{c}_{c,\sigma}^\nu + E_v^\nu \hat{c}_{v,\sigma}^{\nu\dagger} \hat{c}_{v,\sigma}^\nu \right) \tag{5.2}$$

contains the single-particle levels of uncoupled dots $\nu = A, B$. The operators $\hat{c}_c^{\nu,\sigma}$ and $\hat{c}_v^{\nu,\sigma}$ annihilate an electron in the lowest level E_c^ν of the conduction band with spin quantum number $s_z = \sigma 1/2$ and the highest level in the valence band, E_v^ν, with angular momentum $j_z = \sigma 3/2$, respectively, where $\sigma = \pm$. Here, we have adopted a simple model for the change in the band structure of CdSe due to the quantum dot confinement. We assume a spherical dot shape and a splitting of the $j = 3/2$ valence band at the Γ point into the heavy hole (hh) and light hole (lh) subband with total angular momentum projection $j_z = \pm 3/2$ and $j_z = \pm 1/2$, respectively, as obtained, e.g., from the Luttinger Hamiltonian with an additional anisotropy term for the crystal field of the hexagonal lattice [171]. The lh subband will be neglected in the following. The Coulomb interaction energy is

$$\hat{H}_{\mathrm{Coul}} = \sum_{\nu=A,B} \frac{U_\nu}{2} \left[\hat{n}_c^\nu (\hat{n}_c^\nu - 1) + \hat{n}_v^\nu (\hat{n}_v^\nu - 1) - 2 \hat{n}_c^\nu \hat{n}_v^\nu \right], \tag{5.3}$$

where $\hat{n}_c^\nu = \sum_{\sigma=\pm} \hat{c}_{c,\sigma}^{\nu\dagger} \hat{c}_{c,\sigma}^{\nu}$ and $\hat{n}_v^\nu = \sum_{\sigma=\pm} \hat{c}_{v,\sigma}^{\nu} \hat{c}_{v,\sigma}^{\nu\dagger}$ are the number operators for electrons in the conduction band level and holes in the valence band level. $U_\nu \simeq e^2/4\pi\epsilon\epsilon_0 r_\nu$ is the characteristic charging energy of dot A and B, respectively. Transfer of spin and charge between the quantum dots is accounted for by the transfer Hamiltonian

$$\hat{H}_T = \sum_{\sigma=\pm} \left(t_c \hat{c}_{c,\sigma}^{A\dagger} \hat{c}_{c,\sigma}^{B} + t_v \hat{c}_{v,\sigma}^{A\dagger} \hat{c}_{v,\sigma}^{B} + \text{H.c.} \right), \tag{5.4}$$

where we assume that transfer of electrons through the π-conjugated molecule conserves the electron spin both in the conduction and the valence band.

The ansatz for the Hamiltonian in Eqs. (5.1)–(5.4) is a model in which the biexciton shift, the exciton fine structure, and the electrostatic coupling between the two dots have been neglected. We will justify this in Section 5.6 below where we discuss our results for the experimental parameters of Ref. [70]. Because the focus of this work is to calculate the Faraday rotation angle that results from transfer of electrons between the quantum dots, we assume for simplicity that the symmetry axis of the dots with hexagonal crystal structure is parallel to the direction of pump and probe laser pulses. The effect of a random orientation will be discussed in Section 5.6.

5.2 Faraday rotation

Michael Faraday reported in 1846 that the plane of polarization of light transmitted through certain glasses or liquids is rotated by some angle if a magnetic field is applied to the substance [190]. This magneto-optic effect is nowadays referred to as the Faraday rotation or as the Faraday effect. Time-resolved Faraday rotation has been established as an extremely successful technique to observe spin dynamics in semiconductors on a femtosecond time scale [12, 13, 14, 22, 24, 191]. In this method, a circularly polarized "pump" laser pulse excites spin-polarized carriers. A second, linearly polarized "probe" laser pulse experiences Faraday rotation and thus probes the spin population. With an adjustable time delay between pump and probe pulse, the time evolution of an electron spin, for instance, precessing in the presence of a transverse magnetic field, can be detected by Faraday rotation. The Faraday rotation angle θ_F is determined by the population imbalance between the $s_z = \pm 1/2$ conduction band states [192, 193, 194]. For a probe pulse frequency E/h, θ_F is proportional to the difference of the real parts of the dielectric response functions $\epsilon(E)$ for $\sigma^\pm$ circularly polarized light [192]. With the spectral representation of the response functions, $\theta_F(E)$ is expressed in terms of the transition matrix elements between the state $|\psi(t)\rangle$ with energy E_0 and all intermediate states $|\psi_i\rangle$ which are

virtually excited by the probe pulse,

$$\theta_F(E,t) = CE\sum_{|\psi_i\rangle}\frac{E-(E_i-E_0)}{[E-(E_i-E_0)]^2+\Gamma^2} \times\left(\left|\langle\psi_i|\hat{P}_+|\psi(t)\rangle\right|^2-\left|\langle\psi_i|\hat{P}_-|\psi(t)\rangle\right|^2\right). \tag{5.5}$$

The polarization operators $\hat{P}_\pm = d_\nu \hat{c}^{\nu\dagger}_{c,\pm}\hat{c}^{\nu}_{v,\pm}$ couple to the $\sigma^\mp$ circularly polarized components of the probe pulse. d_ν is the dipole transition matrix element (as introduced in Section 2.4.1) for transition from the $j_z = \pm 3/2$ valence band states to the $s_z = \pm 1/2$ conduction band states in the dot ν. E_0 and E_i are the energy eigenvalues of the initial state and the intermediate state $|\psi_i\rangle$, respectively, and the level broadening Γ accounts for a finite lifetime of the orbital levels. The prefactor $C \propto L/(hcn_0)$ is determined by the size L of the sample and the refraction index n_0 (of bulk CdSe in our case).

5.3 Time-resolved Faraday rotation for coupled quantum dots

Before we calculate the Faraday rotation angle θ_F for the general Hamiltonian Eq. (5.1) in Sections 5.4 and 5.5 below, we first consider time-resolved Faraday rotation for a particularly simple case in which a single electron is in a coherent superposition of states in dots A and B at time $t = 0$, $|\psi(0)\rangle = (\hat{c}^{B\dagger}_{c,+} + \alpha\hat{c}^{A\dagger}_{c,+})|0\rangle/\sqrt{1+\alpha^2}$. We further assume $t_{c,v} = 0$ and $E_c^A = E_c^B$ in Eq. (5.1) for $t > 0$. Here, $|0\rangle$ denotes the vacuum state in which the valence band in both quantum dots is filled and the conduction band states are empty. This simple scenario, although unrealistic because transfer matrix elements are assumed to vanish after the initial state $|\psi_0\rangle$ has been prepared, will allow us to derive simple analytical expressions for the Faraday rotation angle even in presence of a magnetic field. The simplifying assumptions $t_{c,v} = 0$ and $E_c^A = E_c^B$ will be lifted in the microscopic discussion in Sections 5.4 and 5.5.

The different radii r_A and r_B of the CdSe dots lead to different g-factors and different Larmor precession frequencies $\omega_\nu = g_\nu\mu_B B_{ext}/\hbar$ [24, 195, 196], where B_{ext} is an external magnetic field perpendicular to the spin quantization axis which is given by the symmetry axis of the CdSe quantum dots, and g_ν are the electron g-factors for $\nu = A, B$. At time t,

$$|\psi(t)\rangle = \frac{1}{\sqrt{1+\alpha^2}}\Big[\cos(\omega_B t/2)\hat{c}^{B\dagger}_{c,+} - i\sin(\omega_B t/2)\hat{c}^{B\dagger}_{c,-} +\alpha\cos(\omega_A t/2)\hat{c}^{A\dagger}_{c,+} - i\alpha\sin(\omega_A t/2)\hat{c}^{A\dagger}_{c,-}\Big]|0\rangle. \tag{5.6}$$

Because we have assumed for the initial state $|\psi(0)\rangle$ a single-electron state (with energy $E_0 = E_c^B$), all intermediate states $|\psi_i\rangle$ in Eq. (5.5) are energy eigenstates

with two electrons and one hole. For $t_{c,v} = 0$ in Eq. (5.1), these are of the form $|\psi_i\rangle = \hat{c}^{\nu\dagger}_{c,\sigma}\hat{c}^{\nu}_{v,\sigma}\hat{c}^{\nu'\dagger}_{c,\sigma'}|0\rangle$ with $\sigma, \sigma' = \pm$ and $\nu, \nu' = A, B$. Pauli blocking prohibits the creation of an exciton with electron spin $\sigma 1/2$ if the conduction band level is already occupied by an electron with the same spin. The resulting difference in transition matrix elements for $\hat{P}_+ = d_A\hat{c}^{A\dagger}_{c,+}\hat{c}^{A}_{v,+} + d_B\hat{c}^{B\dagger}_{c,+}\hat{c}^{B}_{v,+}$ and $\hat{P}_- = d_A\hat{c}^{A\dagger}_{c,-}\hat{c}^{A}_{v,-} + d_B\hat{c}^{B\dagger}_{c,-}\hat{c}^{B}_{v,-}$ is proportional to the population imbalance of the $s_z = \pm 1/2$ levels. For a probe pulse at time t, from Eq. (5.5) we obtain directly

$$\begin{aligned}\theta_F(E,t) &= \frac{CE}{1+\alpha^2}\left[d_B^2\frac{E-E_X^B}{(E-E_X^B)^2+\Gamma^2}\cos(\omega_B t)\right. \\ &\qquad \left. +\alpha^2 d_A^2\frac{E-E_X^A}{(E-E_X^A)^2+\Gamma^2}\cos(\omega_A t)\right], \end{aligned} \tag{5.7}$$

where $E_X^\nu = E_c^\nu - E_v^\nu - U_\nu$ is the exciton energy for quantum dot ν.

$\theta_F(E,t)$ shows coherent oscillations with frequencies ω_A and ω_B caused by the electron spin precessing around the external magnetic field. In reality, these coherent oscillations are exponentially damped with a spin dephasing rate Γ_S which is typically much smaller than the orbital dephasing rate, $\Gamma_S \ll \Gamma$. Taking into account spin dephasing, the Fourier transform of the time-resolved Faraday rotation signal as a function of the probe pulse energy E and the Fourier frequency ω is

$$\begin{aligned}\theta_F(E,\omega) &= \frac{CE}{1+\alpha^2}\left[d_B^2\frac{E-E_X^B}{\left(E-E_X^B\right)^2+\Gamma^2}\frac{\Gamma_S}{\left(\omega-\omega_B\right)^2+\Gamma_S^2}\right. \\ &\qquad \left. +\alpha^2 d_A^2\frac{E-E_X^A}{(E-E_X^A)^2+\Gamma^2}\frac{\Gamma_S}{\left(\omega-\omega_A\right)^2+\Gamma_S^2}\right]. \end{aligned} \tag{5.8}$$

$\theta_F(E,\omega)$ shows characteristic features for $E \simeq E_X^\nu$ and $\omega \simeq \omega_\nu$. The two terms in Eq. (5.8) describe the dielectric response due to virtual creation of an exciton in quantum dot A and B, respectively. For $E_X^B \le E \le E_X^A$, they have different sign and may cancel. Figure 5.1(a) shows a grayscale plot of $|\theta_F(E,\omega)|$ for the experimental values $E_X^B = 2.06\,\mathrm{eV}$, $E_X^A = 2.41\,\mathrm{eV}$, $\Gamma = 0.05\,\mathrm{eV}$, and $\Gamma_S/2\pi = 0.5\,\mathrm{GHz}$, assuming $d_A^2/d_B^2 = 1$ and $\alpha^2 = 0.2$. For Figure 5.1(b), $\Gamma = 0.035\,\mathrm{eV}$, and $\Gamma_S/2\pi = 1.2\,\mathrm{GHz}$, and $\alpha^2 = 0.4$. One of the most characteristic features of the experimental data (Figure 2D in Ref. [70]) is that $|\theta_F(E,\omega)|$ vanishes and reappears as a function of probe pulse frequency E for $\omega \simeq \omega_\nu$. This can also be clearly seen in the theoretical result.

Above, we have assumed that the electron delocalized over both dots at $t = 0$ retains spatial coherence. For rapid decoherence of the orbital part of the wave function, the initial state is described by the density matrix

$$\hat{\rho} = \frac{1}{1+\alpha^2}\left(\hat{c}^{B\dagger}_{c,+}|0\rangle\langle 0|\hat{c}^{B}_{c,+} + \alpha^2\hat{c}^{A\dagger}_{c,+}|0\rangle\langle 0|\hat{c}^{A}_{c,+}\right). \tag{5.9}$$

The Faraday rotation signal in this case is the incoherent superposition of the Faraday rotation signals for dot A and B, and is identical to the results in Eqs. (5.7) and

(5.8). Hence, a Faraday rotation signal as shown in Figure 5.1 does not allow one to distinguish coherent from incoherent spatial superpositions.

5.4 Optical spin injection

In the preceding section, $\theta_F(E)$ was calculated for the simple case of a single electron delocalized over the coupled quantum dots. So far, we have also neglected that all intermediate states $|\psi_i\rangle$ in Eq. (5.5) that are virtually excited by the probe pulse will be modified by finite transfer energies $t_{c,v}$. We next turn to a microscopic analysis in which we take into account $t_{c,v} \neq 0$ also for the intermediate states.

In Ref. [70], the initial state prepared by optical pumping is a one-exciton state. As described by Eq. 5.5 in Section 5.2 above, the Faraday rotation angle as a function of probe energy is proportional to the difference of dielectric response functions for $\sigma^{\pm}$ circularly polarized light. In order to evaluate this expression, both the initial one-exciton state and all intermediate two-exciton states which are virtually excited by the probe pulse must be calculated for the coupled quantum dots. In this section, we first calculate the one-exciton energy eigenstate of the coupled dots prepared by the pump pulse and subsequently identify all two-exciton eigenstates $|\psi_i\rangle$ which are virtually excited by the probe pulse. Our analysis is based on perturbation theory in the transfer energies and is valid if $|t_{c,v}|$ is the smallest energy scale, $|t_{c,v}| \ll \delta E_c, |\delta E_v|, U_A, U_B, |\delta E_{c,v} \pm U_{A,B}|$. Here, we have defined the energy differences $\delta E_c = E_c^A - E_c^B \geq 0$ and $\delta E_v = E_v^A - E_v^B \leq 0$ between the conduction and valence band levels of dots A and B.

In Ref. [70], an initial spin polarization was created by optical pumping. For $t_{c,v} = 0$, the states $\hat{c}_{c,\sigma}^{\nu\dagger}\hat{c}_{v,\sigma}^{\nu}|0\rangle$ are one-exciton eigenstates with energy eigenvalues

$$E_X^{\nu(0)} = E_c^{\nu} - E_v^{\nu} - U_{\nu} \tag{5.10}$$

which are prepared by absorption of a $-\sigma$ circularly polarized pump pulse. To first order in the transfer energies $t_{c,v}$, the energy eigenstates are

$$|X_{A,\sigma}\rangle = \hat{c}_{c,\sigma}^{A\dagger}\hat{c}_{v,\sigma}^{A}|0\rangle + \left(\frac{t_c}{\delta E_c - U_A}\hat{c}_{c,\sigma}^{B\dagger}\hat{c}_{v,\sigma}^{A} + \frac{t_v}{\delta E_v + U_A}\hat{c}_{c,\sigma}^{A\dagger}\hat{c}_{v,\sigma}^{B}\right)|0\rangle, \tag{5.11a}$$

$$|X_{B,\sigma}\rangle = \hat{c}_{c,\sigma}^{B\dagger}\hat{c}_{v,\sigma}^{B}|0\rangle + \left(-\frac{t_c}{\delta E_c + U_B}\hat{c}_{c,\sigma}^{A\dagger}\hat{c}_{v,\sigma}^{B} - \frac{t_v}{\delta E_v - U_B}\hat{c}_{c,\sigma}^{B\dagger}\hat{c}_{v,\sigma}^{A}\right)|0\rangle, \tag{5.11b}$$

with eigenenergies

$$E_X^A = E_X^{A(0)} + \frac{t_c^2}{\delta E_c - U_A} - \frac{t_v^2}{\delta E_v + U_A}, \tag{5.12a}$$

$$E_X^B = E_X^{B(0)} - \frac{t_c^2}{\delta E_c + U_B} + \frac{t_v^2}{\delta E_v - U_B}. \tag{5.12b}$$

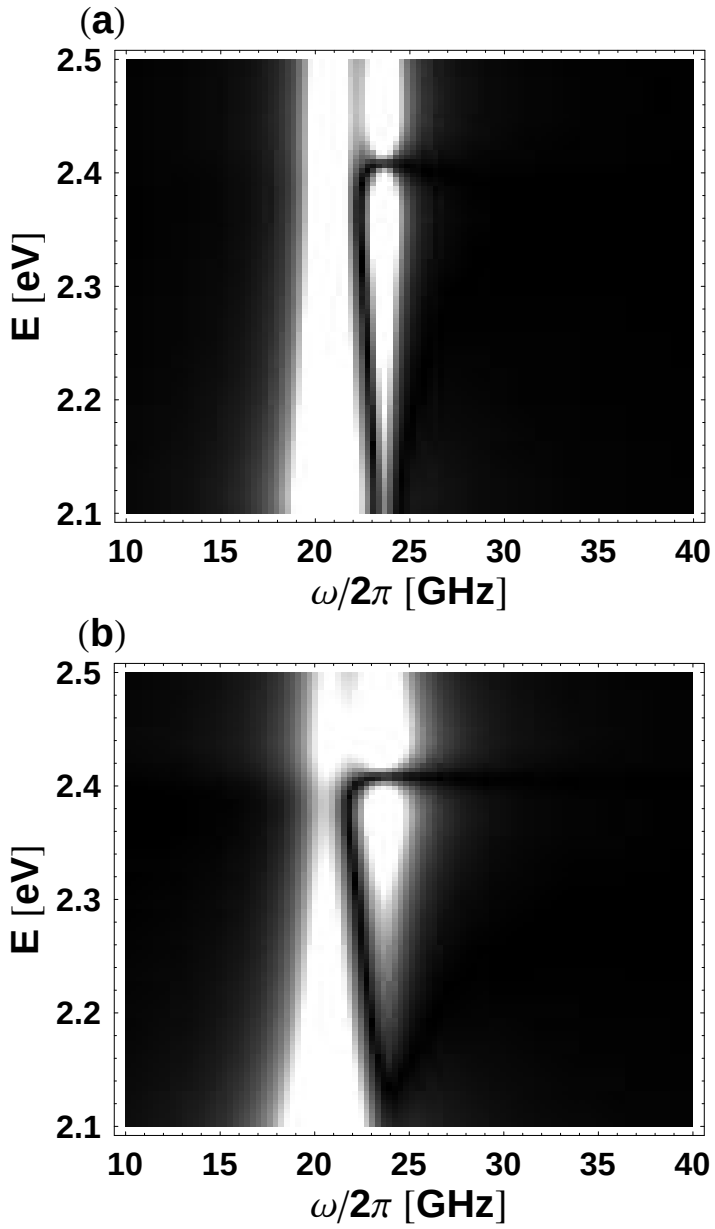

Figure 5.1: (a) Grayscale plot of the Faraday rotation angle $|\theta_F|$ [given in Eq. (5.8)] as a function of the probe-pulse frequency E/h and spin precession frequency $f = \omega/2\pi$. We have chosen the parameters [70] $E_X^A = 2.41\,\mathrm{eV}$, $E_X^B = 2.06\,\mathrm{eV}$, $\omega_A/2\pi = 23.6\,\mathrm{GHz}$, $\omega_B/2\pi = 20.6\,\mathrm{GHz}$, $\Gamma = 0.05\,\mathrm{eV}$, $\Gamma_S/2\pi = 0.5\,\mathrm{GHz}$, and $\alpha^2 = 0.2$. (b) For $\Gamma = 0.035\,\mathrm{eV}$, $\Gamma_S/2\pi = 1.2\,\mathrm{GHz}$, and $\alpha^2 = 0.4$, pronounced features caused by the interplay of the two terms in Eq. (5.8) become more clearly visible. In particular, the Faraday rotation signal at $\omega \simeq \omega_B$ vanishes and reappears as a function of probe-pulse frequency E.

As expected, the eigenenergies are shifted due to the delocalization of electrons and holes over the coupled quantum dots. The exciton states in Eq. (5.11) are the only one-exciton states which can be prepared by the absorption of a photon with circular polarization $-\sigma$ if the photon is incident along the hexagonal axis of the CdSe crystal structure. However, a photon with energy $E \simeq E_X^B$ no longer creates an exciton only in dot B, but an exciton in which electron and hole are delocalized over the coupled quantum dot system. This delocalization of the quantum mechanical wave function is consistent with the short time-scale for spin transfer observed experimentally [70].

We now turn to the calculation of the Faraday rotation angle, assuming that the pump pulse has prepared an initial state $|\psi\rangle = |X_{B,+}\rangle$. The evaluation of the dielectric response function will require us to calculate all two-exciton states that are virtually excited by the probe pulse. Interesting features in the Faraday rotation signal effected by spin transfer are of order $t_{c,v}^2$. In order to keep the following expressions simple, we assume that spin is transferred between the conduction band states and set $t_v = 0$. Then, only the seven states $|A_+B_+\rangle$, $|T_0\rangle$, $|S\rangle$, $|B_+B_-\rangle$, $|\tilde{T}_0\rangle$, $|\tilde{S}\rangle$, and $|\widetilde{B_+B_-}\rangle$ listed below and in Appendix C have finite matrix elements up to $\mathcal{O}(t_c^2)$ with $\hat{P}_\pm|X_{B,+}\rangle$. For $\delta E_v + U_A \neq 0$, only the eigenenergies of $|A_+B_+\rangle$, $|T_0\rangle$, and $|S\rangle$ are close to the excitation energy of a probe pulse with frequency $E/h \simeq E_X^A/h$. Hence, these states dominate the spectral representation in Eq. (5.5). Still, two-exciton eigenstates which are energetically offset compared to $E + E_X^B$ will also contribute to the Faraday rotation signal. However, their contribution varies slowly as a function of probe energy and leads at most to an offset in the results derived below. See also Appendix C.

The polarization operator $\hat{P}_+$ induces transitions from the initial state $|X_{B,+}\rangle$ to

$$|A_+B_+\rangle = \hat{c}_{c,+}^{A\dagger}\hat{c}_{c,+}^{B\dagger}\hat{c}_{v,+}^{A}\hat{c}_{v,+}^{B}|0\rangle \tag{5.13}$$

with energy eigenvalue

$$E_{A_+B_+} = E_X^{A(0)} + E_X^{B(0)}. \tag{5.14}$$

The notation indicates that two electrons with the same spin $s_z = 1/2$ occupy the conduction band states in dots A and B, respectively, and form a spin triplet state. $|A_+B_+\rangle$ is an exact eigenstate of the Hamiltonian even for $t_c \neq 0$ because transfer of the conduction band electrons is blocked by the Pauli exclusion principle. The matrix element $\langle A_+B_+|\hat{P}_+|X_{B_+}\rangle$ is the only finite matrix element of the operator $\hat{P}_+$.

Finite matrix elements for $\hat{P}_-$ contain the states in which the electrons in the conduction band level form a spin triplet and singlet, respectively,

$$|T_0\rangle = \frac{1}{\sqrt{2}}\left(\hat{c}_{c,-}^{A\dagger}\hat{c}_{c,+}^{B\dagger} + \hat{c}_{c,+}^{A\dagger}\hat{c}_{c,-}^{B\dagger}\right)\hat{c}_{v,-}^{A}\hat{c}_{v,+}^{B}|0\rangle, \tag{5.15a}$$

$$\begin{aligned}|S\rangle \propto\ & \frac{1}{\sqrt{2}}\left(\hat{c}_{c,-}^{A\dagger}\hat{c}_{c,+}^{B\dagger} - \hat{c}_{c,+}^{A\dagger}\hat{c}_{c,-}^{B\dagger}\right)\hat{c}_{v,-}^{A}\hat{c}_{v,+}^{B}|0\rangle \\ & +\sqrt{2}\left(\frac{t_c}{\delta E_c + U_B}\hat{c}_{c,+}^{A\dagger}\hat{c}_{c,-}^{A\dagger} - \frac{t_c}{\delta E_c - U_A}\hat{c}_{c,+}^{B\dagger}\hat{c}_{c,-}^{B\dagger}\right)\hat{c}_{v,-}^{A}\hat{c}_{v,+}^{B}|0\rangle,\end{aligned} \tag{5.15b}$$

and the holes with $j_z = -3/2$ and $j_z = +3/2$ are localized in quantum dots A and B, respectively. Note that the projection of the total conduction band spin onto the spin-quantization axis vanishes for the triplet state $|T_0\rangle$. The normalization constant for $|S\rangle$ is defined by $\langle S|S\rangle = 1$. The eigenenergies

$$E_{T_0} = E_X^{A(0)} + E_X^{B(0)}, \tag{5.16a}$$

$$E_S = E_X^{A(0)} + E_X^{B(0)} + 2t_c^2 \left(\frac{1}{\delta E_c - U_A} - \frac{1}{\delta E_c + U_B} \right) \tag{5.16b}$$

show an energy offset which is caused by the inter-dot exchange coupling [11, 134]. The energies of $|A_+B_+\rangle$ and $|T_0\rangle$ are not shifted by electron transfer because of Pauli blocking and destructive interference of transfer paths, respectively.

The state

$$\begin{aligned} |B_+B_-\rangle \propto & \left[\hat{c}_{c,+}^{B\dagger} \hat{c}_{c,-}^{B\dagger} + \frac{t_c}{\delta E_c - U_A} \left(\hat{c}_{c,-}^{A\dagger} \hat{c}_{c,+}^{B\dagger} - \hat{c}_{c,+}^{A\dagger} \hat{c}_{c,-}^{B\dagger} \right) \right. \\ & \left. + \frac{2t_c^2 \hat{c}_{c,+}^{A\dagger} \hat{c}_{c,-}^{A\dagger}}{(\delta E_c - U_A)(2\delta E_c - U_A + U_B)} \right] \hat{c}_{v,-}^{A} \hat{c}_{v,+}^{B} |0\rangle \end{aligned} \tag{5.17}$$

with

$$E_{B_+B_-} = E_X^{B(0)} + E_c^B - E_v^A - 2\frac{t_c^2}{\delta E_c - U_A} \tag{5.18}$$

is offset in energy from $E_X^{A(0)} + E_X^{B(0)}$ even to zeroth order in t_c and does not contribute significantly to $\theta_F(E)$ for $E \simeq E_X^A$. The three states in Eqs. (5.15) and (5.17) provide the dominant terms in the spectral representation for θ_F in Eq. (5.5). In particular, they exhaust the sum rule $\sum_{|\psi_i\rangle} |\langle \psi_i | \hat{c}_{c,-}^{A\dagger} \hat{c}_{v,-}^{A} | X_{B,+} \rangle|^2 = 1$ up to $\mathcal{O}(t_c^2)$. In Figure 5.2, the spin configurations for $|A_+B_+\rangle$, $|S\rangle$, and $|T_0\rangle$ are shown schematically.

From Eqs. (5.11b)–(5.18), the Faraday rotation angle θ_F is readily evaluated. We denote the electron transfer probability from dot ν to dot ν' by $p_{\nu\to\nu'}$. We obtain

$$p_{A\to B} = \left(\frac{t_c}{\delta E_c - U_A} \right)^2, \tag{5.19a}$$

$$p_{B\to A} = \left(\frac{t_c}{\delta E_c + U_B} \right)^2. \tag{5.19b}$$

For the transition matrix elements of the dipole operators in Eq. (5.5), we obtain in terms of the transfer probabilities

$$|\langle A_+B_+|\hat{P}_+|X_{B,+}\rangle|^2 = (1 - p_{B\to A})\, d_A^2, \tag{5.20a}$$

$$|\langle T_0|\hat{P}_-|X_{B,+}\rangle|^2 = \frac{1 - p_{B\to A}}{2} d_A^2, \tag{5.20b}$$

$$|\langle S|\hat{P}_-|X_{B,+}\rangle|^2 = \frac{1 + p_{B\to A} - 2p_{A\to B}}{2} d_A^2, \tag{5.20c}$$

$$|\langle B_+B_-|\hat{P}_-|X_{B,+}\rangle|^2 = p_{A\to B} d_A^2. \tag{5.20d}$$

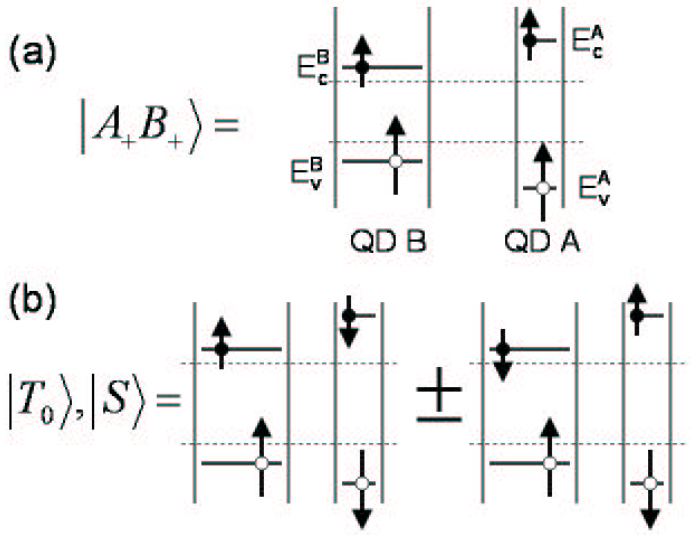

Figure 5.2: Schematic representation of the spin configurations (in the electron picture) for states (a) $|A_+B_+\rangle$ and (b) $|S\rangle$, $|T_0\rangle$ to leading order in t_c. The dashed lines represent the conduction and valence band edge in bulk CdSe.

Because of the exchange splitting $E_{T_0} - E_S$ between conduction band triplet and singlet states, finite transfer probabilities $p_{A\to B}$ and $p_{B\to A}$ lead to pronounced features in the Faraday rotation angle as a function of the probe-pulse frequency E/h. For probe energies $E_{T_0B} = E_{T_0} - E_X^B \le E \le E_{SB} = E_S - E_X^B$, the Faraday rotation signal varies strongly with energy and is given by

$$\theta_F(E) = \frac{CEd_A^2}{2}\left[(1-p_{B\to A})\,\frac{E-E_{T_0B}}{(E-E_{T_0B})^2+\Gamma^2} - (1+p_{B\to A}-2p_{A\to B})\,\frac{E-E_{SB}}{(E-E_{SB})^2+\Gamma^2}\right]. \tag{5.21}$$

For $|E - E_{SB}| \gtrsim |E_{T_0} - E_S|$, Eq. (5.21) simplifies to

$$\theta_F(E) \simeq CEd_A^2 \frac{E-E_X^{A(0)}}{\left(E-E_X^{A(0)}\right)^2+\Gamma^2}\,(p_{A\to B}-p_{B\to A})\,. \tag{5.22}$$

This result is surprising because the Faraday rotation angle is not only determined by the probability $p_{B\to A}$ that the electron created by the pump pulse has been transferred to quantum dot A. Rather, even the *sign* of the Faraday rotation angle depends on the parameters δE_c (and δE_v if transfer between valence band states is included) and $U_{A,B}$. $\theta_F \ge 0$ for $|\delta E_c - U_A| \ge |\delta E_c + U_B|$, and $\theta_F \le 0$ for $|\delta E_c - U_A| \le |\delta E_c + U_B|$. Although counterintuitive at first sight, this can be readily understood from the one- and two-exciton eigenstates. The matrix element for the virtual creation of an

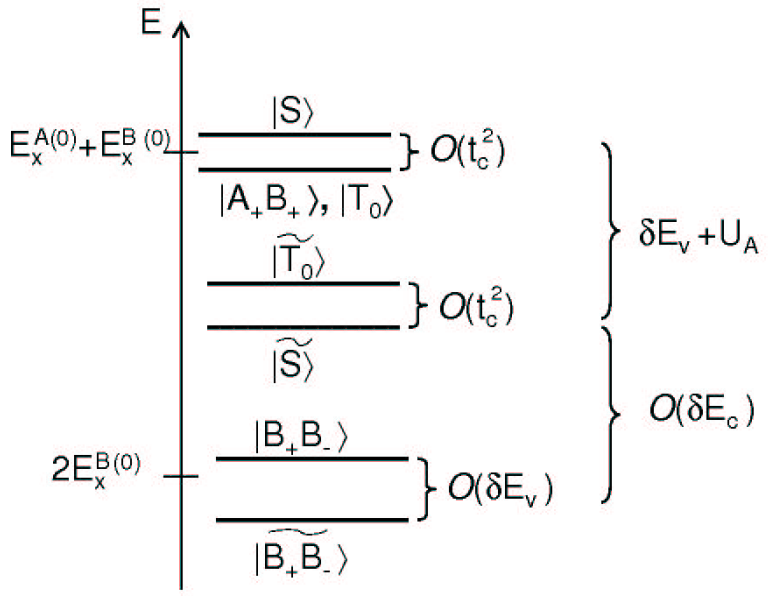

Figure 5.3: Energy level scheme of all two-exciton eigenstates discussed in the text. The eigenenergies fall into three groups which are split by terms of order $\mathcal{O}(t_c^2)$ or $\mathcal{O}(\delta E_v)$. For the dots used in Ref. [70], $\delta E_v + U_A \simeq 0$, and the five states $|A_+B_+\rangle$, $|T_0\rangle$, $|S\rangle$, $|\tilde{T}_0\rangle$, and $|\tilde{S}\rangle$ are nearly degenerate.

exciton with $s_z = 1/2$, $j_z = 3/2$ in quantum dot A is reduced by the probability $p_{B\to A}$ that the conduction band electron created by the pump pulse in B has been transferred to A. In this case, it blocks the creation of a second exciton with the same spin. The transition matrix element for the creation of an exciton with $s_z = -1/2$, $j_z = -3/2$ is reduced by the probability $p_{A\to B}$ that the electron with spin $s_z = -1/2$ in the conduction band state of quantum dot A is transferred to quantum dot B. This transfer process is not prohibited by Pauli blocking and leads to the virtual occupation of $|B_+B_-\rangle$ which is energetically far off resonance. The interplay of both processes results in Eq. (5.22).

Our derivation of Eq. (5.22) was based on the assumption that t_c is the smallest energy scale in the system. As will be discussed in Section 5.6 below, for the experimental parameters in Ref. [70], $\delta E_v + U_A \simeq 0$. For $t_v = 0$, this does not lead to divergencies in the perturbative expansion in t_c. However, these special parameters require that two additional two-exciton states are taken into account for the calculation of $\theta_F(E)$ because they are nearly degenerate with $|A_+B_+\rangle$, $|S\rangle$, and $|T_0\rangle$ (see Figure 5.3). The states $|\tilde{S}\rangle$ and $|\tilde{T}_0\rangle$ defined in Eq. (C.1) have finite overlap matrix elements with

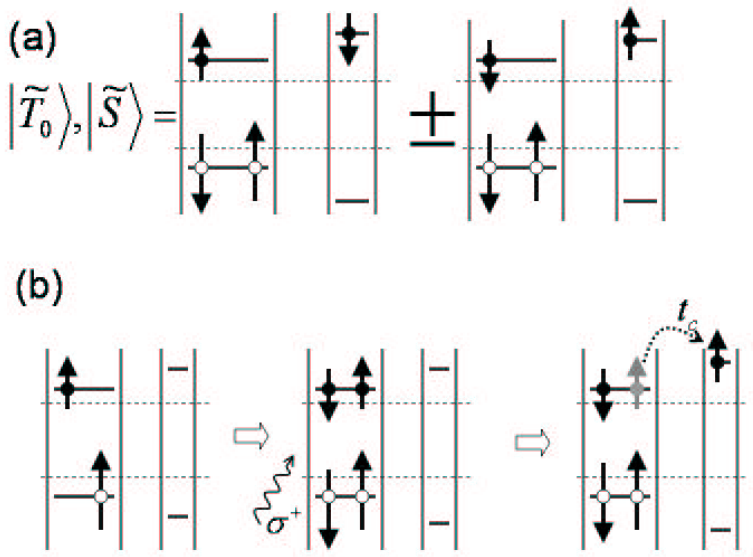

Figure 5.4: (a) Schematic representation of the spin configurations for the states $|\tilde{S}\rangle$, $|\tilde{T}_0\rangle$ to leading order in t_c. (b) Transitions between an initial state $|X_{B,+}\rangle$ and $|\tilde{S}\rangle$, $|\tilde{T}_0\rangle$ are effected by the absorption of a σ^+ polarized probe photon and subsequent tunneling of one conduction band electron.

$\hat{P}_-|X_{B,+}\rangle$,

$$|\langle\tilde{T}_0|\hat{P}_-|X_{B,+}\rangle|^2 = \frac{p_{B\to A}d_B^2}{2}, \tag{5.23a}$$

$$|\langle\tilde{S}|\hat{P}_-|X_{B,+}\rangle|^2 = \frac{p_{B\to A}d_B^2}{2}. \tag{5.23b}$$

The spin configuration for the states $|\tilde{S}\rangle$ and $|\tilde{T}_0\rangle$ are shown schematically in Figure 5.4(a). Note that both holes occupy the valence band states of quantum dot B. The accidental degeneracy of $|\tilde{S}\rangle$ and $|\tilde{T}_0\rangle$ with $|S\rangle$ and $|T_0\rangle$ arises because, for the parameters of Ref. [70], the decrease in orbital energy δE_v is comparable to the increase in Coulomb energy U_A. Transitions between an initial state $|X_{B,+}\rangle$ and $|\tilde{S}\rangle$, $|\tilde{T}_0\rangle$, are two-step processes. A σ^+ polarized probe photon creates an exciton with $s_z = -1/2$ and $j_z = -3/2$ in B, and one of the conduction band electrons in B is subsequently transferred to A. These processes are shown schematically in Figure 5.4(b).

Taking into account all two-exciton states with energies $\left|E_i - \left(E_X^{A(0)} + E_X^{B(0)}\right)\right| \lesssim$

$\max[|\delta E_v + U_A|, |E_{T_0} - E_S|]$, the Faraday rotation angle is

$$\begin{aligned}\theta_F(E) &= \frac{CE}{2}\left\{d_A^2\left[(1-p_{B\to A})\,\frac{E-E_{T_0B}}{(E-E_{T_0B})^2+\Gamma^2}\right.\right. \\ &\qquad \left. - (1+p_{B\to A}-2p_{A\to B})\,\frac{E-E_{SB}}{(E-E_{SB})^2+\Gamma^2}\right] \\ &\qquad \left. -d_B^2 p_{B\to A}\left[\frac{E-E_{\tilde{T}_0B}}{(E-E_{\tilde{T}_0B})^2+\Gamma^2}+\frac{E-E_{\tilde{S}B}}{(E-E_{\tilde{S}B})^2+\Gamma^2}\right]\right\}. \end{aligned} \tag{5.24}$$

The energy differences $E_{\tilde{T}_0B} = E_{\tilde{T}_0} - E_X^B$ and $E_{\tilde{S}B} = E_{\tilde{S}} - E_X^B$ are given by the eigenenergies in Eq. (C.2). For $|E - E_{T_0B}|, |E - E_{SB}| \ll |E - E_{\tilde{T}_0B}|, |E - E_{\tilde{S}B}|$, Eq. (5.24) simplifies to Eq. (5.21). In order to calculate $\theta_F(E)$ for arbitrary energies E, also virtual transitions to $|B_+B_-\rangle$,$|\widetilde{B_+B_-}\rangle$, and the vacuum state $|0\rangle$ have to be taken into account. The corresponding expression is omitted here, but can be directly obtained from Eq. (5.5).

Above, we have only considered $t_c \neq 0$ and $t_v = 0$, i.e., a scenario in which electrons in the valence band remain localized in the quantum dots while electrons in conduction-band states can be transferred. The case $t_v \neq 0$ and $t_c = 0$ can be mapped onto the problem discussed above by mapping electrons onto holes, i.e., by interchanging c and v in above expressions. In particular, Eqs. (5.21) and (5.22) remain valid if the transfer probabilities for electrons are replaced by the corresponding values for holes, e.g., $p_{A\to B} = [t_c/(\delta E_v + U_A)]^2$, and the energy eigenvalues are calculated for transfer in the valence band rather than in the conduction band.

In the limit of small dots with similar sizes, $U_{A,B} \gg t_{c,v} \gg \delta E_c, |\delta E_v|$, configurations in which electrons and holes occupy different quantum dots are strongly suppressed. If $t_{c,v}/U_{A,B} \simeq 0$ but $t_c t_v/U_{A,B}\left(E_X^{A(0)} - E_X^{B(0)}\right)$ remains finite, a joint transfer of electron and hole via a virtual intermediate state is possible. Evidence for this coherent delocalization of an exciton has been reported for dots of similar sizes [138, 142]. The observation of incoherent exciton tunneling between quantum dots has also been reported [197, 198, 199, 200].

5.5 Doping of coupled quantum dots

In the last section, we have analyzed the Faraday rotation angle $\theta_F(E)$ for an initial spin population created by optical pumping, the method used in Ref. [70]. We now calculate $\theta_F(E)$ for the case that the initial spin density is carried by an excess electron rather than the exciton. Spin injection could be achieved, e.g., by doping one CdSe quantum dot with a single donor atom or by electrical injection [201]. For a chemical potential $E_c^B \leq \mu \leq E_c^A, E_c^B + U_B$, the conduction band level of dot B is filled with one electron while dot A remains empty. The excess electron can be spin

polarized by cooling in presence of a magnetic field. Again, we set $t_v = 0$ to keep our results transparent.

The transfer matrix element for the conduction band level leads to the delocalization of the excess electron in quantum dot B,

$$|e_{B,\sigma}\rangle = \left[1 + \left(\frac{t_c}{\delta E_c}\right)^2\right]^{-1/2} \left(\hat{c}^{B\dagger}_{c,\sigma} - \frac{t_c}{\delta E_c}\hat{c}^{A\dagger}_{c,\sigma}\right)|0\rangle \tag{5.25}$$

with eigenenergy $E^B = E^B_c - t_c^2/\delta E_c$. Note that the energy shift is different from the one found for the exciton because there is no Coulomb attraction between electron and hole in the present case.

We calculate the Faraday rotation angle for an initial state $|e_{B,+}\rangle$ and probe energy $E \simeq E^A_X$. Similar to the analysis in Section 5.4, three intermediate states dominate the spectral representation for $\theta_F(E)$. These states are the following. First, the state

$$|A_+B^-_+\rangle = \hat{c}^{A\dagger}_{c,+}\hat{c}^{B\dagger}_{c,+}\hat{c}^{A}_{v,+}|0\rangle \tag{5.26}$$

with energy eigenvalue

$$E_{A_+B^-_+} = E^{A(0)}_X + E^B_c \tag{5.27}$$

is populated by creation of an exciton with conduction and valence band spins $s_z = 1/2$ and $j_z = 3/2$, respectively[1]. Then, virtual creation of an exciton with $s_z = -1/2$ and $j_z = -3/2$ leads to transitions to the spin triplet and singlet states

$$|T^-_0\rangle = \frac{1}{\sqrt{2}}\left(\hat{c}^{A\dagger}_{c,-}\hat{c}^{B\dagger}_{c,+} + \hat{c}^{A\dagger}_{c,+}\hat{c}^{B\dagger}_{c,-}\right)\hat{c}^{A}_{v,-}|0\rangle \tag{5.28a}$$

$$|S^-\rangle \propto \frac{1}{\sqrt{2}}\left(\hat{c}^{A\dagger}_{c,-}\hat{c}^{B\dagger}_{c,+} - \hat{c}^{A\dagger}_{c,+}\hat{c}^{B\dagger}_{c,-}\right)\hat{c}^{A}_{v,-}|0\rangle + \sqrt{2}\left(\frac{t_c}{\delta E_c}\hat{c}^{A\dagger}_{c,+}\hat{c}^{A\dagger}_{c,-} - \frac{t_c}{\delta E_c - U_A - U_B}\hat{c}^{B\dagger}_{c,+}\hat{c}^{B\dagger}_{c,-}\right)\hat{c}^{A}_{v,-}|0\rangle, \tag{5.28b}$$

where the normalization constant for $|S^-\rangle$ is determined by $\langle S^-|S^-\rangle = 1$. The eigenenergies

$$E_{T^-_0} = E^{A(0)}_X + E^B_c, \tag{5.29a}$$

$$E_{S^-} = E^{A(0)}_X + E^B_c + 2t_c^2\left(\frac{1}{\delta E_c - U_A - U_B} - \frac{1}{\delta E_c}\right) \tag{5.29b}$$

are split by the exchange coupling of the conduction-band levels. Further, there are several states with energies differing from $E^{A(0)}_X + E^B_c$ (see Appendix D). For probe pulse energies $E \simeq E^{A(0)}_X$ and $|\delta E_v + U_A - U_B| \gtrsim \Gamma$, $\theta_F(E)$ is dominated by virtual

[1]The superscript distinguishes the states with two electrons and one hole from the two-exciton states discussed in Section 5.4.

excitations into the states $|A_+B_+^-\rangle$, $|T_0^-\rangle$, and $|S^-\rangle$. In this case, all other energy eigenstates with two conduction-band electrons and one hole listed in Appendix D are energetically far off resonance and can be neglected.

The transition matrix elements of the polarization operators $\hat{P}_\pm$ between $|e_{B,+}\rangle$ and the states Eqs. (5.26) and (5.28) are readily evaluated. The probabilities for electron transfer between the quantum dots are now given by

$$p_{B\to A}^- = \left(\frac{t_c}{\delta E_c}\right)^2, \tag{5.30a}$$

$$p_{A\to B}^- = \left(\frac{t_c}{\delta E_c - U_A - U_B}\right)^2. \tag{5.30b}$$

Then,

$$|\langle A_+B_+^-|\hat{P}_+|e_{B,+}\rangle|^2 = \left(1-p_{B\to A}^-\right) d_A^2, \tag{5.31a}$$

$$|\langle T_0^-|\hat{P}_-|e_{B,+}\rangle|^2 = \frac{1-p_{B\to A}^-}{2} d_A^2, \tag{5.31b}$$

$$|\langle S^-|\hat{P}_-|e_{B,+}\rangle|^2 = \frac{1+p_{B\to A}^- - 2p_{A\to B}^-}{2} d_A^2. \tag{5.31c}$$

Inserting these matrix elements into Eq. (5.5), the spectral representation of $\theta_F(E)$, we find for the Faraday rotation angle

$$\theta_F(E) = \frac{CEd_A^2}{2}\left[\left(1-p_{B\to A}^-\right)\frac{E-E_{T_0B}^-}{(E-E_{T_0B}^-)^2+\Gamma^2} - \left(1+p_{B\to A}^- - 2p_{A\to B}^-\right)\frac{E-E_{SB}^-}{(E-E_{SB}^-)^2+\Gamma^2}\right] \tag{5.32}$$

for probe energies $E \simeq E_X^{A(0)}$, in close analogy to Eq. (5.21) for optical spin injection. The energy differences are defined by $E_{T_0B}^- = E_{T_0^-} - E^B$ and $E_{SB}^- = E_{S^-} - E^B$. Because of the exchange splitting between $|T_0^-\rangle$ and $|S^-\rangle$, $\theta_F(E)$ will in general exhibit several peaks and lack point inversion symmetry. The functional dependence on probe energy is determined by the transfer probabilities and the energy differences $E_{T_0B}^-$ and E_{SB}^-. See Appendix D for a more detailed analysis which takes into account all finite transition matrix elements up to $\mathcal{O}(t_c^2)$.

Experiments on doped quantum dots could provide valuable information supplementing the experimental data obtained for optical pumping. The main advantage over optical spin injection is that spin decoherence times are expected to be substantially longer because they are not limited by electron-hole recombination. Even more importantly, Faraday rotation measurements on doped coupled quantum dots can clarify whether spin transfer occurs predominantly between the conduction or valence band levels because, for $t_c = 0$ and $t_v \neq 0$, $\theta_F(E) \simeq 0$ for probe energies $E \simeq E_X^{A(0)}$.

5.6 Comparison with experiment

In order to compare the results of Section 5.4 with experimental data from Ref. [70], we first provide numerical values for δE_c, δE_v, U_A, and U_B. The energy level spectrum of CdSe quantum dots is well established both experimentally and theoretically [202, 203]. The absorption energies $E_X^{A(0)} = 2.41\,\mathrm{eV}$ and $E_X^{B(0)} = 2.06\,\mathrm{eV}$ in Ref. [70] are consistent with $r_A \simeq 2.0\,\mathrm{nm}$ and $r_B \simeq 3.5\,\mathrm{nm}$, and we will use these radii for the following calculations. From Ref. [202], $\delta E_c \simeq 0.30\,\mathrm{eV}$ and $\delta E_v \simeq -0.10\,\mathrm{eV}$.

From the bulk values for the static dielectric constant, $\epsilon = 9.7$, and the band masses in the conduction and valence band, $m_c/m_e = 0.12$ and $m_v/m_e = 0.45$, one obtains the exciton radius 5.4 nm [204, 205, 206, 189]. The exciton radius is larger than $r_{A,B}$, and electrons and holes are strongly confined in the quantum dots as assumed in Eq. (5.1). The characteristic energy scale of the Coulomb interaction is $U_\nu \simeq e^2/4\pi\epsilon\epsilon_0 r_\nu$. For the given values of r_A and r_B, $U_A = 0.07\,\mathrm{eV}$ and $U_B = 0.04\,\mathrm{eV}$.

The Hamiltonian Eq. (5.1) does not take into account biexciton shifts, the exciton fine structure, and inter-dot Coulomb interactions. For CdSe quantum dots with radii 1.5–4 nm, the biexciton shift is of order 0.01–0.02 eV (Ref. [207]) and the characteristic energy splitting between bright and dark excitons is smaller than 0.01 eV [208]. The characteristic energy scale for inter-dot Coulomb interactions is $U_{AB} \simeq e^2/4\pi\epsilon_0\epsilon(r_A + r_B) \leq 0.03\,\mathrm{eV}$. However, it is relevant only if neither of the two quantum dots is electrically neutral. The most important effect of the inter-dot Coulomb interaction is to lower the energy eigenvalues of $|\tilde{T}_0\rangle$ and $|\tilde{S}\rangle$ [Eq. (C.1)] by U_{AB}. All these energy scales are small compared to the level broadening Γ and can safely be neglected.

In the following, we assume that only electrons in conduction band levels are transferred between the quantum dots while valence band electrons remain localized. As discussed in Section 5.5, this assumption can be tested by experiments on doped quantum dots. Mediated by electron transfer through the molecular bridge, the lowest conduction band level in dot B hybridizes with the lowest conduction band level in dot A. Comparing the observed energy shift $E_X^B - E_X^{B(0)} = -0.02\,\mathrm{eV}$ with Eq. (5.12), we find

$$t_c = \sqrt{\left(E_X^{B(0)} - E_X^B\right)(\delta E_c + U_B)} = 0.082\,\mathrm{eV}. \tag{5.33}$$

Our theory predicts that the exciton absorption peak for dot A is shifted to larger energies for the coupled quantum dots, in contrast to the experimental result $E_X^A - E_X^{A(0)} < 0$. The most likely explanation for this is that the lowest conduction band level in dot A hybridizes[2] also with higher excited levels in dot B which are nearly degenerate with E_c^A. In order to account for quantitative changes effected by this hybridization, the energy $E_X^{A(0)}$ must be replaced by the true value of the hybridized

[2]This hybridization with higher lying levels in quantum dot B does not invalidate our calculation of the Faraday rotation angle in Section 5.4 because the pump pulse leads to occupation of the lowest conduction-band level in quantum dot B only.

state in all expressions for the two-exciton eigenenergies. This value can be obtained from $E_X^{A(0)} + t_c^2/(\delta E_c + U_A) \simeq 2.36\,\mathrm{eV}$, where the latter is the experimental value for the exciton absorption edge of dot A in the coupled quantum dots. Hence, $E_X^{A(0)} \to 2.33\,\mathrm{eV}$.

From these parameters, we calculate for the transfer probabilities between the lowest conduction band states $p_{A\to B} = 0.13$ and $p_{B\to A} = 0.06$. The energy differences between the two-exciton states and the initial state are $E_{T_0 B} = 2.35\,\mathrm{eV}$, $E_{SB} = 2.37\,\mathrm{eV}$, $E_{\tilde{T}_0 B} = 2.32\,\mathrm{eV}$, $E_{\tilde{S}B} = 2.31\,\mathrm{eV}$. The oscillator strength for exciton creation, proportional to $d_{A,B}^2$, is independent of the quantum dot size in the strong confinement regime and proportional to the quantum dot volume for weak confinement. Because both dots are close to the strong confinement limit, we assume a weak scaling $d_B^2/d_A^2 = 2$ for the following Figures.

In Figure 5.5(a), we show the Faraday rotation angle calculated from Eq. (5.22) as a function of probe energy for different values of Γ, $\Gamma = 0.05\,\mathrm{eV}$ (solid), $\Gamma = 0.02\,\mathrm{eV}$ (dashed), and $\Gamma = 0.08\,\mathrm{eV}$ (dotted). We note that even qualitative features depend strongly on the microscopic parameters such as Γ. For small Γ, additional peaks emerge because the contributions from the individual two-exciton states can be resolved.

In spite of the dependence on microscopic parameters, some pronounced features in $\theta_F(E)$ are generally present:

(i) $\theta_F(E)$ does not exhibit point-inversion symmetry, in stark contrast to the Faraday rotation angle expected from virtual transitions to a single state.

(ii) θ_F has in general more than two maxima or minima. The positions and heights of the extrema are determined by the interplay of the transfer probabilities $p_{A\to B}$ and $p_{B\to A}$, and the energy splittings between the different two-exciton states. Experiments have demonstrated the strong dependence of the Faraday rotation angle on the probe energy E, including a fine structure of the resonance [209].

In Figure 5.5(b), we compare the calculated Faraday rotation signal for coupled quantum dots A and B with the corresponding result for uncoupled quantum dots A pumped at resonance. For a probe energy $E \simeq 2.42\,\mathrm{eV}$, the Faraday rotation signal for coupled dots A and B is significantly smaller than the Faraday rotation signal of the AA system, consistent with experimental observations [70].

So far, we have assumed that the symmetry axis of the CdSe quantum dots with hexagonal crystal structure is parallel to the propagation direction of pump and probe laser pulses. However, in experiment the dots are randomly oriented. We discuss next how the random orientation changes our results. The propagation direction of pump and probe laser pulse is $\hat{\mathbf{z}}$, the polarization vector of the probe pulse $\hat{\mathbf{x}}$, and the symmetry axes of quantum dots A and B are denoted by $\hat{\mathbf{c}}_A$ and $\hat{\mathbf{c}}_B$, respectively. We define the azimuthal angles $\phi_A = \angle(\hat{\mathbf{x}}, \hat{\mathbf{c}}_A)$ and $\phi_B = \angle(\hat{\mathbf{x}}, \hat{\mathbf{c}}_B)$, and the angle enclosed by the two symmetry axes $\phi_{AB} = \angle(\hat{\mathbf{c}}_A, \hat{\mathbf{c}}_B)$, see Figure 5.6(a). The conduction band spin eigenstates with quantization axis $\hat{\mathbf{c}}_{A,B}$ are denoted by $|\uparrow_{A,B}\rangle$ and $|\downarrow_{A,B}\rangle$.

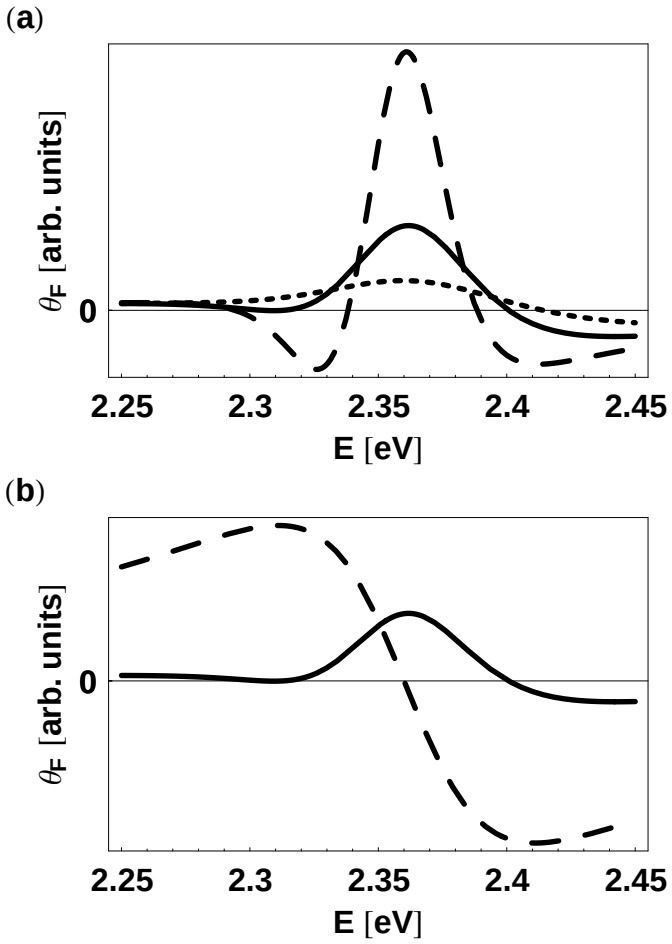

Figure 5.5: (a) Plot of the Faraday rotation angle as a function of probe pulse frequency calculated from Eq. (5.22) for different level broadenings $\Gamma = 0.05\,\mathrm{eV}$ (solid), $0.02\,\mathrm{eV}$ (dashed), and $0.08\,\mathrm{eV}$ (dotted). All other parameters are as described in the text. For small Γ, $\theta_F(E)$ clearly shows the individual contributions from the various two-exciton states. (b) Comparison of the Faraday rotation angle for coupled quantum dots for $\Gamma = 0.05\,\mathrm{eV}$ (solid) with the calculated signal for a AA structure (dashed).

For arbitrary angle $\angle(\hat{\mathbf{z}}, \hat{\mathbf{c}}_B)$, the probability for the circularly polarized pump pulse to create a net spin polarization in the conduction band level decreases from its maximum value at $\angle(\hat{\mathbf{z}}, \hat{\mathbf{c}}_B) = 0$ to zero at $\angle(\hat{\mathbf{z}}, \hat{\mathbf{c}}_B) = \pi/2$. For $\angle(\hat{\mathbf{z}}, \hat{\mathbf{c}}_B) < \pi/2$, the majority of conduction band electrons is in spin state $|\uparrow_B\rangle$, with the quantization axis defined by $\hat{\mathbf{c}}_B$. On transfer to dot A, the conduction band electron retains its spin state because states with $s_z = \pm 1/2$ are degenerate in both quantum dots and t_c is spin-independent. The characteristic level spacing of valence band states is large compared to the crystal field splitting in bulk CdSe, which allows us to treat the latter as a small perturbation, following Ref. [207].

In the following, we calculate the Faraday rotation angle for a random orientation of the quantum dots assuming that the pump pulse has created a conduction band electron with spin $|\uparrow_B\rangle$. The random orientation of quantum dots affects the Faraday rotation of the probe pulse in two ways. Firstly, the matrix elements for transitions from the $j_z = \pm 3/2$ valence band levels to the $s_z = \pm 1/2$ conduction band levels in quantum dot A (B) decrease by $\sin\phi_A$ ($\sin\phi_B$) compared to the oriented sample [207]. More importantly, also the relative orientation of $\hat{\mathbf{c}}_A$ and $\hat{\mathbf{c}}_B$ modifies the Faraday rotation angle. For illustration, consider two quantum dots with $t_c = 0$, and a conduction band electron in spin state $|\uparrow_B\rangle$ in B. The σ^- circularly polarized component of the probe pulse with $E \simeq E_X^A$ excites a virtual exciton in A, with a conduction band electron in spin state $|\uparrow_A\rangle$. Note that the spin direction is defined by $\hat{\mathbf{c}}_A$, the symmetry axis of A. Expanding $|\uparrow_A\rangle = \cos(\phi_{AB}/2)|\uparrow_B\rangle + i\sin(\phi_{AB}/2)|\downarrow_B\rangle$ in terms of the eigenstates along quantization axis $\hat{\mathbf{c}}_B$, the product state of the two excitons contains terms in which the two conduction band spins are antiparallel and have a finite overlap with the spin singlet state. This is in stark contrast to the oriented sample, where the two conduction band electrons would always form a triplet.

The analogous analysis for coupled quantum dots must take into account both the reduced transition matrix elements for the probe pulse and the relative orientation of quantum dots A and B. Because virtual transitions to $|\tilde{T}_0\rangle$ and $|\tilde{S}\rangle$ involve excitation of quantum dot B which was populated by the pump pulse, the matrix elements in Eq. (5.23) are reduced by a factor $|\sin\phi_B|$ which is independent of the relative orientation of $\hat{\mathbf{c}}_A$ and $\hat{\mathbf{c}}_B$. In contrast, virtual transitions in quantum dot A probe the spin polarization relative to the quantization axis $\hat{\mathbf{c}}_A$ after an electron with spin pointing along $\hat{\mathbf{c}}_B$ has been transferred, and the transition matrix elements depend also on ϕ_{AB}, see Figure 5.6(b). For the Faraday rotation angle, we find

$$\begin{aligned}\theta_F(E) \;=\; & \frac{CE}{2}\left\{ d_A^2 \cos\phi_{AB}\,\sin^2\phi_A \left[(1-p_{B\to A})\,\frac{E-E_{T_0B}}{(E-E_{T_0B})^2+\Gamma^2} \right.\right. \\ & \left. - (1+p_{B\to A}-2p_{A\to B})\,\frac{E-E_{SB}}{(E-E_{SB})^2+\Gamma^2}\right] \\ & \left. - d_B^2 \sin^2\phi_B\, p_{B\to A}\left[\frac{E-E_{\tilde{T}_0B}}{(E-E_{\tilde{T}_0B})^2+\Gamma^2} + \frac{E-E_{\tilde{S}B}}{(E-E_{\tilde{S}B})^2+\Gamma^2}\right]\right\}. \end{aligned} \tag{5.34}$$

The dependence on the relative orientation of the two quantum dots, ϕ_{AB}, is readily

understood. For $\phi_{AB} = \pi/2$, the first and second term in the expression for $\theta_F(E)$ vanish because the conduction band spin created in dot B is perpendicular to the spin quantization axis in dot A. A laser pulse probing quantum dot A does not show any Faraday rotation because the net spin along $\hat{\mathbf{c}}_A$ vanishes, cf. Figure 5.6(b).

In experiment, $\hat{\mathbf{c}}_A$ and $\hat{\mathbf{c}}_B$ are randomly distributed over the unit sphere. Performing this average in Eq. (5.34), we find for the Faraday rotation angle

$$\begin{aligned}\overline{\theta_F}(E) &= \frac{CE}{2}\left\{\frac{3}{16}d_A^2\left[(1-p_{B\to A})\,\frac{E-E_{T_0B}}{(E-E_{T_0B})^2+\Gamma^2}\right.\right. \\ &\qquad \left. -(1+p_{B\to A}-2p_{A\to B})\,\frac{E-E_{SB}}{(E-E_{SB})^2+\Gamma^2}\right] \\ &\qquad \left. -\frac{2}{3}d_B^2 p_{B\to A}\left[\frac{E-E_{\tilde{T}_0B}}{(E-E_{\tilde{T}_0B})^2+\Gamma^2}+\frac{E-E_{\tilde{S}B}}{(E-E_{\tilde{S}B})^2+\Gamma^2}\right]\right\}. \end{aligned} \tag{5.35}$$

Note that the spectral weight of the last term increases compared to the oriented sample.

5.7 Conclusion

We have calculated the Faraday rotation angle for coupled quantum dots as a function of the probe pulse frequency [188]. We have considered an initial spin polarization in neutral quantum dots (created by optical pumping) and of one excess electron in the two coupled quantum dots. Our results lead us to the following conclusions.

(i) The Faraday rotation angle shows a nontrivial functional dependence on the probe energy, the details of which depend on the spin exchange energy and spin transfer probabilities, see Eq. (5.22) and Figure 5.5(a). Most notably, because several two-exciton states are separated in energy by a small spin exchange coupling, $\theta_F(E)$ is not invariant under point inversion symmetry. Measurement of $\theta_F(E)$ as a function of the probe energy would allow one to identify the contributions of the various two-exciton states that are virtually excited by the probe pulse.

(ii) Experiments on doped quantum dots would allow one to determine whether spin transfer is mediated by transfer between the conduction-band states or the valence-band states. In particular, from $\theta_F = 0$ for probe pulse energies close to the resonance of dot A one could exclude that an excess electron injected into dot B has been transferred to A. In contrast, for optical spin injection, spin could be transferred both between conduction and valence band states.

(iii) In general, measurement of the Faraday rotation signal at a given probe frequency does not provide enough information to determine spin transfer probabilities between the quantum dots. However, from the experimentally observed energy shifts, we calculate a characteristic energy scale $t_c = 0.08\,\mathrm{eV}$ for spin transfer in the conduction

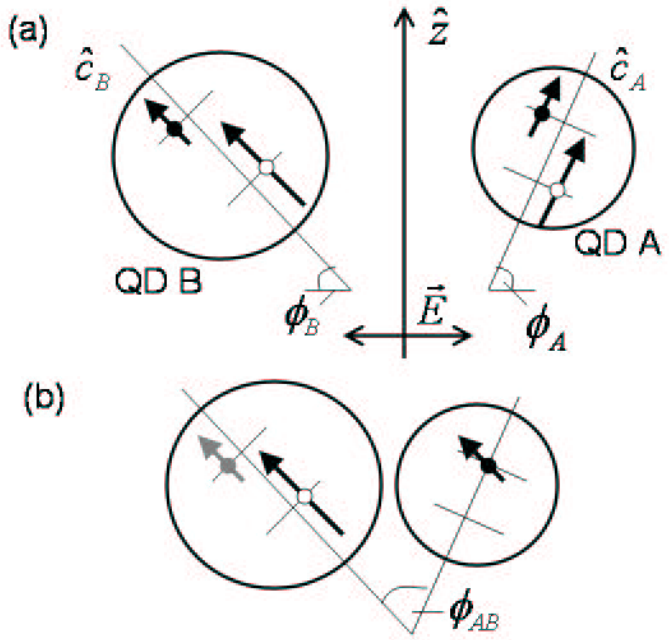

Figure 5.6: (a) The hexagonal symmetry axes of quantum dots A and B are in general oriented randomly relative to the direction of the laser pump and probe pulse. Because of the interband selection rules, a σ^- circularly polarized laser pulse generates a spin polarization along the symmetry axis of the respective dot. (b) A conduction band electron created in quantum dot B retains its spin direction on transfer to quantum dot A. Faraday rotation in dot A probes the projection of this spin onto the symmetry axis $\hat{\mathbf{c}}_A$, which gives rise to a factor $\cos\phi_{AB}$ for the first and second term in Eq. (5.34).

band. Based on the transfer Hamiltonian ansatz, this implies a probability of 6% for electron spin to be transferred from dot B to dot A, and of 13% for the opposite direction.

The purpose of this chapter was to establish the connection between spin transfer and the Faraday rotation signal observed in experiment. Our analysis was based on a transfer Hamiltonian ansatz. Some of the most interesting results of Ref. [70] remain to be explored theoretically. Most notably, the transfer Hamiltonian ansatz is based on the assumption that electrons are transferred between the quantum dots via the bridging benzene molecule. Microscopic work will have to clarify why conjugated molecules provide efficient transfer paths between quantum dots. Very recently, the spin-transfer probability in this system has been calculated atomistically using a semi-empirical tight-binding model for the quantum dots and extended Hueckel theory to treat the linking molecule Hamiltonian [210]. In this work, a striking dependence of the spin transfer on the surface site attachment and the conformation of the linking molecule has been found.

The results obtained in this chapter can also provide important guidance for the identification of microscopic transfer mechanisms. The increase of the Faraday rotation signal at a fixed probe frequency has been interpreted as an increase of the spin transfer efficiency for higher temperatures [70]. According to our results, an increase in the transfer matrix element t_c also leads to a shift of the exciton edge in absorption spectra toward lower energies. If the exciton absorption edge does not change with increasing temperature, the increased Faraday rotation signal is more likely effected, e.g., by additional incoherent transfer paths than by an increase of the transfer matrix element.

Chapter 6

Dynamics of coupled qubits in cavities

Recently, it has been shown that transmission through a detuned cavity mode can be utilized for readout of qubits [211, 212]. We show in this chapter that a similar readout scheme remains effective even for the case of qubits which are coupled by an additional interaction [213].

6.1 Cavity-QED

The optical properties of emitters such as quantum dots or atoms can be strongly modified by a cavity. A cavity imposes boundary conditions for the electromagnetic field and thus influences the photon density of states available for the emitter. This leads to the most fascinating phenomena of cavity quantum-electrodynamics (cavity QED): If the emitter is resonant with a cavity mode and is located at a suitable position in the cavity (e.g., not at a node of the electric field), then the emitter can couple much stronger to the cavity mode than to all other modes of the electromagnetic field. This leads to a strongly directional photon emission and also to an increased photon emission rate [214]. Cavities thus may significantly increase the efficiency of photon sources which is crucial, e.g., for single-photon sources. For quantum dots, several types of cavities have been fabricated, for instance microdisks, pillar microcavities (containing distributed Bragg mirrors), or defects in photonic crystals (where the photonic crystal defines a photonic bandstructure due to a periodic modulation of the refractive index, analogous to the bandstructure for electrons due to the crystal lattice). Recently, strong coupling of quantum dots and microcavities has been reported [215, 216], where energy quanta oscillate coherently between emitter and cavity mode. Thus experiments on quantum dot cavity QED have by now reached a level of quality which is comparable to that of atoms coupled with photons in cavities. The quantum-mechanical coupling of individual atoms and photons has been demon-

strated in a series of cavity-QED experiments during the last decade [97, 217, 218]. In addition to the fundamental interest in states formed by superpositions of matter and photon degrees of freedom, the development of cavity-QED has been triggered by possible applications in quantum information schemes. Strong coupling of a qubit and a cavity mode allows one to convert localized into flying qubits suitable for transmission of quantum information [219]. For several qubits interacting with one cavity mode, the cavity can act as a bus for quantum information that couples qubits with large spatial separation [220, 211].

6.2 Model

We consider a pair of qubits coupled to one cavity mode. The Hamiltonian of the system under study is given by

$$\begin{aligned} \hat{H} &= \hbar \sum_{i=1,2} \left[\Omega_i \hat{s}_{i,z} + g_i \left(\hat{a} \hat{s}_i^+ + \hat{a}^\dagger \hat{s}_i^- \right) \right] \\ &\quad + \hbar\omega \hat{a}^\dagger \hat{a} + \frac{\hbar J_\perp}{2} \left(\hat{s}_1^+ \hat{s}_2^- + \hat{s}_1^- \hat{s}_2^+ \right) + \hbar J_z \hat{s}_{1,z} \hat{s}_{2,z}. \end{aligned} \tag{6.1}$$

Here, $\hbar\Omega_i$ is the energy splitting of qubit $i = 1, 2$, $\hbar g_i$ the coupling strength with the cavity mode, $\hbar\omega$ the energy of a cavity photon, $\hat{s}_i^\pm$ are raising and lowering operators for qubit i, and $\hat{s}_{i,z} = (1/2)\sigma_{i,z}$ where $\sigma_{i,z}$ is the corresponding Pauli matrix for qubit i. Extending previous work [220, 211], we allow in the Hamiltonian Eq. (6.1) for an additional direct inter-qubit coupling mediated by $J_\perp$ and J_z. The interplay of direct and cavity-mediated coupling leads to intricate phenomena. For $J_z = J_\perp = 0$, the state of both qubits can be read out simultaneously from the cavity dispersion if $\Omega_1 \neq \Omega_2$ and the cavity Q-factor is sufficiently large [211, 212]. We show that a similar readout scheme remains effective even for the case of coupled qubits. For identical qubits with $\Omega_1 = \Omega_2$ and $g_1 = g_2$, the measurement via the cavity mode projects the coupled state onto the singlet-triplet basis and thus would allow one to detect entangled two-qubit states. We show that the direct exchange coupling modifies the cavity-mediated interactions and, for large cavity photon numbers, decreases the fidelity of cavity-mediated two-qubit gates [124, 211]. On a more fundamental level, our model allows us to investigate the transition from cavity-mediated interactions at small $J_\perp$ to a direct coupling in the presence of cavity loss and qubit decoherence. For $J_\perp = J_z = 0$, Eq. (6.1) has been derived for superconducting qubits at the charge degeneracy point interacting with a microwave resonator [211]. However, the system under consideration here has much wider applicability, including exciton states in coupled quantum dots in optical microcavities [221, 222].

6.3 Dispersive regime: qubit readout

We consider the dispersive regime, where the cavity mode is non-resonant with all transitions of the qubit system and the coupling term of cavity and qubits in Eq. (6.1) can be treated perturbatively. For a single qubit, the cavity resonance was shown theoretically [211] to shift by $\pm g^2/\Delta$, where Δ is the detuning, depending on the state of the qubit. Measurement of the cavity resonance hence provides a readout mechanism for the qubit which has been demonstrated for Cooper pair boxes at the charge degeneracy point [212]. For two qubits which are not directly coupled to each other ($J_\perp = J_z = 0$), but both of which are coupled to the cavity mode with ($g_1 = g_2 \equiv g \neq 0$), the cavity-qubit coupling can be integrated out to leading order by a Schrieffer-Wolff transformation U. The resulting effective Hamiltonian is [124, 211]

$$\begin{aligned}\hat{H} &= \hbar\left(\omega + \frac{2g^2}{\Delta_1}\hat{s}_{1,z} + \frac{2g^2}{\Delta_2}\hat{s}_{2,z}\right)\hat{a}^\dagger\hat{a} + \hbar\left(\Omega_1 + \frac{g^2}{\Delta_1}\right)\hat{s}_{1,z} \\ &\quad + \hbar\left(\Omega_2 + \frac{g^2}{\Delta_2}\right)\hat{s}_{2,z} + \frac{\hbar}{2}\left(\frac{g^2}{\Delta_1} + \frac{g^2}{\Delta_2}\right)\left(\hat{s}_1^+\hat{s}_2^- + \hat{s}_1^-\hat{s}_2^+\right),\end{aligned} \tag{6.2}$$

with $\Delta_{1,2} = \Omega_{1,2} - \omega$. Equation (6.2) implies that (i) photon emission into the qubit and subsequent absorption by the second qubit [described by the last term of Eq. (6.2)] gives rise to an effective cavity-mediated coupling; and (ii) the cavity resonance is energetically shifted relative to ω by $g^2(-\Delta_1^{-1} - \Delta_2^{-1})$, $g^2(\Delta_1^{-1} - \Delta_2^{-1})$, $g^2(-\Delta_1^{-1} + \Delta_2^{-1})$, and $g^2(\Delta_1^{-1} + \Delta_2^{-1})$ for the qubit states $|\downarrow\downarrow\rangle$, $|\uparrow\downarrow\rangle$, $|\downarrow\uparrow\rangle$, and $|\uparrow\uparrow\rangle$, respectively. In particular, for $|\Delta_1 - \Delta_2| \gg g^2|(\Delta_1^{-1} + \Delta_2^{-1})|$, spin flip-flop transitions between the qubits are weak and the cavity resonance can be used for the simultaneous readout of both qubits if the cavity loss rate is sufficiently small that all four frequencies can be resolved [211].

We now turn to the complementary limit of identical qubits, $\Omega_1 = \Omega_2 = \Omega$ and $g_1 = g_2 \equiv g$ with finite direct coupling. Because

$$\hat{N} = \hat{a}^\dagger\hat{a} + \hat{s}_{1,z} + \hat{s}_{2,z} \tag{6.3}$$

commutes with $\hat{H}$, the problem can be solved exactly by diagonalization of the Hamiltonian in the four-dimensional subspaces with given eigenvalue of $\hat{N}$. Here, we provide an analytical solution in the limit of weak coupling where the detuning of ω relative to all transitions of the coupled qubit system is large compared to $g\sqrt{N}$. For $g = 0$, $\hat{H}$ is diagonal in the singlet - triplet basis, $|S\rangle = (|\uparrow\downarrow\rangle - |\downarrow\uparrow\rangle)/\sqrt{2}$, $|T_-\rangle = |\downarrow\downarrow\rangle$, $|T_0\rangle = (|\uparrow\downarrow\rangle + |\downarrow\uparrow\rangle)/\sqrt{2}$, and $|T_+\rangle = |\uparrow\uparrow\rangle$ with energies $E_S = -J_z/4 - J_\perp/2$, $E_- = -\Omega + J_z/4$, $E_0 = -J_z/4 + J_\perp/2$, and $E_+ = \Omega + J_z/4$. We now generalize the Schrieffer-Wolff transformation of Refs. [211, 124] for finite $J_\perp$ and J_z by defining

$$\hat{H}' = U\hat{H}U^\dagger, \tag{6.4}$$

where

$$\begin{aligned} U &= e^{\hat{A}}, \\ \hat{A} &= \frac{g}{2(\Delta_-)}\left\{\hat{a}\left[\hat{s}_1^+(1-\hat{s}_{2,z})+\hat{s}_2^+(1-\hat{s}_{1,z})\right]-\text{H.c.}\right\} \\ &\quad +\frac{g}{2(\Delta_+)}\left\{\hat{a}\left[\hat{s}_1^+(1+\hat{s}_{2,z})+\hat{s}_2^+(1+\hat{s}_{1,z})\right]-\text{H.c.}\right\}, \end{aligned} \tag{6.5}$$

with $\Delta = \Omega - \omega$, $J = (J_\perp - J_z)/2$, and $\Delta_\pm = \Delta \mp J$ denotes the energy difference between the triplet state $|T_\pm\rangle$ and $|T_0\rangle$. By construction, the Schrieffer-Wolff transformation removes the cavity coupling to leading order. Expanding $\hat{H}'$ to second order in g, we find

$$\begin{aligned} \hat{H}' &= \hbar\Omega(\hat{n}+\hat{s}_{1,z}+\hat{s}_{2,z}) - \hbar\Delta\hat{n} + \frac{\hbar J_\perp}{2}\left(\hat{s}_1^+\hat{s}_2^- + \hat{s}_1^-\hat{s}_2^+\right) + \hbar J_z\hat{s}_{1,z}\hat{s}_{2,z} \\ &\quad +\frac{g^2}{2}\left(\frac{\hat{n}+1}{\Delta_+}+\frac{\hat{n}}{\Delta_-}\right)(\hat{s}_{1,z}+\hat{s}_{2,z}) \\ &\quad +\frac{g^2}{2}(2\hat{n}+1)\left(\frac{1}{\Delta_+}-\frac{1}{\Delta_-}\right)\hat{s}_{1,z}\hat{s}_{2,z} \\ &\quad +g^2\left(\frac{\hat{n}+1}{\Delta_-}-\frac{\hat{n}}{\Delta_+}\right)\left(\hat{s}_1^+\hat{s}_2^- + \hat{s}_1^-\hat{s}_2^+\right) \\ &\quad +g^2\left(\frac{1}{\Delta_+}-\frac{1}{\Delta_-}\right)\left(\hat{a}^2\hat{s}_1^+\hat{s}_2^+ + \hat{a}^{\dagger 2}\hat{s}_1^-\hat{s}_2^-\right), \end{aligned} \tag{6.6}$$

where $\hat{n} = \hat{a}^\dagger\hat{a}$ is the photon number operator. The second line of Eq. (6.6) is diagonal in the singlet-triplet basis and can be interpreted as the ac stark shift of the qubit states due to the cavity mode. The third line of Eq. (6.6) describes two-photon transitions between $|T_+\rangle$ and $|T_-\rangle$.

The expansion in g leading to Eq. (6.6) is valid as long as $g\sqrt{N} \ll |\Delta_\pm|$. Unless $g^2|\Delta_+^{-1} - \Delta_-^{-1}| \gtrsim |\Delta|$, two-photon processes described by the last term in Eq. (6.6) can be neglected. For a cavity mode detuning which is off-resonant with all transitions, Eq. (6.6) implies that the cavity resonance experiences a shift

$$\omega \to \omega + 2g^2 \times \begin{cases} 0 & \text{for } |S\rangle, \\ \Delta_+^{-1} & \text{for } |T_+\rangle, \\ \Delta_-^{-1} - \Delta_+^{-1} & \text{for } |T_0\rangle, \text{ and} \\ -\Delta_-^{-1} & \text{for } |T_-\rangle. \end{cases} \tag{6.7}$$

Similarly to two qubits with different level spacing $\Omega_1 \neq \Omega_2$ and without direct coupling, $J_\perp = J_z = 0$, the cavity resonance splits into four lines, depending on the state of the coupled qubits. In stark contrast to uncoupled qubits, however, measurement of the cavity resonance projects the qubits onto the singlet-triplet basis rather than the $\hat{s}_z$ product basis. A resonance shift by $2g^2(\Delta_-^{-1} - \Delta_+^{-1})$, corresponding to the $|T_0\rangle$ state, would indicate that the coupled qubits are in a maximally entangled

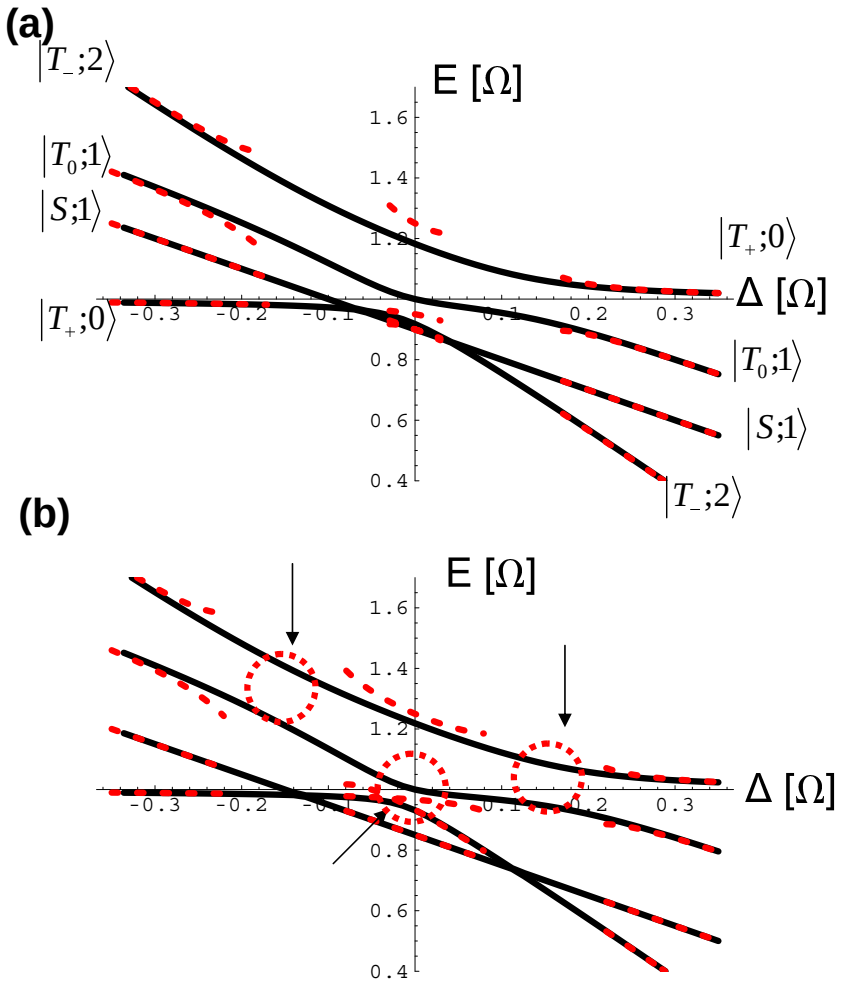

Figure 6.1: Energy level spectrum in the subspace $N = 1$ as a function of Δ for $g = 0.05\Omega$ and (a) $J = 0.1\Omega$ and (b) $J = 0.15\Omega$, respectively. Solid lines indicate the exact energy eigenvalues, dashed lines the approximate analytical values obtained with Eq. (6.6). The three anticrossings discussed in the text are indicated by arrows in (b).

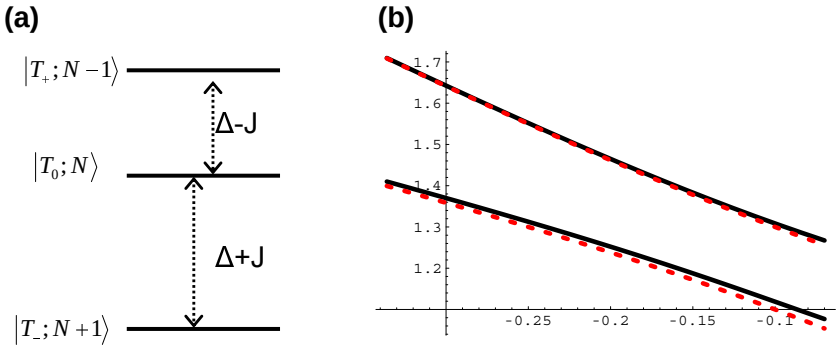

Figure 6.2: (a) Triplet level scheme. (b) Exact anticrossing (solid) in comparison with two-level description.

state. However, such a proof of entanglement would be rather indirect because it relies only on the energy levels of the system rather than on quantum state tomography.

In order to verify the range of validity of our results, we compare the spectrum determined from Eq. (6.6) in the dispersive regime with exact diagonalization. In Figure 6.1, we show the exact level spectrum (solid lines) as a function of Δ for $g = 0.05\Omega$, $J_z = 0$ and (a) $J_\perp = 0.2\Omega$ and (b) $J_\perp = 0.3\Omega$, respectively. The analytical results valid in the perturbative regime of large detuning from all resonances are indicated as dashed lines.

As evident from Figure 6.1, the expansion in g breaks down if the cavity mode approaches resonance with one of the triplet transitions. On tuning Δ, the spectrum shows three anticrossings. Two strong anticrossings with splitting $g\sqrt{2(N+1)}$ ($g\sqrt{2N}$) for $\Delta + J = 0$ ($\Delta - J = 0$), respectively, corresponding to strong mixing of the states $|T_-;N+1\rangle$ and $|T_0;N\rangle$ ($|T_0;N\rangle$ and $|T_+;N-1\rangle$) by one-photon absorption. In addition, there is a weaker anticrossing with splitting $2g^2\sqrt{N(N+1)}/J$ between $|T_-;N+1\rangle$ and $|T_+;N-1\rangle$ at $\Delta = 0$ due to two-photon absorption processes described by the last term in Eq. (6.6). In Figure 6.2, we show all relevant transitions and the exact energy eigenvalues in comparison with approximate expressions of the two-state model.

6.4 Conclusion

We have studied two coupled qubits which additionally interact with a cavity mode. A Schrieffer-Wolff transformation has been performed for the case of two identical qubits. From the transformed Hamiltonian we conclude that for weak coupling to the cavity the singlet and the three triplet states of the two-qubit system can be distinguished by the energy shift which they induce for the cavity mode, provided these

shifts are larger than the cavity linewidth. The model we have considered is applicable to different systems which are described by the Hamiltonian Eq. (6.1), including excitons in tunnel- or electrostatically coupled quantum dots that are imbedded in a microcavity, or capacitively coupled Cooper pair boxes in a microwave resonator.

Appendix A

Biexciton Coulomb matrix elements

We present the Coulomb matrix elements obtained in Chapter 3 for a biexciton or two X^+ in a double dot in the presence of a magnetic field $\mathbf{B} = B\hat{\mathbf{z}}$ and an in-plane electric field $\mathbf{E} = \varepsilon \mathbf{n}_{\|}$.

A.1 Electric field perpendicular to inter-dot axis

For an electric field $\mathbf{E} = \varepsilon\hat{\mathbf{y}}$ perpendicular to the inter-dot axis $\hat{\mathbf{x}}$, we obtain for the overlap

$$\tilde{S}_\alpha =_\alpha \langle 1|2\rangle_\alpha = \exp\left[-\frac{d^2}{x_\alpha}\left(b_\alpha - \frac{1}{b_\alpha}\right) + i\frac{a|\Delta_\alpha|}{l_B^2}\right], \tag{A.1}$$

where $x_e = 1$ and $x_h = \xi\eta$. Note that $l_B \sim 10^{-4}\text{m} \gg a, |\Delta_\alpha|$ for magnetic fields of a few Tesla and the phase of $\tilde{S}_\alpha$ can therefore safely be neglected in practice. We obtain for the symbols used in Eqs. (3.13) and (3.23) [223, 224]:

$$\begin{aligned}
E_{\alpha\alpha} &\equiv \langle 12|C_{\alpha,\alpha}|12\rangle = \langle 21|C_{\alpha,\alpha}|21\rangle \\
&= c\sqrt{\frac{b_\alpha}{x_\alpha}}\exp\left(-\frac{b_\alpha d^2}{x_\alpha}\right) I_0\left(\frac{b_\alpha d^2}{x_\alpha}\right), &\text{(A.2)}\\
\tilde{E}_{\alpha\alpha} &\equiv \langle 12|C_{\alpha,\alpha}|21\rangle = c\sqrt{\frac{b_\alpha}{x_\alpha}}\tilde{S}_\alpha \exp\left(-\frac{b_\alpha d^2}{x_\alpha}\right) I_0\left[\frac{d^2}{x_\alpha}\left(b_\alpha - \frac{1}{b_\alpha}\right)\right], &\text{(A.3)}\\
E_X(\varepsilon) &\equiv \langle 11|C_{e,h}|11\rangle = \langle 22|C_{e,h}|22\rangle = -c\sqrt{\bar{b}}\exp\left(-\frac{\bar{b}}{4}\Delta^2\right) I_0\left(\frac{\bar{b}}{4}\Delta^2\right), &\text{(A.4)}
\end{aligned}$$

$$
\begin{aligned}
E_{eh}(\varepsilon) &\equiv \langle 12|C_{e,h}|12\rangle = \langle 21|C_{e,h}|21\rangle \\
&= -c\sqrt{\bar{b}}\,\exp\left[-\frac{\bar{b}}{4}\left(4d^2+\Delta^2\right)\right] I_0\left[\frac{\bar{b}}{4}\left(4d^2+\Delta^2\right)\right], \qquad \text{(A.5)} \\
\tilde{E}_{X\alpha}(\varepsilon) &\equiv \left\{ \begin{array}{ll} 2\mathrm{Re}\langle 11|C_{e,h}|21\rangle = 2\mathrm{Re}\langle 22|C_{e,h}|12\rangle & \text{for } \alpha = e \\ 2\mathrm{Re}\langle 11|C_{e,h}|12\rangle = 2\mathrm{Re}\langle 22|C_{e,h}|21\rangle & \text{for } \alpha = h \end{array} \right\} \\
&= -2c\sqrt{\bar{b}}\,\mathrm{Re}\left\{\tilde{S}_\alpha \exp\left[-\frac{\bar{b}}{4}\left(\frac{d^2}{b_\alpha^2}+\Delta^2-2i\frac{d\Delta}{b_\alpha}\sqrt{b_\alpha^2-1}\right)\right]\right. \\
&\qquad \left.\times I_0\left[\frac{\bar{b}}{4}\left(\frac{d^2}{b_\alpha^2}+\Delta^2-2i\frac{d\Delta}{b_\alpha}\sqrt{b_\alpha^2-1}\right)\right]\right\}, \qquad \text{(A.6)} \\
\tilde{E}_{Xeh}(\varepsilon) &\equiv \mathrm{Re}\langle 11|C_{e,h}|22\rangle + \mathrm{Re}\langle 21|C_{e,h}|12\rangle \\
&= -c\sqrt{\bar{b}}\,\mathrm{Re}\left\{\tilde{S}_e\tilde{S}_h \exp\left[\frac{1}{\bar{b}}\left(\frac{d}{b_e}\sqrt{b_e^2-1}+\frac{i}{2}\bar{b}\Delta\right)^2\right]\right. \\
&\qquad \left.\times I_0\left[\frac{1}{\bar{b}}\left(\frac{d}{b_e}\sqrt{b_e^2-1}+\frac{i}{2}\bar{b}\Delta\right)^2\right]\right\} \\
&\quad -c\sqrt{\bar{b}}\,\mathrm{Re}\left\{\tilde{S}_e\tilde{S}_h^* \exp\left[\frac{1}{\bar{b}}\left(\frac{d(b_h-\xi\eta b_e)}{b_e(b_h+\xi\eta b_e)}\sqrt{b_e^2-1}+\frac{i}{2}\bar{b}\Delta\right)^2\right]\right. \\
&\qquad \left.\times I_0\left[\frac{1}{\bar{b}}\left(\frac{d(b_h-\xi\eta b_e)}{b_e(b_h+\xi\eta b_e)}\sqrt{b_e^2-1}+\frac{i}{2}\bar{b}\Delta\right)^2\right]\right\}. \qquad \text{(A.7)}
\end{aligned}
$$

In the matrix elements of $C_{\alpha,\beta}$ above, the index α refers to the first entry in the bra and the ket, and β refers to the second entry. Further, $I_0(x)$ is the zeroth-order modified Bessel function, $c = e^2\sqrt{\pi/2}\,/\kappa a_e\hbar\omega_e$ is a dimensionless parameter characterizing the Coulomb interaction, $\Delta = (|\Delta_e|+|\Delta_h|)/a_e$, and $\bar{b} = 2b_eb_h/(b_h+\xi\eta b_e)$. In the Coulomb energies Eqs. (3.13) and (3.23) we have used $|\tilde{S}_\alpha|^2 = S_\alpha^2$. The correct expressions for the Coulomb energies Eqs. (3.13) and (3.23) are obtained after setting $\tilde{S}_\alpha \to S_\alpha$ in above matrix elements, as discussed above.

A.2 Electric field parallel to inter-dot axis

For an in-plane electric field $\mathbf{E} = \varepsilon\hat{\mathbf{x}}$ parallel to the inter-dot axis, the Coulomb matrix elements Eqs. (A.2)–(A.4) are unchanged, whereas Eqs. (A.5)–(A.7) are replaced by [223, 224]

$$
\begin{aligned}
E_{eh}(\varepsilon) &\equiv \frac{1}{2}\left(\langle 12|C_{e,h}|12\rangle + \langle 21|C_{e,h}|21\rangle\right) \\
&= -\frac{c\sqrt{\bar{b}}}{2}\left\{\exp\left[-\frac{\bar{b}}{4}\left(2d+\Delta\right)^2\right] I_0\left[\frac{\bar{b}}{4}\left(2d+\Delta\right)^2\right]\right. \\
&\qquad \left. + \exp\left[-\frac{\bar{b}}{4}\left(2d-\Delta\right)^2\right] I_0\left[\frac{\bar{b}}{4}\left(2d-\Delta\right)^2\right]\right\}, \qquad \text{(A.8)} \\
\tilde{E}_{X\alpha}(\varepsilon) &\equiv \left\{ \begin{array}{ll} \mathrm{Re}\langle 11|C_{e,h}|21\rangle + \mathrm{Re}\langle 22|C_{e,h}|12\rangle & \text{for } \alpha = \mathrm{e} \\ \mathrm{Re}\langle 11|C_{e,h}|12\rangle + \mathrm{Re}\langle 22|C_{e,h}|21\rangle & \text{for } \alpha = \mathrm{h} \end{array} \right\} \\
&= -c\sqrt{\bar{b}}\, S_\alpha \left\{\exp\left(-\frac{\bar{b}}{4}\left[(d-\Delta)^2 - d^2\left(1-\frac{1}{b_\alpha^2}\right)\right]\right)\right. \\
&\quad \times I_0\left(\frac{\bar{b}}{4}\left[(d-\Delta)^2 - d^2\left(1-\frac{1}{b_\alpha^2}\right)\right]\right) \\
&\quad + \exp\left(-\frac{\bar{b}}{4}\left[(d+\Delta)^2 - d^2\left(1-\frac{1}{b_\alpha^2}\right)\right]\right) \\
&\quad \left. \times I_0\left(\frac{\bar{b}}{4}\left[(d+\Delta)^2 - d^2\left(1-\frac{1}{b_\alpha^2}\right)\right]\right)\right\}, \qquad \text{(A.9)} \\
\tilde{E}_{Xeh}(\varepsilon) &\equiv \mathrm{Re}\langle 11|C_{e,h}|22\rangle + \mathrm{Re}\langle 21|C_{e,h}|12\rangle \\
&= -c\sqrt{\bar{b}}\, S_e S_h \\
&\quad \times \left\{\exp\left(\frac{\bar{b}}{4}\left[d^2\left(1-\frac{1}{b_e^2}\right)\left(1+\frac{\xi\eta b_e}{b_h}\right)^2 - \Delta^2\right]\right)\right. \\
&\qquad \times I_0\left(\frac{\bar{b}}{4}\left[d^2\left(1-\frac{1}{b_e^2}\right)\left(1+\frac{\xi\eta b_e}{b_h}\right)^2 - \Delta^2\right]\right) \\
&\qquad + \exp\left(\frac{\bar{b}}{4}\left[d^2\left(1-\frac{1}{b_e^2}\right)\left(1-\frac{\xi\eta b_e}{b_h}\right)^2 - \Delta^2\right]\right) \\
&\qquad \left. \times I_0\left(\frac{\bar{b}}{4}\left[d^2\left(1-\frac{1}{b_e^2}\right)\left(1-\frac{\xi\eta b_e}{b_h}\right)^2 - \Delta^2\right]\right)\right\}. \qquad \text{(A.10)}
\end{aligned}
$$

Appendix B

Biexciton oscillator strengths

We present results for the oscillator strengths of transitions between a biexciton and an exciton in a double dot. Following Chapter 3, we consider for the biexciton the delocalized biexciton states $|IJ\rangle$ [Eq. (3.9)] and the localized biexcitons $|DDDD\rangle$. For the single-exciton state we consider a localized exciton $|DD\rangle$, a symmetric or antisymmetric delocalized exciton $|X\pm\rangle$, and a symmetric or antisymmetric delocalized carrier $\alpha = e, h$ with the other carrier localized on dot D, $|\alpha \pm D\rangle$.

For p_1 [Eq. (3.33)] with the biexciton states $|IJ\rangle$ in the presence of a magnetic field $\mathbf{B} = (0, 0, B)$ and an electric field $\mathbf{E} = \varepsilon(n_x, n_y, 0)$, we obtain

$$
\begin{aligned}
|\langle IJ|\mathbf{e}_{\mathbf{k}\lambda}\cdot\mathbf{p}|11\rangle| &= 2|M_{\sigma\lambda}(\theta,\phi)\sqrt{N_{IJ}}\left(C_{eh}\left[1+(-1)^{I+J}S_eS_h\right]\right. \\
&\quad \left.+(-1)^I S_e S_{eh1}+(-1)^J S_h S_{eh2}\right)|, \qquad \text{(B.1)}\\
|\langle IJ|\mathbf{e}_{\mathbf{k}\lambda}\cdot\mathbf{p}|22\rangle| &= 2|M_{\sigma\lambda}(\theta,\phi)\sqrt{N_{IJ}}\left(C_{eh}\left[(-1)^{I+J}+S_eS_h\right]\right. \\
&\quad \left.+(-1)^I S_h S_{eh1}+(-1)^J S_e S_{eh2}\right)|, \qquad \text{(B.2)}\\
|\langle IJ|\mathbf{e}_{\mathbf{k}\lambda}\cdot\mathbf{p}|X\pm\rangle| &= |M_{\sigma\lambda}(\theta,\phi)\sqrt{\frac{2N_{IJ}}{(1\pm S_eS_h)}} \\
&\quad \times\left[C_{eh}(1\pm(-1)^{I+J})(1\pm S_eS_h)\right. \\
&\quad \left.+(-1)^I S_{eh1}(S_e\pm S_h)+(-1)^J S_{eh2}(S_h\pm S_e)\right]|, \qquad \text{(B.3)}\\
|\langle IJ|\mathbf{e}_{\mathbf{k}\lambda}\cdot\mathbf{p}|h\pm1\rangle| &= |M_{\sigma\lambda}(\theta,\phi)\sqrt{2N_{IJ}(1\pm S_h)}\left(C_{eh}[1\pm(-1)^{I+J}S_e]\right. \\
&\quad \left.+(-1)^I S_{eh1}S_e\pm(-1)^J S_{eh2}\right)|, \qquad \text{(B.4)}\\
|\langle IJ|\mathbf{e}_{\mathbf{k}\lambda}\cdot\mathbf{p}|h\pm2\rangle| &= |M_{\sigma\lambda}(\theta,\phi)\sqrt{2N_{IJ}(1\pm S_h)}\left(C_{eh}[S_e\pm(-1)^{I+J}]\right. \\
&\quad \left.+(-1)^I S_{eh1}\pm(-1)^J S_{eh2}S_e\right)|, \qquad \text{(B.5)}\\
|\langle IJ|\mathbf{e}_{\mathbf{k}\lambda}\cdot\mathbf{p}|e\pm1\rangle| &= |M_{\sigma\lambda}(\theta,\phi)\sqrt{2N_{IJ}(1\pm S_e)}\left(C_{eh}[1\pm(-1)^{I+J}S_h]\right. \\
&\quad \left.\pm(-1)^I S_{eh1}+(-1)^J S_{eh2}S_h\right)|, \qquad \text{(B.6)}\\
|\langle IJ|\mathbf{e}_{\mathbf{k}\lambda}\cdot\mathbf{p}|e\pm2\rangle| &= |M_{\sigma\lambda}(\theta,\phi)\sqrt{2N_{IJ}(1\pm S_e)}\left(C_{eh}[S_h\pm(-1)^{I+J}]\right. \\
&\quad \left.\pm(-1)^I S_{eh1}S_h+(-1)^J S_{eh2}\right)|, \qquad \text{(B.7)}
\end{aligned}
$$

where $\Delta = (|\Delta_e| + |\Delta_h|)/a_e$. We apply the notation $C_{eh} = P_{eh}(\Delta)$ and $S_{eh1} = P_{eh}[(2d - n_x\Delta)^2 + n_y^2\Delta^2]$ and $S_{eh2} = P_{eh}[(2d + n_x\Delta)^2 + n_y^2\Delta^2]$.

For the transitions including a biexciton which is localized in one dot, we obtain

$$\langle 1111|\mathbf{e}_{\mathbf{k}\lambda}\cdot\mathbf{p}|11\rangle = 2|M_{\sigma\lambda}(\theta,\phi)|C_{eh}, \tag{B.8}$$

$$\langle 1111|\mathbf{e}_{\mathbf{k}\lambda}\cdot\mathbf{p}|22\rangle = 2|M_{\sigma\lambda}(\theta,\phi)|S_eS_hC_{eh}, \tag{B.9}$$

$$\langle 1111|\mathbf{e}_{\mathbf{k}\lambda}\cdot\mathbf{p}|X\pm\rangle = |M_{\sigma\lambda}(\theta,\phi)|\sqrt{2(1\pm S_eS_h)}\,C_{eh}, \tag{B.10}$$

$$\langle 1111|\mathbf{e}_{\mathbf{k}\lambda}\cdot\mathbf{p}|h\pm 1\rangle = |M_{\sigma\lambda}(\theta,\phi)|\sqrt{2(1\pm S_h)}\,C_{eh}, \tag{B.11}$$

$$\langle 1111|\mathbf{e}_{\mathbf{k}\lambda}\cdot\mathbf{p}|h\pm 2\rangle = |M_{\sigma\lambda}(\theta,\phi)|\sqrt{2(1\pm S_h)}\,S_eC_{eh}, \tag{B.12}$$

$$\langle 1111|\mathbf{e}_{\mathbf{k}\lambda}\cdot\mathbf{p}|e\pm 1\rangle = |M_{\sigma\lambda}(\theta,\phi)|\sqrt{2(1\pm S_e)}\,C_{eh}, \tag{B.13}$$

$$\langle 1111|\mathbf{e}_{\mathbf{k}\lambda}\cdot\mathbf{p}|e\pm 2\rangle = |M_{\sigma\lambda}(\theta,\phi)|\sqrt{2(1\pm S_e)}\,S_hC_{eh}. \tag{B.14}$$

Analogous expressions are obtained if $\langle 1111|$ is replaced by $\langle 2222|$.

Appendix C

Two-exciton eigenstates of molecularly coupled quantum dots

In order to evaluate the Faraday rotation angle $\theta_F(E)$ from Eq. (5.5) for arbitrary probe energies E, all two-exciton intermediate states $|\psi_i\rangle$ with finite transition matrix elements $\langle\psi_i|\hat{P}_\pm|X_{B,+}\rangle$ must be calculated. States with energies $E_i \simeq E + E_X^{B(0)}$ lead to the dominant contributions in the expression for the Faraday rotation angle, Eq. (5.5). The states $|A_+B_+\rangle$, $|S\rangle$, and $|T_0\rangle$ defined in Eqs. (5.13) and (5.15) have energy eigenvalues E_i with $|E_X^{A(0)} + E_X^{B(0)} - E_i| \leq \mathcal{O}[t_c^2/(\delta E_c - U_A), t_c^2/(\delta E_c + U_A)]$, and are the most important intermediate states for probe pulse energies $E \simeq E_X^{A(0)}$. However, for the experimental values of Ref. [70], $\delta E_v + U_A$ is small and two additional two-exciton states must be taken into account.

The states

$$|\tilde{T}_0\rangle = \frac{1}{\sqrt{2}}\left(\hat{c}^{A\dagger}_{c,-}\hat{c}^{B\dagger}_{c,+} + \hat{c}^{A\dagger}_{c,+}\hat{c}^{B\dagger}_{c,-}\right)\hat{c}^{B}_{v,+}\hat{c}^{B}_{v,-}|0\rangle, \tag{C.1a}$$

$$|\tilde{S}\rangle \propto \frac{1}{\sqrt{2}}\left(\hat{c}^{A\dagger}_{c,-}\hat{c}^{B\dagger}_{c,+} - \hat{c}^{A\dagger}_{c,+}\hat{c}^{B\dagger}_{c,-}\right)\hat{c}^{B}_{v,+}\hat{c}^{B}_{v,-}|0\rangle \tag{C.1b}$$

$$+\sqrt{2}\left(\frac{t_c}{\delta E_c + U_A + 2U_B}\hat{c}^{A\dagger}_{c,+}\hat{c}^{A\dagger}_{c,-} - \frac{t_c}{\delta E_c + U_B}\hat{c}^{B\dagger}_{c,+}\hat{c}^{B\dagger}_{c,-}\right)\hat{c}^{B}_{v,+}\hat{c}^{B}_{v,-}|0\rangle$$

differ from the corresponding states in Eq. (5.15) in that both holes are localized in dot B. The normalization constant for $|\tilde{S}\rangle$ is fixed by $\langle\tilde{S}|\tilde{S}\rangle = 1$. The eigenenergies

$$E_{\tilde{T}_0} = E_X^{A(0)} + E_X^{B(0)} + \delta E_v + U_A, \tag{C.2a}$$

$$E_{\tilde{S}} = E_X^{A(0)} + E_X^{B(0)} + \delta E_v + U_A \tag{C.2b}$$

$$+2t_c^2\left(\frac{1}{\delta E_c + U_B} - \frac{1}{\delta E_c + 2U_B + U_A}\right) \tag{C.2c}$$

are shifted relative to E_{T_0} and E_S by $\delta E_v + U_A$.

$\|\psi_i\rangle$	E_i	$E_i - E_X^B$ [eV]
$\|A_+B_+\rangle$	$E_X^{A(0)} + E_X^{B(0)}$	2.35
$\|T_0\rangle$	$E_X^{A(0)} + E_X^{B(0)}$	2.35
$\|S\rangle$	$E_X^{A(0)} + E_X^{B(0)}$	2.37
$\|B_+B_-\rangle$	$E_c^B - E_v^A + E_X^{B(0)}$	2.06
$\|\tilde{T}_0\rangle$	$E_c^A - E_v^B + E_X^{B(0)}$	2.32
$\|\tilde{S}\rangle$	$E_c^A - E_v^B + E_X^{B(0)}$	2.33
$\widetilde{\|B_+B_-\rangle}$	$2E_X^{B(0)}$	2.04

Table C.1: Two-exciton eigenstates $|\psi_i\rangle$ which contribute to the Faraday rotation angle up to second order in t_c. We also list the corresponding eigenenergies to $\mathcal{O}(t_c^0)$ and evaluate them for the parameters discussed in Section 5.6. As noted in the main text, the degeneracy of $|\tilde{T}_0\rangle$, $|\tilde{S}\rangle$ with $|T_0\rangle$, $|S\rangle$ is a consequence of $\delta E_v + U_A \simeq 0$ for the quantum dots used in experiment.

The state

$$\begin{aligned} \widetilde{|B_+B_-\rangle} \;\propto\; & \left[\hat{c}^{B\dagger}_{c,+}\hat{c}^{B\dagger}_{c,-} + \frac{t_c}{\delta E_c + U_B}\left(\hat{c}^{A\dagger}_{c,-}\hat{c}^{B\dagger}_{c,+} - \hat{c}^{A\dagger}_{c,+}\hat{c}^{B\dagger}_{c,-}\right)\right. \\ & \left. + \frac{2t_c^2\hat{c}^{A\dagger}_{c,+}\hat{c}^{A\dagger}_{c,-}}{(\delta E_c + U_B)(2\delta E_c + U_A + 3U_B)}\right]\hat{c}^{B}_{v,+}\hat{c}^{B}_{v,-}|0\rangle \end{aligned} \tag{C.3}$$

with

$$E_{\widetilde{B_+B_-}} = 2E_X^{B(0)} - 2\frac{t_c^2}{\delta E_c + U_B} \tag{C.4}$$

is energetically separated from E_{T_0} and E_S by $E_X^{A(0)} - E_X^{B(0)}$.

In Table C.1, we summarize all two-exciton eigenstates which contribute to the spectral representation of $\theta_F(E)$ up to order t_c^2. We also list the formal expressions for their eigenenergies to leading order $\mathcal{O}(t_c^0)$ and give the numerical values, taking into account terms up to $\mathcal{O}(t_c^2)$ for the parameters discussed in Section 5.6.

Appendix D

Eigenstates of doped molecularly coupled quantum dots

Here, we calculate eigenstates and energy eigenvalues for states with two electrons and one hole in the coupled quantum dots. These are the intermediate states $|\psi_i\rangle$ in Eq. (5.5) which have finite overlap matrix elements with $\hat{P}_\pm|e_{B,+}\rangle$ and determine the Faraday rotation angle for coupled quantum dots doped with a single excess electron.

In addition to the states $|A_+B_+^-\rangle$, $|S^-\rangle$, and $|T_0^-\rangle$ defined in Eqs. (5.26) and (5.28), five states have contributions of order t_c^2 to the Faraday rotation angle. These are

$$|B_+B_-^-\rangle \propto \left[\hat{c}^{B\dagger}_{c,+}\hat{c}^{B\dagger}_{c,-} + \frac{t_c}{\delta E_c - U_A - U_B}\left(\hat{c}^{A\dagger}_{c,-}\hat{c}^{B\dagger}_{c,+} - \hat{c}^{A\dagger}_{c,+}\hat{c}^{B\dagger}_{c,-}\right)\right]\hat{c}^{A}_{v,-}|0\rangle, \quad \text{(D.1a)}$$

$$|\widetilde{A_+B_+}^-\rangle = \hat{c}^{A\dagger}_{c,+}\hat{c}^{B\dagger}_{c,+}\hat{c}^{B}_{v,+}|0\rangle, \quad \text{(D.1b)}$$

$$|\tilde{T}_0^-\rangle = \frac{1}{\sqrt{2}}\left(\hat{c}^{A\dagger}_{c,-}\hat{c}^{B\dagger}_{c,+} + \hat{c}^{A\dagger}_{c,+}\hat{c}^{B\dagger}_{c,-}\right)\hat{c}^{B}_{v,-}|0\rangle, \quad \text{(D.1c)}$$

$$|\tilde{S}^-\rangle \propto \left[\frac{1}{\sqrt{2}}\left(\hat{c}^{A\dagger}_{c,-}\hat{c}^{B\dagger}_{c,+} - \hat{c}^{A\dagger}_{c,+}\hat{c}^{B\dagger}_{c,-}\right) + \sqrt{2}\left(\frac{t_c}{\delta E_c + U_A + U_B}\hat{c}^{A\dagger}_{c,+}\hat{c}^{A\dagger}_{c,-} - \frac{t_c}{\delta E_c}\hat{c}^{B\dagger}_{c,+}\hat{c}^{B\dagger}_{c,-}\right)\right]\hat{c}^{B}_{v,-}|0\rangle, \quad \text{(D.1d)}$$

$$|\widetilde{B_+B_-}^-\rangle \propto \left[\hat{c}^{B\dagger}_{c,+}\hat{c}^{B\dagger}_{c,-} + \frac{t_c}{\delta E_c}\left(\hat{c}^{A\dagger}_{c,-}\hat{c}^{B\dagger}_{c,+} - \hat{c}^{A\dagger}_{c,+}\hat{c}^{B\dagger}_{c,-}\right)\right]\hat{c}^{B}_{v,-}|0\rangle, \quad \text{(D.1e)}$$

with the proportionality constants chosen to ensure normalization. The correspond-

ing energy eigenvalues are

$$E_{B_+B_-^-} = 2E_c^B + U_B - E_v^A - 2\frac{t_c^2}{\delta E_c - U_A - U_B}, \tag{D.2a}$$

$$E_{\widetilde{A_+B_+}^-} = E_X^{B(0)} + E_c^A, \tag{D.2b}$$

$$E_{\tilde{T}_0^-} = E_X^{B(0)} + E_c^A, \tag{D.2c}$$

$$E_{\tilde{S}^-} = E_X^{B(0)} + E_c^A + 2t_c^2\left(\frac{1}{\delta E_c} - \frac{1}{\delta E_c + U_A + U_B}\right), \tag{D.2d}$$

$$E_{\widetilde{B_+B_-}^-} = E_X^{B(0)} + E_c^B - 2\frac{t_c^2}{\delta E_c}. \tag{D.2e}$$

From Eq. (D.1), we obtain the transition matrix elements in terms of the transfer probabilities defined in Eq. (5.30),

$$|\langle B_+B_-^-|\hat{P}_-|e_{B,+}\rangle|^2 = p_{A\to B}^- d_A^2, \tag{D.3a}$$

$$|\langle \widetilde{A_+B_+}^-|\hat{P}_+|e_{B,+}\rangle|^2 = p_{B\to A}^- d_B^2, \tag{D.3b}$$

$$|\langle \tilde{T}_0^-|\hat{P}_-|e_{B,+}\rangle|^2 = \frac{p_{B\to A}^-}{2} d_B^2, \tag{D.3c}$$

$$|\langle \tilde{S}^-|\hat{P}_-|e_{B,+}\rangle|^2 = \frac{p_{B\to A}^-}{2} d_B^2, \tag{D.3d}$$

$$|\langle \widetilde{B_+B_-}^-|\hat{P}_-|e_{B,+}\rangle|^2 = \left(1 - p_{B\to A}^-\right) d_B^2. \tag{D.3e}$$

These transition matrix elements and the eigenenergies allow one to calculate $\theta_F(E)$ for arbitrary energies. However, the states in Eq. (D.1) are offset in energy from $E_X^{A(0)} + E^B$. For probe energies $E \simeq E_X^{A(0)}$, virtual transitions to the states $|A_+B_+^-\rangle$, $|S^-\rangle$, and $|T_0^-\rangle$ are dominant, and $\theta_F(E)$ simplifies to the approximate expression given in Eq. (5.32).

In Table D.1, we list all states with two electrons and one hole which contribute to $\theta_F(E)$ up to $\mathcal{O}(t_c^2)$. We also provide the general expressions for the eigenenergies to order $\mathcal{O}(t_c^0)$ and evaluate them numerically for the parameters discussed in Section 5.6.

$\|\psi_i\rangle$	E_i	$E_i - E_c^B$ [eV]
$\|A_+B_+^-\rangle$	$E_X^{A(0)} + E_c^B$	2.34
$\|T_0^-\rangle$	$E_X^{A(0)} + E_c^B$	2.34
$\|S^-\rangle$	$E_X^{A(0)} + E_c^B$	2.36
$\|B_+B_-^-\rangle$	$2E_c^B + U_B - E_v^A$	2.19
$\|\widetilde{A_+B_-}^-\rangle$	$E_X^{B(0)} + E_c^A$	2.27
$\|\tilde{T}_0^-\rangle$	$E_X^{B(0)} + E_c^A$	2.27
$\|\tilde{S}^-\rangle$	$E_X^{B(0)} + E_c^A$	2.28
$\|\widetilde{B_+B_-}^-\rangle$	$E_X^{B(0)} + E_c^B$	2.03

Table D.1: Eigenstates $|\psi_i\rangle$ with two electrons and one hole which contribute to the Faraday rotation angle up to second order in t_c. We also list the corresponding eigenenergies to $\mathcal{O}(t_c^0)$ and evaluate them for the parameters discussed in Section 5.6.

Bibliography

[1] G. A. Prinz, Science **282**, 1660 (1998).

[2] S. A. Wolf, D. D. Awschalom, R. A. Buhrman, J. M. Daughton, S. von Molnár, M. L. Roukes, A. Y. Chtchelkanova, D. M. Treger, Science **294**, 1488 (2001).

[3] P. Grünberg, R. Schreiber, Y. Pang, M. B. Brodsky, and H. Sowers, Phys. Rev. Lett. **57**, 2442 (1986).

[4] M. N. Baibich, J. M. Broto, A. Fert, F. Nguyen Van Dau, F. Petroff, P. Eitenne, G. Creuzet, A. Friederich, and J. Chazelas, Phys. Rev. Lett. **61**, 2472 (1988).

[5] Y. K. Kato, R. C. Myers, A. C. Gossard, and D. D. Awschalom, Science **306**, 1910 (2004).

[6] S. Datta and B. Das, Appl. Phys. Lett. **56**, 665 (1990).

[7] C. H. Bennett and D. P. DiVincenzo, Nature (London) **404**, 247 (2000).

[8] M. A. Nielsen and I. L. Chuang, *Quantum Computation and Quantum Information*, Cambridge University Press (2000).

[9] *Semiconductor Spintronics and Quantum Computation*, eds. D. D. Awschalom, D. Loss, and N. Samarth. Series on Nanoscience and Technology, Springer (2002).

[10] V. Cerletti, W. A. Coish, O. Gywat, and D. Loss, Nanotechnology **16**, R27 (2005).

[11] D. Loss and D. P. DiVincenzo, Phys. Rev. A **57**, 120 (1998).

[12] D. D. Awschalom and J. M. Kikkawa, Physics Today **52**, 33 (1999).

[13] J. M. Kikkawa, I. P. Smorchkova, N. Samarath, and D. D. Awschalom, Science **277**, 1284 (1997).

[14] J. M. Kikkawa and D. D. Awschalom, Phys. Rev. Lett. **80**, 4313 (1998).

[15] J. M. Kikkawa and D. D. Awschalom, Nature (London) **397**, 139 (1999).

[16] T. Fujisawa, D. G. Austing, Y. Tokura, Y. Hirayama, and S. Tarucha, Nature (London) **419**, 278 (2002).

[17] R. Hanson, B. Witkamp, L. M. K. Vandersypen, L. H. Willems van Beveren, J. M. Elzerman, and L. P. Kouwenhoven, Phys. Rev. Lett. **91**, 196802 (2003).

[18] J. M. Elzerman, R. Hanson, L. H. Willems van Beveren, B. Witkamp, L. M. K. Vandersypen, and L. P. Kouwenhoven, Nature (London) **430**, 431 (2004).

[19] M. Kroutvar, Y. Ducommun, D. Heiss, M. Bichler, D. Schuh, G. Abstreiter, and J. J. Finley, Nature (London) **432**, 81 (2004).

[20] J. R. Petta, A. C. Johnson, A. Yacoby, C. M. Marcus, M. P. Hanson, and A. C. Gossard, cond-mat/0412048.

[21] R. Hanson, L. H. Willems van Beveren, I. T. Vink, J. M. Elzerman, W. J. M. Naber, F. H. L. Koppens, L. P. Kouwenhoven, and L. M. K. Vandersypen, cond-mat/0412768.

[22] J. A. Gupta, D. D. Awschalom, X. Peng, and A. P. Alivisatos, Phys. Rev. B **59**, R10 421 (1999).

[23] R. J. Epstein, D. T. Fuchs, W. V. Schoenfeld, P. M. Petroff, and D. D. Awschalom, Appl. Phys. Lett. **78**, 733 (2001).

[24] J. A. Gupta, D. D. Awschalom, Al. L. Efros, and A. V. Rodina, Phys. Rev. B **66**, 125307 (2002).

[25] A. S. Bracker, E. A. Stinaff, D. Gammon, M. E. Ware, J. G. Tischler, A. Shabaev, Al. L. Efros, D. Park, D. Gershoni, V. L. Korenev, and I. A. Merkulov, Phys. Rev. Lett. **94**, 047402 (2005).

[26] J. Bell, Physics **1**, 195 (1965).

[27] J. F. Clauser and A. Shimony, Rep. Prog. Phys. **41**, 1881 (1978) and References therein.

[28] J. F. Clauser, M. A. Horne, A. Shimony, and R. A. Holt, Phys. Rev. Lett. **23**, 880 (1969).

[29] A. Aspect, P. Grangier, and G. Roger, Phys. Rev. Lett. **47**, 460 (1981).

[30] A. Aspect, P. Grangier, and G. Roger, Phys. Rev. Lett. **49**, 91 (1982).

[31] A. Aspect, J. Dalibard, and G. Roger, Phys. Rev. Lett. **49**, 1804 (1982).

[32] L. Mandel and E. Wolf, *Optical Coherence and Quantum Optics*, Cambridge University Press (1995).

[33] P. G. Kwiat, K. Mattle, H. Weinfurter, A. Zeilinger, A. V. Sergienko, and Y. Shih, Phys. Rev. Lett. **75**, 4337 (1995).

[34] D. Bouwmeester, J.-W. Pan, M. Daniell, H. Weinfurter, and A. Zeilinger, Phys. Rev. Lett. **82**, 1345 (1999).

[35] J.-W. Pan, M. Daniell, S. Gasparoni, G. Weihs, and A. Zeilinger, Phys. Rev. Lett. **86**, 4435 (2001).

[36] M. Murao, D. Jonathan, M. B. Plenio, and V. Vedral, Phys. Rev. A **59**, 156 (1999).

[37] D. Bouwmeester, J.-W. Pan, K. Mattle, M. Eibl, H. Weinfurter, and A. Zeilinger, Nature (London) **390**, 575 (1997).

[38] D. Boschi, S. Branca, F. De Martini, L. Hardy, and S. Popescu, Phys. Rev. Lett. **80**, 1121 (1998).

[39] R. C. Ashoori, Nature (London) **379**, 413 (1996).

[40] S. Tarucha, D. G. Austing, T. Honda, R. J. van der Hage, and L. P. Kouwenhoven, Phys. Rev. Lett. **77**, 3613 (1996).

[41] D. Gammon, E. S. Snow, B. V. Shanabrook, D. S. Katzer, and D. Park, Science **273**, 87 (1996).

[42] D. Gammon, E. S. Snow, B. V. Shanabrook, D. S. Katzer, and D. Park, Phys. Rev. Lett. **76**, 3005 (1996).

[43] N. H. Bonadeo, J. Erland, D. Gammon, D. Park, D. S. Katzer and D. G. Steel, Science **282**, 1473 (1998).

[44] G. Chen, N. H. Bonadeo, D. G. Steel, D. Gammon, D. S. Katzer, D. Park, and L. J. Sham, Science **289**, 1906 (2000).

[45] X. Li, Y. Wu, D. Steel, D. Gammon, T. H. Stievater, D. S. Katzer, D. Park, C. Piermarocchi, and L. J. Sham, Science **301**, 809 (2003).

[46] D. Leonard, M. Krishnamurthy, C. M. Reaves, S. P. Denbaars, and P. M. Petroff, Appl. Phys. Lett. **63**, 3203 (1993).

[47] K. Eberl, M. O. Lipinski, Y. M. Manz, W. Winter, N. Y. Jin-Phillipp, and O. G. Schmidt, Physica E **9**, 164 (2001).

[48] R. J. Warburton, B. T. Miller, C. S. Dürr, C. Bödefeld, K. Karrai, J. P. Kotthaus, G. Medeiros-Ribeiro, P. M. Petroff, and S. Huant, Phys. Rev. B **58**, 16221 (1998).

[49] A. Imamoḡlu and Y. Yamamoto, Phys. Rev. Lett. **72**, 210 (1994).

[50] J. Kim, O. Benson, H. Kan, and Y. Yamamoto, Nature (London) **397**, 500 (1999).

[51] P. Michler, A. Kiraz, C. Becher, W. V. Schoenfeld, P. M. Petroff, L. Zhang, E. Hu, and A. Imamoğlu, Science **290**, 2282 (2000).

[52] C. Santori, M. Pelton, G. Solomon, Y. Dale, and Y. Yamamoto, Phys. Rev. Lett. **86**, 1502 (2001).

[53] V. Zwiller, H. Blom, P. Jonsson, N. Panev, S. Jeppesen, T. Tsegaye, E. Goobar, M. E. Pistol, L. Samuelson, and G. Björk, Appl. Phys. Lett. **78**, 2476 (2001).

[54] R. M. Thompson, R. M. Stevenson, A. J. Shields, I. Farrer, C. J. Lobo, D. A. Ritchie, M. L. Leadbeater, and M. Pepper, Phys. Rev. B **64**, R201302 (2001).

[55] Z. Yuan, B. E. Kardynal, R. M. Stevenson, A. J. Shields, C. J. Lobo, K. Cooper, N. S. Beattie, D. A. Ritchie, and M. Pepper, Science **295**, 102 (2002).

[56] E. Waks, K. Inoue, C. Santori, D. Fattal, J. Vučković, G. S. Solomon, and Y. Yamamoto, Nature (London) **420**, 762 (2002).

[57] D. Fattal, E. Diamanti, K. Inoue, and Y. Yamamoto, Phys. Rev. Lett. **92**, 037904 (2004).

[58] T. Lundstrom, W. Schoenfeld, H. Lee, and P. M. Petroff, Science **286**, 2312 (1999).

[59] T. H. Stievater, X. Li, D. G. Steel, D. Gammon, D. S. Katzer, D. Park, C. Piermarocchi, and L. J. Sham, Phys. Rev. Lett. **87**, 133603 (2001).

[60] H. Kamada, H. Gotoh, J. Temmyo, T. Takagahara, and H. Ando, Phys. Rev. Lett. **87**, 246401 (2001).

[61] H. Htoon, T. Takagahara, D. Kulik, O. Baklenov, A. L. Holmes, Jr., and C. K. Shih, Phys. Rev. Lett. **88**, 087401 (2002).

[62] A. Zrenner, E. Beham, S. Stufler, F. Findeis, M. Bichler, and G. Abstreiter, Nature (London) **418**, 612 (2002).

[63] O. Benson, C. Santori, M. Pelton, and Y. Yamamoto, Phys. Rev. Lett. **84**, 2513 (2000).

[64] E. Moreau, I. Robert, L. Manin, V. Thierry-Mieg, J. M. Gérard, and I. Abram, Phys. Rev. Lett. **87**, 183601 (2001).

[65] A. Kiraz, S. Fälth, C. Becher, B. Gayral, W. V. Schoenfeld, P. M. Petroff, L. Zhang, E. Hu, and A. Imamoğlu, Phys. Rev. B **65**, R161303 (2002).

[66] C. Santori, G. S. Solomon, M. Pelton, and Y. Yamamoto, Phys. Rev. B **66**, 045308 (2002).

[67] R. M. Stevenson, R. M. Thompson, A. J. Shields, I. Farrer, B. E. Kardynal, D. A. Ritchie, and M. Pepper, Phys. Rev. B **66**, 081302(R) (2002).

[68] V. Zwiller, P. Jonsson, H. Blom, S. Jeppesen, M. E. Pistol, L. Samuelson, A. A. Katznelson, E. Yu. Kotelnikov, V. Evtikhiev, and G. Björk, Phys. Rev. A **66**, 053814 (2002).

[69] S. M. Ulrich, S. Strauf, P. Michler, G. Bacher, and A. Forchel, Appl. Phys. Lett. **83**, 1848 (2003).

[70] M. Ouyang and D. D. Awschalom, Science **301**, 1074 (2003).

[71] V. Cerletti, O. Gywat, and D. Loss, cond-mat/0411235.

[72] G. Burkard, D. Loss, and D. P. DiVincenzo, Phys. Rev. B **59**, 2070 (1999).

[73] G. Burkard, D. Loss, and E. V. Sukhorukov, Phys. Rev. B **61**, R16 303 (2000).

[74] G. Burkard, G. Seelig, and D. Loss, Phys. Rev. B **62**, 2581 (2000).

[75] D. S. Saraga and D. Loss, Phys. Rev. Lett. **90**, 166803 (2003).

[76] P. Recher, E. V. Sukhorukov, and D. Loss, Phys. Rev. B **63**, 165314 (2001).

[77] G. B. Lesovik, T. Martin, and G. Blatter, Eur. Phys. J. B, **24**, 287 (2001).

[78] P. Recher and D. Loss, Phys. Rev. B **65**, 165327 (2002).

[79] C. Bena, S. Vishveshwara, L. Balents, and M. P. A. Fisher, Phys. Rev. Lett. **89**, 037901 (2002).

[80] V. Bouchiat, N. Chtchelkatchev, D. Feinberg, G. B. Lesovik, T. Martin and J. Torrés, Nanotechnology **14**, 77 (2003).

[81] P. Recher and D. Loss, Phys. Rev. Lett. **91**, 267003 (2003).

[82] D. S. Saraga, B. L. Altshuler, D. Loss, and R. M. Westervelt, Phys. Rev. Lett. **92**, 246803 (2004).

[83] R. Fiederling, M. Keim, G. Reuscher, W. Ossau, G. Schmidt, A. Waag, and L. W. Molenkamp, Nature (London) **402**, 787 (1999).

[84] Y. Ohno, D. K. Young, B. Beschoten, F. Matsukura, H. Ohno, and D. D. Awschalom, Nature (London) **402**, 790 (1999).

[85] Y. Chye, M. E. White, E. Johnston-Halperin, B. D. Gerardot, D. D. Awschalom, and P. M. Petroff, Phys. Rev. B **66**, R201301 (2002).

[86] C. E. Pryor and M. E. Flatté, Phys. Rev. Lett. **91**, 257901 (2003).

[87] J. Seufert, G. Bacher, H. Schömig, A. Forchel, L. Hansen, G. Schmidt, and L. W. Molenkamp, Phys. Rev. B **69**, 035311 (2004).

[88] K. Gündoğdu, K. C. Hall, T. F. Boggess, D. G. Deppe, O. B. Shchekin, Appl. Phys. Lett. **84**, 2793 (2004).

[89] J. C. Egues, G. Burkard, and D. Loss, Phys. Rev. Lett. **89**, 176401 (2002).

[90] A. Zrenner, J. Chem. Ph. **112**, 7790 (2000).

[91] D. Gammon and D. G. Steel, Physics Today, **55**, 36 (2002).

[92] G. Burkard and D. Loss, Phys. Rev. Lett. **91**, 087903 (2003).

[93] B. Ohnesorge, M. Albrecht, J. Oshinowo, A. Forchel, and Y. Arakawa, Phys. Rev. B **54**, 11 532 (1996).

[94] S. Raymond, S. Fafard, P. J. Poole, A. Wojs, P. Hawrylak, S. Charbonneau, D. Leonard, R. Leon, P. M. Petroff, and J. L. Merz, Phys. Rev. B **54**, 11 548 (1996).

[95] C. Cohen-Tannoudji, B. Diu, F. Laloë, *Quantum Mechanics Volume II*, Hermann and John Wiley & Sons, Inc. (1977).

[96] E. T. Jaynes and F. W. Cummings, Proc. IEEE **51**, 89 (1963).

[97] J. M. Raimond, M. Brune, and S. Haroche, Rev. Mod. Phys. **73**, 565 (2001).

[98] J. J. Sakurai, *Modern Quantum Mechanics, Revised Edition*, (Addison-Wesley, 1995).

[99] M. I. D'yakonov and V. I. Perel' in *Optical Orientation, Modern Problems in Condensed Matter Sciences* vol 8, F. Meyer and B. P. Zakharchenya (eds.), North Holland, Amsterdam (1984).

[100] E. L. Ivchenko and G. E. Pikus, *Superlattices and other Heterostructures*, Springer, Berlin (1995).

[101] See, e.g., P. Brick, C. Ell, S. Chatterjee, G. Khitrova, H. M. Gibbs, T. Meier, C. Sieh, and S. W. Koch, Phys. Rev. B **64**, 075323 (2001).

[102] A. Peres, *Quantum Theory: Concepts and Methods*, Kluwer (1998).

[103] H. W. van Kesteren, E. C. Cosman, W. A. J. A. van der Poel, and C. T. Foxon, Phys. Rev. B **41**, 5283 (1990).

[104] M. Bayer, G. Ortner, O. Stern, A. Kuther, A. A. Gorbunov, A. Forchel, P. Hawrylak, S. Fafard, K. Hinzer, T. L. Reinecke, S. N. Walck, J. P. Reithmaier, F. Klopf, and F. Schäfer, Phys. Rev. B **65**, 195315 (2002).

[105] J. J. Finley, D. J. Mowbray, M. S. Skolnick, A. D. Ashmore, C. Baker, A. F. G. Monte, and M. Hopkinson, Phys. Rev. B **66**, 153316 (2002).

[106] A. Högele, S. Seidl, M. Kroner, K. Karrai, R. J. Warburton, B. D. Gerardot, and P. M. Petroff, Phys. Rev. Lett. **93**, 217401 (2004).

[107] V. D. Kulakovskii, G. Bacher, R. Weigand, T. Kümmel, A. Forchel, E. Borovitskaya, K. Leonardi, and D. Hommel, Phys. Rev. Lett. **82**, 1780 (1999).

[108] T. Takagahara, Phys. Rev. B **62**, 16 840 (2000).

[109] P. Borri, W. Langbein, S. Schneider, U. Woggon, R. L. Sellin, D. Ouyang, and D. Bimberg, Phys. Rev. Lett. **87**, 157401 (2001).

[110] T. M. Stace, G. J. Milburn, and C. H. W. Barnes, Phys. Rev. B **67**, 085317 (2003).

[111] Y. Oka, S. Permogorov, R. Pittini, J. X. Shen, K. Kayanuma, A. Reznitsky, L. Tenishev, and S. Verbin, Physica E **10**, 315 (2001).

[112] T. H. Stievater, X. Li, T. Cubel, D. G. Steel, D. Gammon, D. S. Katzer, and D. Park, Appl. Phys. Lett. **81**, 4251 (2002).

[113] E. Tsitsishvili, R. v. Baltz, and H. Kalt, Phys. Rev. B **67**, 205330 (2003).

[114] D. V. Regelman, E. Dekel, D. Gershoni, E. Ehrenfreund, A. J. Williamson, J. Shumway, A. Zunger, W. V. Schoenfeld, and P. M. Petroff, Phys. Rev. B **64**, 165301 (2001).

[115] J. J. Finley, M. Sabathil, P. Vogl, G. Abstreiter, R. Oulton, A. I. Tartakovskii, D. J. Mowbray, M. S. Skolnick, S. L. Liew, A. G. Cullis, and M. Hopkinson, Phys. Rev. B **70**, R201308 (2004).

[116] J. M. Luttinger, Phys. Rev. **102**, 1030 (1956).

[117] R. Winkler, Phys. Rev. B **70**, 125301 (2004).

[118] M. Bayer, A. Kuther, A. Forchel, A. Gorbunov, V. B. Timofeev, F. Schäfer, J. P. Reithmaier, T. L. Reinecke, and S. N. Walck, Phys. Rev. Lett. **82**, 1748 (1999).

[119] G. Bester, S. Nair, and A. Zunger, Phys. Rev. B **67**, R161306 (2003).

[120] H. Kamada, H. Gotoh, H. Ando, J. Temmyo, and T. Tamamura, Phys. Rev. B **60**, 5791 (1999).

[121] M. Paillard, X. Marie, P. Renucci, T. Amand, A. Jbeli, and J. M. Gérard, Phys. Rev. Lett. **86**, 1634 (2001).

[122] T. Flissikowski, A. Hundt, M. Lowisch, M. Rabe, and F. Henneberger, Phys. Rev. Lett. **86**, 3127 (2001).

[123] A. Imamoḡlu, private communication.

[124] A. Imamoḡlu, D. D. Awschalom, G. Burkard, D. P. DiVincenzo, D. Loss, M. Sherwin, and A. Small, Phys. Rev. Lett. **83**, 4204 (1999).

[125] A. Högele, M. Kroner, S. Seidl, K. Karrai, M. Atatüre, J. Dreiser, A. Imamoḡlu, R. J. Warburton, A. Badolato, B. D. Gerardot, and P. M. Petroff, cond-mat/0410506.

[126] L. Banyai, Y. Z. Hu, M. Lindberg, and S. W. Koch, Phys. Rev. B **38**, 8142 (1988).

[127] T. Takagahara, Phys. Rev. B **39**, 10 206 (1989).

[128] G. W. Bryant, Phys. Rev. B **41**, 1243 (1990).

[129] Y. Z. Hu, S. W. Koch, M. Lindberg, N. Peyghambarian, E. L. Pollock, and F. F. Abraham, Phys. Rev. Lett. **64**, 1805 (1990).

[130] Y. Z. Hu, M. Lindberg, and S. W. Koch, Phys. Rev. B **42**, 1713 (1990).

[131] S. V. Nair, T. Takagahara, Phys. Rev. B **55**, 5153 (1996).

[132] P. Hawrylak, Phys. Rev. B **60**, 5597 (1999).

[133] C. Santori, G. S. Solomon, M. Pelton, and Y. Yamamoto, Phys. Rev. B **65**, 073310 (2002).

[134] O. Gywat, G. Burkard, and D. Loss, Phys. Rev. B **65**, 205329 (2002).

[135] F. Troiani, U. Hohenester, and E. Molinari, Phys. Rev. B **62**, R2263 (2000).

[136] L. Quiroga and N. F. Johnson, Phys. Rev. Lett. **83**, 2270 (1999).

[137] A. O. Govorov, Phys. Rev. B **68**, 075315 (2003); **71**, 155323 (2005).

[138] G. Schedelbeck, W. Wegscheider, M. Bichler, and G. Abstreiter, Science **278**, 1792 (1997).

[139] H. Heidemeyer, U. Denker, C. Müller, and O. G. Schmidt, Phys. Rev. Lett. **91**, 196103 (2003).

[140] R.J. Luyken, A. Lorke, M. Haslinger, B.T. Miller, M. Fricke, J. P. Kotthaus, G. Medeiros-Ribeiro and P. M. Petroff, Physica E **2**, 704 (1998).

[141] M. C. Bödefeld, R. J. Warburton, K. Karrai, J. P. Kotthaus, G. Medeiros-Ribeiro, and P. M. Petroff, Appl. Phys. Lett. **74**, 1839 (1999).

[142] M. Bayer, P. Hawrylak, K. Hinzer, S. Fafard, M. Korkusinski, Z. R. Wasilewski, O. Stern, and A. Forchel, Science **291**, 451 (2001).

[143] H. J. Krenner, M. Sabathil, E. C. Clark, A. F. Kress, D. Schuh, M. Bichler, G. Abstreiter, and J. J. Finley, Phys. Rev. Lett. **94**, 057402 (2005).

[144] G. Bester, J. Shumway, and A. Zunger, Phys. Rev. Lett. **93**, 047401 (2004).

[145] V. Fock, Z. f. Phys. **47**, 446 (1928); C. Darwin, Proc. Cambridge Philos. Soc. **27**, 86 (1930).

[146] S. Raymond, S. Studenikin, A. Sachrajda, Z. Wasilewski, S. J. Cheng, W. Sheng, P. Hawrylak, A. Babinski, M. Potemski, G. Ortner, and M. Bayer, Phys. Rev. Lett. **92**, 187402 (2004).

[147] I. Shtrichman, C. Metzner, B. D. Gerardot, W. V. Schoenfeld, and P. M. Petroff, Phys. Rev. B **65**, R081303 (2002).

[148] W. Heitler and F. London, Z. f. Phys. **44**, 455 (1927).

[149] W. F. Brinkman, T. M. Rice, and B. Bell, Phys. Rev. B **8**, 1570 (1973).

[150] O. Gywat, H.-A. Engel, D. Loss, R. J. Epstein, F. M. Mendoza, and D. D. Awschalom, Phys. Rev. B **69**, 205303 (2004).

[151] O. Gywat, H.-A. Engel, and D. Loss, (to appear in J. Supercond.) cond-mat/0408451.

[152] V. N. Golovach, A. Khaetskii, and D. Loss, Phys. Rev. Lett. **93**, 016601 (2004).

[153] A. V. Khaetskii, D. Loss, and L. Glazman, Phys. Rev. Lett. **88**, 186802 (2002).

[154] A. V. Khaetskii, D. Loss, and L. Glazman, Phys. Rev. B **67**, 195329 (2003).

[155] W. A. Coish and D. Loss, Phys. Rev. B **70**, 195340 (2004).

[156] H.-A. Engel and D. Loss, Phys. Rev. Lett. **86**, 4648 (2001).

[157] H.-A. Engel and D. Loss, Phys. Rev. B **65**, 195321 (2002).

[158] I. Martin, D. Mozyrsky, and H. W. Jiang, Phys. Rev. Lett. **90**, 018301 (2003).

[159] F. T. Charnock and T. A. Kennedy, Phys. Rev. B **64**, R041201 (2001).

[160] J. Köhler, J. A. J. M. Disselhorst, M. C. J. M. Donckers, E. J. J. Groenen, J. Schmidt, and W. E. Moerner, Nature (London) **363**, 242 (1993).

[161] J. Wrachtrup, C. von Borczyskowski, J. Bernard, M. Orrit, and R. Brown, Nature (London) **363**, 244 (1993).

[162] A. Gruber, A. Dräbenstedt, C. Tietz, L. Fleury, J. Wrachtrup, and C. von Borczyskowski, Science **276**, 2012 (1997).

[163] F. Jelezko, T. Gaebel, I. Popa, A. Gruber, and J. Wrachtrup, Phys. Rev. Lett. **92**, 076401 (2004).

[164] E. Lifshitz, I. Dag, I. D. Litvitn, and G. Hodes, J. Phys. Chem. B **102** (46), 9245 (1998).

[165] N. Zurauskiene, G. Janssen, E. Goovaerts, A. Bouwen, D. Shoemaker, P. M. Koenraad, and J. H. Wolter, phys. stat. sol. (b) **224**, 551 (2001).

[166] S. Cortez, O. Krebs, S. Laurent, M. Senes, X. Marie, P. Voisin, R. Ferreira, G. Bastard, J. M. Gérard, and T. Amand, Phys. Rev. Lett. **89**, 207401 (2002).

[167] M. Baier, F. Findeis, A. Zrenner, M. Bichler, and G. Abstreiter, Phys. Rev. B **64**, 195326 (2001).

[168] C. Schulhauser, R. J. Warburton, A. Högele, K. Karrai, A. O. Govorov, J. M. Garcia, B. D. Gerardot and P. M. Petroff, Physica E **21**, 184 (2004).

[169] J. G. Tischler, A. S. Bracker, D. Gammon, and D. Park, Phys. Rev. B **66**, 081310 (2002).

[170] A. Shabaev, Al. L. Efros, D. Gammon, and I. A. Merkulov, Phys. Rev. B **68**, 201305 (2004).

[171] Al. L. Efros, Phys. Rev. B **46**, 7448 (1992).

[172] Al. L. Efros and A. V. Rodina, Phys. Rev. B **47**, 10 005 (1993).

[173] M. Fricke, A. Lorke, J. P. Kotthaus, G. Medeiros-Ribeiro, and P. M. Petroff, Europhys. Lett. **36**, 197 (1996).

[174] Y. Kato, R. C. Myers, D. C. Driscoll, A. C. Gossard, J. Levy, and D. D. Awschalom, Science **299**, 1201 (2003).

[175] H. J. Carmichael, *Statistical Methods in Quantum Optics 1*, Springer (1999).

[176] C. W. Gardiner and P. Zoller, *Quantum Noise*, Springer (2000).

[177] M. E. Schmidt, S. A. Blanton, M. A. Hines, and P. Guyot-Sionnest, Phys. Rev. B **53**, 12 629 (1996).

[178] A. M. van Oijen, R. Verberk, Y. Durand, J. Schmidt, J. N. J. van Lingen, A. A. van Bol, and A. Meijerink, Appl. Phys. Lett. **79**, 830 (2001).

[179] A. V. Baranov, Y. Masumoto, K. Inoue, A. V. Fedorov, and A. A. Onushchenko, Phys. Rev. B **55**, 15 675 (1997).

[180] M. Grundmann, N. N. Ledentsov, O. Stier, D. Bimberg, V. M. Ustinov, P. S. Kop'ev, and Zh. I. Alferov, Appl. Phys. Lett. **68**, 979 (1996).

[181] J. J. Finley, M. Skalitz, M. Arzberger, A. Zrenner, G. Böhm, and G. Abstreiter, Appl. Phys. Lett. **73**, 2618 (1998).

[182] F. Findeis, M. Baier, E. Beham, A. Zrenner, and G. Abstreiter, Appl. Phys. Lett. **78**, 2958 (2001).

[183] H. J. Kimble, R. J. Cook, and A. L. Wells, Phys. Rev. A **34**, 3190 (1986).

[184] T. Flissikowski, I. A. Akimov, A. Hundt, and F. Henneberger, Phys. Rev. B **68**, R161309 (2003).

[185] L. M. Woods, T. L. Reinecke, and R. Kotlyar, Phys. Rev. B **69**, 125330 (2004).

[186] J. A. Gupta, R. Knobel, N. Samarth, and D. D. Awschalom, Science **292**, 2458 (2001).

[187] C. E. Pryor and M. E. Flatté, quant-ph/0211160.

[188] F. Meier, V. Cerletti, O. Gywat, D. Loss, and D. D. Awschalom, Phys. Rev. B **69**, 195315 (2004).

[189] H. Fu, L.-W. Wang, and A. Zunger, Phys. Rev. B **59**, 5568 (1999).

[190] M. Faraday, Philos. Trans. Roy. Soc. Lond., **136**, 1 (1846).

[191] J. Berezowsky, M. Ouyang, F. Meier, D. D. Awschalom, D. Battaglia, and X. Peng, Phys. Rev. B **71**, 081309(R) (2005).

[192] S. Hugonnard-Bruyère, C. Buss, F. Vouilloz, R. Frey, and C. Flytzanis, Phys. Rev. B **50**, 2200 (1994).

[193] N. Linder and L. J. Sham, Physica E **2**, 412 (1998).

[194] L. J. Sham, Journ. Mag. Mag. Mat. **200**, 219 (1999).

[195] A. V. Rodina, Al. L. Efros, and A. Y. Alekseev, Phys. Rev. B **67**, 155312 (2003).

[196] J. Schrier and K. B. Whaley, Phys. Rev. B **67**, 235301 (2003).

[197] R. Heitz, I. Mukhametzhanov, P. Chen, and A. Madhukar, Phys. Rev. B **58**, 10 151 (1998).

[198] A. Tackeuchi, T. Kuroda, K. Mase, Y. Nakata, and N. Yokoyama, Phys. Rev. B **62**, 1568 (2000).

[199] H. D. Robinson, B. B. Goldberg, and J. L. Merz, Phys. Rev. B **64**, 075308 (2001).

[200] J. Seufert, M. Obert, G. Bacher, A. Forchel, T. Passow, K. Leonardi, and D. Hommel, Phys. Rev. B **64**, 121303 (2001).

[201] C. Wang, B. L. Wehrenberg, C. Y. Woo, and P. Guyot-Sionnest, J. Phys. Chem. B **108**, 9027 (2004).

[202] A. I. Ekimov, F. Hache, M. C. Schanne-Klein, D. Ricard, C. Flytzanis, I. A. Kudryavtsev, T. V. Yazeva, A. V. Rodina, and Al. L. Efros, J. Opt. Soc. Am. B **10**, 100 (1993).

[203] D. J. Norris, A. Sacra, C. B. Murray, and M. G. Bawendi, Phys. Rev. Lett. **72**, 2612 (1994).

[204] R. R. Reeber, J. Mater. Sci. **11**, 590 (1976).

[205] R. G. Wheeler and J. O. Dimmock, Phys. Rev. **125**, 1805 (1962).

[206] R. Geick and C. H. Perry, J. Appl. Phys. **37**, 1994 (1966).

[207] Al. L. Efros, M. Rosen, M. Kuno, M. Nirmal, D. J. Norris, and M. Bawendi, Phys. Rev. B **54**, 4843 (1996).

[208] M. Achermann, J. A. Hollingsworth, and V. I. Klimov, Phys. Rev. B **68**, 245302 (2003).

[209] M. Ouyang, private communication.

[210] J. Schrier and K. B. Whaley, cond-mat/0502080.

[211] A. Blais, R.-S. Huang, A. Wallraff, S. M. Girvin, and R. J. Schoelkopf, Phys. Rev. A **69**, 062320 (2004).

[212] A. Wallraff, D. I. Schuster, A. Blais, L. Frunzio, R.-S. Huang, J. Majer, S. Kumar, S. M. Girvin, and R. J. Schoelkopf, Nature (London) **431**, 162 (2004).

[213] O. Gywat, V. Cerletti, F. Meier, D. Loss, and D. D. Awschalom, (unpublished).

[214] *Confined Photon Systems*, H. Benisty, J.-M. Gérard, R. Houdré, J. Rarity, and C. Weisbuch (eds.), Springer (1999).

[215] J. P. Reithmaier, G. Sek, A. Löffler, C. Hofmann, S. Kuhn, S. Reitzenstein, L. V. Keldysh, V. D. Kulakovskii, T. L. Reinecke, and A. Forchel, Nature (London) **432**, 197 (2004).

[216] T. Yoshie, A. Scherer, J. Hendrickson, G. Khitrova, H. M. Gibbs, G. Rupper, C. Ell, O. B. Shchekin, and D. G. Deppe, Nature (London) **432**, 200 (2004).

[217] Q. A. Turchette, C. J. Hood, W. Lange, H. Mabuchi, and H. J. Kimble, Phys. Rev. Lett. **75**, 4710 (1995).

[218] B. T. H. Varcoe, S. Brattke, M. Weidinger, and H. Walther, Nature (London) **403**, 743 (2000).

[219] S. J. van Enk, J. I. Cirac, and P. Zoller, Phys. Rev. Lett. **78**, 4293 (1997).

[220] A. Imamoḡlu, Fortschr. Phys. **48**, 987 (2000).

[221] A. Kiraz, C. Reese, B. Gayral, L. Zhang, W. V. Schoenfeld, B. D. Gerardot, P. M. Petroff, E. L. Hu, and A. Imamoḡlu, J. Opt. B **5**, 129 (2003).

[222] J. Vučković and Y. Yamamoto, Appl. Phys. Lett. **82**, 2374 (2003).

[223] A. P. Prudnikow, Y. A. Brychkov, and O. I. Marichev, *Integrals and Series*, Gordon and Breach, New York (1986).

[224] M. Abramowitz and I. A. Stegun, *Handbook of Mathematical Functions with Formulas, Graphs, and Mathematical Tables*, Dover Publications, Inc., New York (1972).

Curriculum Vitae

von Oliver Gywat
Geboren: 9. Dezember 1976 in Basel
Staatsangehörigkeit: Schweizer

Ausbildung

1984–1988	Primarschule in Riehen
1988–1995	Besuch des Gymnasiums am Freien Gymnasium Basel
Juni 1995	Matura (Typus B) mit Auszeichnung
1995–1996	Militärdienst in der Schweizer Armee
1996–2001	Studium der Physik, Mathematik und Astronomie an der Universität Basel
März 2001	Diplom in Theoretischer Physik Diplomarbeit "Biexcitons in Semiconductor Quantum Dots" in theoretischer Festkörperphysik unter der Anleitung von Prof. D. Loss.
2001–2005	Promotionsstudium in Theoretischer Physik an der Universität Basel Dissertation "Electron–photon interaction in quantum dots: spin and entanglement" unter der Anleitung von Prof. D. Loss
April 2005	Promotion mit Prädikat "summa cum laude"

Meine universitäre Ausbildung verdanke ich den Professoren
C. Bandle, G. Bauer, B. Binggeli, C. Bruder, R. Buser, O. Gerhard, B. Hecht, A. V. Khaetskii, H. P. Kraft, D. Loss, D. Masser, E. Meyer, D. Pohl, C. Schönenberger, I. Sick, G.-A. Tamman, L. Tauscher, F.-K. Thielemann, H. Thomas und D. Trautmann, sowie den Privatdozenten
U. Aeschbacher, T. Ahrend, W. Belzig, W. Breymann, A. Bussmann-Holder, F.-J. Elmer, H. Mühry, J. Schliemann und P. Talkner.

Publikationen

Veronica Cerletti, W. A. Coish, Oliver Gywat, and Daniel Loss,
Recipes for spin-based quantum computing,
Nanotechnology **16**, R27 (2005); see also cond-mat/0412028.

Veronica Cerletti, Oliver Gywat, and Daniel Loss,
Entanglement transfer from electron spins to photons,
cond-mat/0411235.

Oliver Gywat, Hans-Andreas Engel, and Daniel Loss,
Probing Single-Electron Spin Decoherence in Quantum Dots using Charged Excitons,
cond-mat/0408451, to appear in J. Supercond. (2005).

Florian Meier, Veronica Cerletti, Oliver Gywat, Daniel Loss, and D. D. Awschalom,
Molecular spintronics: Coherent spin transfer in coupled quantum dots,
Phys. Rev. B **69**, 195315 (2004); see also cond-mat/0401397.

Oliver Gywat, Hans-Andreas Engel, Daniel Loss, R. J. Epstein, F. Mendoza, and D. D. Awschalom,
Optical Detection of Single-Electron Spin Decoherence in a Quantum Dot,
Phys. Rev. B **69**, 205303 (2004); see also cond-mat/0307669.

Oliver Gywat, Guido Burkard, and Daniel Loss,
Quantum computation and the production of entangled photons using coupled quantum dots, Superlattices and Microstructures **31**, 127 (2002).

Oliver Gywat, Guido Burkard, and Daniel Loss,
Biexcitons in coupled quantum dots as a source of entangled photons,
Phys. Rev. B **65**, 205329 (2002); see also cond-mat/0109223.

Die angegebenen Preprint-Versionen können via die URL http://arXiv.org/abs/cond-mat/ heruntergeladen werden.